

**UNICAMP**

Universidade Estadual de Campinas

Faculdade de Engenharia Civil, Arquitetura e Urbanismo

Gustavo Alcalá Batistela

**A posteriori error estimation for the  
multiscale hybrid-mixed finite element  
method**

**Estimação de erro a posteriori para o método  
dos elementos finitos híbrido-misto  
multiescala**

Campinas

2023

Gustavo Alcalá Batistela

**A posteriori error estimation for the multiscale  
hybrid-mixed finite element method**

**Estimação de erro a posteriori para o método dos  
elementos finitos híbrido-misto multiescala**

Dissertation presented to the School of Civil Engineering, Architecture and Urban Design of the University of Campinas in partial fulfillment of the requirements for the degree of Master in Civil Engineering.

Dissertação apresentada à Faculdade de Engenharia Civil, Arquitetura e Urbanismo da Universidade Estadual de Campinas como parte dos requisitos exigidos para a obtenção do título de Mestre em Engenharia Civil.

Supervisor: Philippe Remy Bernard Devloo

Este exemplar corresponde à versão final da Dissertação defendida pelo aluno Gustavo Alcalá Batistela e orientada pelo Prof. Dr. Philippe Remy Bernard Devloo.

Campinas

2023

Ficha catalográfica  
Universidade Estadual de Campinas  
Biblioteca da Área de Engenharia e Arquitetura  
Elizangela Aparecida dos Santos Souza - CRB 8/8098

B320p Batistela, Gustavo Alcalá, 1995-  
A posteriori error estimation for the multiscale hybrid-mixed finite element method / Gustavo Alcalá Batistela. – Campinas, SP : [s.n.], 2023.

Orientador: Philippe Remy Bernard Devloo.  
Dissertação (mestrado) – Universidade Estadual de Campinas, Faculdade de Engenharia Civil, Arquitetura e Urbanismo.

1. Erro - Estimativas. 2. Método dos elementos finitos.. 3. Multiescala. I. Devloo, Philippe Remy Bernard, 1958-. II. Universidade Estadual de Campinas. Faculdade de Engenharia Civil, Arquitetura e Urbanismo. III. Título.

Informações Complementares

**Título em outro idioma:** Estimção de erro a posteriori para o método dos elementos finitos híbrido-misto multiescala

**Palavras-chave em inglês:**

Error - Estimates

Finite element method

Multiscale

**Área de concentração:** Estruturas e Geotécnica

**Titulação:** Mestre em Engenharia Civil

**Banca examinadora:**

Philippe Remy Bernard Devloo [Orientador]

Gustavo Henrique Siqueira

Paulo Rafael Bösing

**Data de defesa:** 10-03-2023

**Programa de Pós-Graduação:** Engenharia Civil

**Identificação e informações acadêmicas do(a) aluno(a)**

- ORCID do autor: <https://orcid.org/0000-0003-2991-3682>

- Currículo Lattes do autor: <http://lattes.cnpq.br/0538278432452249>

**UNIVERSIDADE ESTADUAL DE CAMPINAS  
FACULDADE DE ENGENHARIA CIVIL, ARQUITETURA E  
URBANISMO**

**A posteriori error estimation for the multiscale hybrid-  
mixed finite element method (Estimação de erro a  
posteriori para o método dos elementos finitos híbrido-  
misto multiescala)**

**Gustavo Alcalá Batistela**

**Dissertação de Mestrado aprovada pela Banca Examinadora, constituída por:**

**Prof. Dr. Philippe Remy Bernard Devloo  
Presidente e Orientador(a)/FECFAU-Unicamp**

**Prof. Dr. Gustavo Henrique Siqueira  
FECFAU-Unicamp**

**Prof. Dr. Paulo Rafael Bösing  
Universidade Federal da Fronteira Sul**

A Ata da defesa com as respectivas assinaturas dos membros encontra-se no SIGA/Sistema de Fluxo de Dissertação/Tese e na Secretaria do Programa da Unidade.

Campinas, 10 de Março de 2023

# Acknowledgements

I would like to express my heartfelt appreciation to those who have supported me during the writing of my dissertation.

Firstly, I am grateful for the invaluable guidance and expertise provided by my supervisor, Philippe Devloo. His unlimited creativity is truly inspirational. Secondly, I would like to extend my gratitude to Denise Siqueira, who I consider co-advisor of this work. Denise has been a constant source of presence and encouragement throughout this journey and helped me in every single step of this research.

I am also grateful for the emotional support provided by my parents, Fabiana and Licio, my partner Luiza, and my grandparents, who have been a constant source of love and motivation during this challenging period.

Additionally, I would like to acknowledge the collaborative support of the entire LabMec team. This includes hours of programming insights and discussions provided by Francisco, and the contribution of Sonia, who helped me grasp mathematical concepts that were instrumental to my research.

Finally, I'd like to acknowledge the financial support received by FAPESP: grant #2020/06301-6, São Paulo Research Foundation (FAPESP).

# Resumo

Estimação de erro a posteriori para o método dos elementos finitos misto-híbrido multiescala para problemas de Darcy,  $\text{MHM-H}(\text{div})-\mathcal{E}_\gamma$ , é apresentada. O método  $\text{MHM-H}(\text{div})-\mathcal{E}_\gamma$  adota espaços de elementos finitos de duas escalas: discretizações refinadas são adotadas no interior de subregiões poligonais, mas aproximações do fluxo são restritas sobre as interfaces da malha por um espaço de traços normais *coarse*. Para estabilidade, aproximações da pressão e do fluxo são compatíveis em termos do divergente, satisfazendo o diagrama de De Rham. A estimação de erro se baseia na reconstrução do potencial, método popular neste tipo de análise no contexto de métodos mistos. Experimentos numéricos são apresentados para ilustrar a eficiência da metodologia proposta.

**Palavras-chave:** Estimação de erro; métodos híbridos multiescala; fluxo com restrição de traço

# Abstract

A posteriori error estimation for the multiscale hybrid-mixed finite element method for Darcy's problems,  $\text{MHM-H}(\text{div})-\mathcal{E}_\gamma$ , is presented. The  $\text{MHM-H}(\text{div})-\mathcal{E}_\gamma$  adopts two-scale finite element spaces: refined discretizations are adopted inside polygonal subregions, and flux approximations are constrained over the mesh interfaces by a given coarse normal trace space. For stability, pressure and flux approximations are divergence compatible, satisfying De Rham's diagram. The error estimation is based on potential reconstruction, which is a popular technique for this kind of analysis in the context of mixed methods. Numerical experiments are presented in order to illustrate the efficiency of the proposed methodology.

**Keywords:** Error estimation; multiscale hybrid methods; flux with trace constraints

# List of Figures

Figure 1 – Plot of function $f(t) = \tan(t)$ . . . . .	16
Figure 2 – Representation of the trace of a function $u \in H^1(\Omega)$ defined over a quadrilateral domain over $\Gamma$ , where $\Gamma = \partial\Omega$ . . . . .	17
Figure 3 – Representation of the normal trace of a function $\mathbf{v} \in H(\text{div}, \Omega)$ defined over a quadrilateral domain over $\Gamma_1 \dots \Gamma_4 = \partial\Omega$ , such that $\mathbf{v} \cdot \mathbf{n} _{\Gamma_1} = g$ , where $g$ is a linear function, and $\mathbf{v} \cdot \mathbf{n} _{\partial\Omega \setminus \Gamma_1} = 0$ . . . . .	19
Figure 4 – Elements of the finite element mesh . . . . .	20
Figure 5 – Transformations between parametric and geometric spaces . . . . .	21
Figure 6 – Decomposition of a quadrilateral element into its sides . . . . .	21
Figure 7 – Partition $\mathcal{T}_h = \{K_1, K_2\}$ . . . . .	23
Figure 8 – Example of an $L^2(\Omega)$ vertex function . . . . .	23
Figure 9 – Example of an $L^2(\Omega)$ edge function . . . . .	23
Figure 10 – Example of an $L^2(\Omega)$ face function . . . . .	24
Figure 11 – $\phi \in H^1(\Omega)$ such that $\mathcal{F}_{K_1}^{-1}(\phi _{K_1}) = \hat{\phi}^{v_2}(\xi, \eta)$ and $\mathcal{F}_{K_2}^{-1}(\phi _{K_2}) = \hat{\phi}^{v_3}(\xi, \eta)$ . . . . .	24
Figure 12 – $\phi \in H^1(\Omega)$ such that $\mathcal{F}_{K_1}^{-1}(\phi _{K_1}) = \hat{\phi}^{e_1,0}(\xi, \eta)$ and $\mathcal{F}_{K_2}^{-1}(\phi _{K_2}) = \hat{\phi}^{e_3,0}(\xi, \eta)$ . . . . .	25
Figure 13 – $\phi \in H^1(\Omega)$ such that $\mathcal{F}_{K_1}^{-1}(\phi _{K_1}) = \hat{\phi}^{f,0,0}(\xi, \eta)$ . . . . .	25
Figure 14 – Constant vector fields defined on the quadrilateral element . . . . .	26
Figure 15 – Examples of $H(\text{div}, \Omega)$ functions on the reference element . . . . .	26
Figure 16 – Example of an edge quadrilateral $H(\text{div}, \Omega)$ function $\phi \in H(\text{div}, \Omega)$ such that $\mathcal{F}_{\text{div},K_1}^{-1}(\phi _{K_1}) = \hat{\phi}^{v_2}(\xi, \eta) \cdot \hat{\mathbf{v}}_4$ and $\mathcal{F}_{\text{div},K_2}^{-1}(\phi _{K_2}) = -\hat{\phi}^{v_3}(\xi, \eta) \cdot \hat{\mathbf{v}}_9$ . . . . .	27
Figure 17 – Example of an edge quadrilateral $H(\text{div}, \Omega)$ function $\phi \in H(\text{div}, \Omega)$ such that $\mathcal{F}_{\text{div},K_1}^{-1}(\phi _{K_1}) = \hat{\phi}^{f,0,0}(\xi, \eta) \cdot \hat{\mathbf{v}}_{17}$ . . . . .	27
Figure 18 – Problem domain with boundary parts $\Gamma_D$ , $\Gamma_N$ and outward unit normal field $\mathbf{n}$ . . . . .	29
Figure 19 – Example of a hierarchy of partitions $\mathcal{T}$ , $\mathcal{T}^\Gamma$ , and $\mathcal{T}_{\text{hin}}^{\Omega_i}$ for the MHM-H(div)- $\mathcal{E}_\gamma$ method. . . . .	37
Figure 20 – Interpretation of the upscaling operation as DoF constraints coupling local mixed problems on each macro domain. . . . .	39
Figure 21 – Illustration of the inter-element smoothing procedure: average over edges. . . . .	50
Figure 22 – Illustration of the inter-element smoothing procedure: update vertex values. . . . .	51
Figure 23 – Illustration of the potential reconstruction: (a) exact potential $u$ , (b) MHM-H(div)- $\mathcal{E}_\gamma$ solution $\tilde{u}$ , and (c) potential reconstruction $s \in H^1(\Omega)$ . . . . .	52
Figure 24 – Exact solution $u(x, y)$ of the smooth problem. . . . .	56

Figure 25 – Smooth solution problem: (a) square subregions and L-shaped subregions (b). . . . .	56
Figure 26 – Smooth solution approximated by the MHM-H(div)- $\mathcal{E}_\gamma$ method with square subregion geometry: exact errors $E_{\text{ex}}(\Omega_i)$ , estimated errors $\eta_{P,\Omega_i}$ , and local effectivity indexes $I_{\text{eff}}(\Omega_i)$ in the subregions, for space configuration with $h_{sk} = 1/4$ , $h_{in} = 1/8$ , $k_{sk} = 1$ and $k_{in} = 3$ . . . . .	57
Figure 27 – Smooth solution approximated by the MHM-H(div)- $\mathcal{E}_\gamma$ method with L-shaped subregion geometry: exact errors $E_{\text{ex}}(\Omega_i)$ , estimated errors $\eta_{P,\Omega_i}$ , and local effectivity indexes $I_{\text{eff}}(\Omega_i)$ in the subregions, for space configuration with $h_{sk} = 1/4$ , $h_{in} = 1/8$ , $k_{sk} = 1$ and $k_{in} = 3$ . . . . .	57
Figure 28 – Smooth solution approximated by the MHM-H(div)- $\mathcal{E}_\gamma$ method on square partitions using discretization parameters $h_{sk} = 2^{-j}$ , $j = 2, \dots, 6$ , $h_{in} = h_{sk}/2^l$ , $l = 0, 1$ and $2$ , $k_{sk} = i$ , $k_{in} = k_{sk} + i$ , with $i = 1$ and $2$ . Left plots: exact errors $E_{\text{ex}}$ (dashed lines) and estimated errors $E_{\text{est}}$ (continuous lines). Right plots: corresponding global effectivity indexes $I_{\text{eff}}$ . . . . .	60
Figure 29 – Singular solution: (a) local exact error and (b) estimated error for L-shape mesh using space configurations of type $k_{sk} = 1$ and $k_{in} = k_{sk} + 3$ , $h_{in} = h_{sk} = 2^{-3}$ . . . . .	61
Figure 30 – Historic of convergence for the singular problem. Left side: curves of estimated error and exact error; right side: curve of the effectivity index. . . . .	61
Figure 31 – Problem with inner singularity: permeability distribution and exact solution. . . . .	62
Figure 32 – Solution with inner singularity approximated by the MHM-H(div)- $\mathcal{E}_\gamma$ method based on square partitions using discretization parameters $h_{sk} = 2^{-j}$ , $j = 2, \dots, 6$ , $h_{in} = h_{sk}/2^l$ , $l = 0, 1$ and $2$ , $k_{sk} = 1$ , $k_{in} = 2$ , and $3$ . Left plots: exact errors (dashed lines) and the estimated errors (continuous lines). Right plots: corresponding global effectivity indexes. . . . .	64
Figure 33 – Solution with high corner gradient approximated by the MHM-H(div)- $\mathcal{E}_\gamma$ method based two-level finite element setting for uniform coarse square partition, for $h_{sk} = 1/5$ , $h_{in} = h_{sk}/2$ , $k_{ks} = 1$ , and $k_{in} = 3$ : the exact solution $u(x, y)$ , local exact errors, local estimated errors, and local effectivity indexes in each macro domain $\Omega_i \in \mathcal{T}$ . . . . .	65
Figure 34 – Solution with high corner gradient approximated by the MHM-H(div)- $\mathcal{E}_\gamma$ method for $\mathcal{E}_\gamma$ based on a sequence of six $h$ -adaptive partitions: by refinement of the skeleton partition of Algorithm 1 (top meshes), and refinement of the subregions of Algorithm 2 (bottom meshes). . . . .	66

Figure 35 – Solution with high corner gradient approximated by the MHM-H(div)- $\mathcal{E}_\gamma$ method based on uniform partitions (red lines), on $h$ -adaptive trace partitions by Algorithm 1 (A1 - black lines), on $h$ -adaptive partitions by Algorithm 2 (A2 - blue lines), using $k_{ks} = 1$ and $k_{in} = 3$ . Left plots: exact errors $E_{\text{ex}}$ (continuous lines) and estimator errors $E_{\text{est}}$ (dashed lines) versus DoF. Right plots: effectivity indexes $I_{\text{eff}}$ for uniform and adaptive settings. . . . .	67
Figure 36 – Heterogenous permeability (in log distribution). . . . .	67
Figure 37 – Darcy’s model with heterogeneous permeability: approximation potential $\tilde{u}$ and flux $\tilde{\sigma}$ by the MHM-H(div)- $\mathcal{E}_\gamma$ based on the coarse sub-region partition $\mathcal{T}^0$ , the trace adapted partition $\mathcal{T}^{\Gamma,8}$ , internal sub-partitions $\mathcal{T}_{h_{in}}^{\Omega_i}$ , with $h_{in} = 1$ , polynomial degrees $k_{sk} = 1$ , and $k_{in} = 4$ . . . . .	68
Figure 38 – Darcy’s model with heterogeneous permeability: $h$ -adapted skeleton partitions $\mathcal{T}^{\Gamma,\ell}$ , $\ell = 1, 3, 6$ and $8$ , and local estimated errors $\eta_{P,\Omega_i}$ of adaptive solutions obtained by Algorithm 1 for the MHM-H(div)- $\mathcal{E}_\gamma$ formulation using the fixed coarse sub-region partition $\mathcal{T}^0$ and internal sub-partitions $\mathcal{T}_{h_{in}}^{\Omega_i}$ , with $h_{in} = 1$ , polynomial degrees $k_{sk} = 1$ , and $k_{in} = 4$ . . . . .	69
Figure 39 – Darcy’s model with heterogeneous permeability: estimated errors of adaptive solutions of the MHM-H(div)- $\mathcal{E}_\gamma$ formulation obtained by Algorithm 1 using space configurations based on the fixed coarse sub-region $\mathcal{T}^0$ , internal sub-partitions $\mathcal{T}_{h_{in}}^{\Omega_i}$ , with $h_{in} = 1$ , trace adapted partitions $\mathcal{T}^{\Gamma,\ell}$ , $\ell = 1, \dots, 8$ , polynomial degrees $k_{sk} = 1$ , and $k_{in} = 4$ . . . . .	70

# Contents

<b>1</b>	<b>INTRODUCTION</b> . . . . .	<b>13</b>
<b>1.1</b>	<b>Objectives</b> . . . . .	<b>14</b>
<b>1.2</b>	<b>Organization of the content</b> . . . . .	<b>14</b>
<b>2</b>	<b>INFINITE AND FINITE ELEMENT SPACES</b> . . . . .	<b>15</b>
<b>2.1</b>	<b>Functional spaces</b> . . . . .	<b>16</b>
2.1.1	The $L^2(\Omega)$ space . . . . .	16
2.1.2	The $H^1(\Omega)$ space, its trace and relevant subspaces . . . . .	17
2.1.3	The $H(\text{div}, \Omega)$ space, its trace and relevant subspaces . . . . .	18
<b>2.2</b>	<b>Finite-dimensional spaces</b> . . . . .	<b>19</b>
2.2.1	Finite element mesh . . . . .	19
2.2.2	Shape functions . . . . .	20
2.2.3	Finite element spaces . . . . .	27
<b>3</b>	<b>CLASSICAL FINITE ELEMENT FORMULATIONS</b> . . . . .	<b>29</b>
<b>3.1</b>	<b>The model problem</b> . . . . .	<b>29</b>
<b>3.2</b>	<b>Primal <math>H^1(\Omega)</math> formulation</b> . . . . .	<b>30</b>
<b>3.3</b>	<b><math>H(\text{div}, \Omega)</math>-conforming mixed formulation</b> . . . . .	<b>31</b>
3.3.1	Finite-dimensional space pairs for mixed approximations . . . . .	31
3.3.2	Finite element formulation . . . . .	32
<b>4</b>	<b>THE MHM-<math>H(\text{div})</math>-<math>\mathcal{E}_\gamma</math> METHOD</b> . . . . .	<b>35</b>
<b>4.1</b>	<b>Concepts regarding geometry</b> . . . . .	<b>35</b>
<b>4.2</b>	<b>Finite element space settings</b> . . . . .	<b>35</b>
<b>4.3</b>	<b>Global-local algorithms</b> . . . . .	<b>38</b>
<b>4.4</b>	<b>Important properties</b> . . . . .	<b>39</b>
<b>4.5</b>	<b>Examples of hierarchic MHM settings</b> . . . . .	<b>41</b>
<b>5</b>	<b>ERROR ESTIMATION</b> . . . . .	<b>42</b>
<b>5.1</b>	<b>Estimates for the flux</b> . . . . .	<b>43</b>
<b>5.2</b>	<b>Potential reconstruction</b> . . . . .	<b>48</b>
5.2.1	Inter-element smoothing procedure . . . . .	49
5.2.2	Solving local Dirichlet problems . . . . .	51
<b>5.3</b>	<b>Adaptivity</b> . . . . .	<b>52</b>
5.3.1	Stable $h$ -adaptive finite element settings $\mathcal{E}_\gamma$ . . . . .	52
5.3.2	Trace $h$ -adaptivity . . . . .	52

5.3.3	Classic h-adaptivity . . . . .	54
<b>6</b>	<b>NUMERICAL RESULTS . . . . .</b>	<b>55</b>
<b>6.1</b>	<b>Tests with two-level finite element space settings <math>\mathcal{E}_\gamma</math> . . . . .</b>	<b>55</b>
6.1.1	Problem with smooth solution . . . . .	55
6.1.1.1	Effect of the shape of the macro domain . . . . .	56
6.1.1.2	Effect of internal refinement . . . . .	58
<b>6.2</b>	<b>Singular solution on L- shape domain . . . . .</b>	<b>61</b>
<b>6.3</b>	<b>Solution with inner point singularity . . . . .</b>	<b>62</b>
6.3.1	Solution with a corner strong gradient . . . . .	65
6.3.1.1	A two-level numerical test . . . . .	65
6.3.1.2	Comparison of adaptive strategies . . . . .	65
6.3.2	Flow in heterogeneous porous media: trace adaptivity . . . . .	67
<b>7</b>	<b>CONCLUSION . . . . .</b>	<b>71</b>
	<b>BIBLIOGRAPHY . . . . .</b>	<b>72</b>
	<b>APPENDIX A – PROOF OF THEOREMS . . . . .</b>	<b>75</b>
<b>A.1</b>	<b>Proof of Theorem 1 . . . . .</b>	<b>75</b>
<b>A.2</b>	<b>Proof of Theorem 2 . . . . .</b>	<b>77</b>

# 1 Introduction

Many engineering applications involve materials with heterogeneous properties (e.g. composite materials and porous media) which introduce fine-scale characteristics to the problem. In petroleum engineering, these characteristics arise from the spatial distribution of petrophysics parameters like porosity and permeability. To assess uncertainty and evaluate exploitation strategies, an accurate flow representation is required. In numerical simulations of Darcy's flow, governed by Poisson's equation, the fine-scale effects have a great influence on the solution [AARNES, 2004].

Despite a continuing growth in the available computational power, solving these problems in the fine-scale is still not feasible for most cases due to the size of the global system of equations. In this context, multiscale methods, which calculate the solution on different scales separately, emerge as a way to incorporate the fine-scale effects on the solution at a reduced computational cost.

In this work, the MHM- $H(\text{div})-\mathcal{E}_\gamma$  [DURÁN et al., 2019] is considered. The MHM- $H(\text{div})-\mathcal{E}_\gamma$  is a variant of the multiscale hybrid mixed method, MHM [ARAYA et al., 2013], in which local problems are solved by the mixed finite element method. This variant improves the accuracy of the flux solution while ensuring local mass conservation at both scales. The global, coarse, problem consists in finding a constant piecewise pressure in the interior of the coarse elements, which we denote subdomain, and coarse normal flux on the interface between adjacent subdomains. The coarse normal flux is used as a Neumann boundary condition to local problems in each subdomain, where the fine-scale details, consisting of internal fluxes and a zero-mean pressure field, are solved.

Like every numerical method, for most cases, the obtained solution is an *approximation* of the unknown exact solution. Consequently, there are deviations between the finite element method solution and the exact one. In the case of the MHM- $H(\text{div})-\mathcal{E}_\gamma$ , one of the most prominent source of errors is the restriction of the fine scale flux to the coarser flux on the interfaces between macro elements, according to *a priori* estimates presented in [DURÁN et al., 2019].

*A priori* error estimates is a proof of the asymptotic convergence for a method. However, these estimates can not provide an upper bound for the errors, as they rely on coefficients that depend on the unknown exact solution. In this context, *a posteriori* estimates arise as a framework to provide computable error bounds, based on the approximated solution and the problem settings only.

Additionally, *a posteriori* estimates can be applied to identify the regions of the domain in which the approximation error is greater. This property allows for the use

in adaptive mesh refinement procedures [BABUŠKA; RHEINBOLDT, 1978].

## 1.1 Objectives

The purpose of the current work is to adapt known *a posteriori* error estimations for standard single-scale mixed methods presented in [AINSWORTH, 2010] to the multiscale MHM- $H(\text{div})$ - $\mathcal{E}_\gamma$  context.

The adopted methodology is based on a reconstruction procedure. Given flux and pressure approximate solutions, denoted by  $\sigma_h$  and  $u_h$  respectively, the principle is to recover a second continuous approximation  $s \in H^1(\Omega)$  for pressure (known as reconstructed potential) to be used to estimate the unknown exact flux and pressure errors (see [VOHRALÍK, 2015] for a review on this matter).

The algorithm follows two steps: (a) inter-element smoothing, where a continuous average of the approximate pressure is defined over the mesh skeleton, and (b) the solution of local Dirichlet problems using the interelement average pressure as Dirichlet boundary data.

The algorithm is implemented in the *NeoPZ*<sup>1</sup> [DEVLOO, 1997] environment, an open-source, cross-platform, finite element library written in C++.

## 1.2 Organization of the content

Chapter 2 is dedicated to the description of finite element spaces. In Chapter 3, classical finite element formulations are presented. Chapter 4 describes the fundamental aspects of the MHM- $H(\text{div})$ - $\mathcal{E}_\gamma$ . *A posteriori* error estimates for the MHM- $H(\text{div})$ - $\mathcal{E}_\gamma$  are developed in Chapter 5. Numerical results are shown in Chapter 6.

---

<sup>1</sup> Available at: <<http://www.labmec.org.br/wiki/neopz/start>>

## 2 Infinite and finite element spaces

Many engineering problems can be modelled by a set of partial differential equations, whose exact solution can not be obtained due to the nature of the governing differential equations or to the complexity of the domain.

The finite element method, FEM, is a numerical method to find an approximate solution of a boundary-value problem modelled by a set of partial differential equations. A complete introduction to FEM is found in [BECKER; CAREY; ODEN, 1981] and [CIARLET, 2002].

Its popularity is mainly due to its versatility and generality, being suitable for a wide range of problems, such as wave propagation, elasticity, flow in porous media, etc. Furthermore, its performance stands out when working with complex domains.

The first step towards approximating the solution of a set of PDE with FEM is the definition of a weak or variational formulation of the problem. A weak solution to a differential equation satisfies the differential equation in an integral sense and the equation no longer needs to hold absolutely at every point.

For a given differential equation, there are multiple weak formulations, that may introduce different variables, in different spaces. A finite element method is associated with a specific weak formulation, meaning that there are various finite element methods to solve the same physical problem.

At the continuum level, a weak formulation is supposed to have the same solution as the original problem. The importance of turning the problem into a weak statement is that it can be converted to a discrete algebraic problem by the Ritz-Galerkin method, through which an approximate solution can be found. The solution provided by Ritz-Galerkin method is a linear combination of the basis vectors of a finite-dimensional approximation space.

Once the finite element mesh -a domain partition into elements- is defined, the FEM provides a systematic way of generating this approximation space, typically based on piecewise polynomials with local support on these elements.

Provided the approximation space, the next step is the assembly of the stiffness matrix and the load vector, by numerically integrating the terms of the discretized weak formulation, resulting in a linear system in a matrixial form.

The FEM approximation is obtained by solving this linear system. The solution involves inverting the stiffness matrix, which is typically the most demanding step of the calculation in terms of computational resources.

Once the solution is computed, additional variables may be post-processed by applying constitutive laws on the solution, etc.

This section is dedicated to the description of fundamental functional spaces.

## 2.1 Functional spaces

### 2.1.1 The $L^2(\Omega)$ space

Let  $\Omega \subset \mathbb{R}^d$ ,  $d = 2, 3$ , an open, bounded Lipschitz domain with boundary  $\partial\Omega$ . The first space to consider is the  $L^2(\Omega)$  space, composed of functions which are square-integrable in  $\Omega \subset \mathbb{R}^d$ .

**Definition 1** (The  $L^2(\Omega)$  space).

$$L^2(\Omega) := \left\{ u : \Omega \rightarrow \mathbb{R} : \int_{\Omega} |u|^2 \, d\Omega < +\infty \right\}.$$

Figure 1 illustrates this concept. The function  $f(t) = \tan(t)$  only belongs in  $L^2(\Omega)$  if  $\Omega$  is an interval in which  $f$  is square-integrable. Since  $\int_0^x f^2 \, dt = -x + \tan(x)$  is undefined for  $x = \pi/2 + k\pi$ ,  $\forall k \in \mathbb{Z}$ , therefore  $f \notin L^2(\Omega)$ , in  $\Omega = (0, \pi/2 + k\pi)$  but  $f \in L^2(\Omega)$  if  $\Omega = (-1, 1)$ .

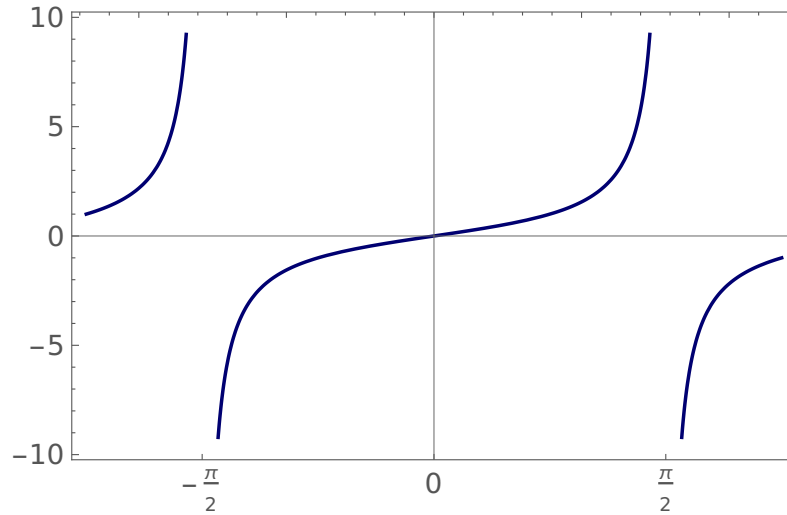


Figure 1 – Plot of function  $f(t) = \tan(t)$

The space  $L^2(\Omega)$  is also a Hilbert space with the inner product:

$$(u, v)_{L^2(\Omega)} := \int_{\Omega} u \cdot v \, d\Omega, \quad (2.1)$$

which induces the  $L^2(\Omega)$  norm:

$$\| \cdot \|_{L^2(\Omega)} := \sqrt{(\cdot, \cdot)_{L^2(\Omega)}}. \quad (2.2)$$

### 2.1.2 The $H^1(\Omega)$ space, its trace and relevant subspaces

The  $H^1(\Omega)$  space is used in the primal finite element method. An  $H^1(\Omega)$ -conforming function is scalar-valued and its gradient is square-integrable.

**Definition 2** (The  $H^1(\Omega)$  space).

$$H^1(\Omega) := \left\{ u \in L^2(\Omega) : \nabla u \in [L^2(\Omega)]^d \right\}.$$

$H^1(\Omega)$  is equipped with the inner product:

$$(u, v)_{H^1(\Omega)} := (u, v)_{L^2(\Omega)} + (\nabla u, \nabla v)_{L^2(\Omega)}, \quad (2.3)$$

which induces the standard  $H^1(\Omega)$  norm:

$$\| \cdot \|_{H^1(\Omega)} := \sqrt{(\cdot, \cdot)_{H^1(\Omega)}}. \quad (2.4)$$

Frequently, there's an interest in the value that functions in  $H^1(\Omega)$  hold on  $d - 1$ -dimensional curves  $\Gamma$ . For a function  $u \in H^1(\Omega)$  we denote  $u|_{\Gamma}$  the restriction of  $u$  on  $\Gamma$ , which is the so-called trace of  $u$  on  $\Gamma$  (Figure 2).

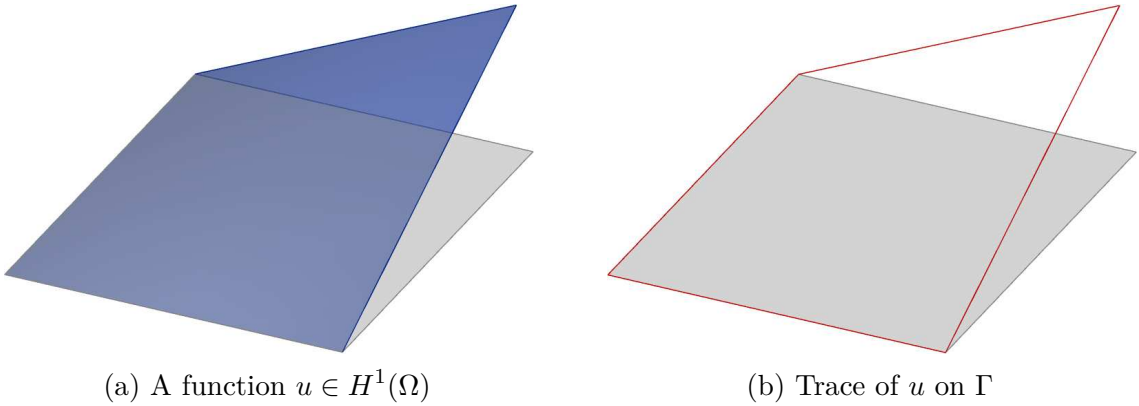


Figure 2 – Representation of the trace of a function  $u \in H^1(\Omega)$  defined over a quadrilateral domain over  $\Gamma$ , where  $\Gamma = \partial\Omega$

This lead to the definition of a normed vector space  $H^{-1/2}(\Gamma)$ , which is the space of traces of  $H^1(\Omega)$ :

**Definition 3** (The  $H^{-1/2}(\Gamma)$  space).

$$H^{-1/2}(\Gamma) := \left\{ u|_{\Gamma} : u \in H^1(\Omega) \right\}.$$

One of the main properties of functions in  $H^1(\Omega)$  is the continuity across  $(d - 1)$  curves  $\Gamma$  (in the sense of  $H^{-1/2}(\Gamma)$ ).

Subspaces of  $H^1(\Omega)$  can be now defined based on specific trace values.

**Definition 4** (The  $H_0^1(\Omega)$  space). *The space  $H_0^1(\Omega)$  is the subspace of  $H^1(\Omega)$  such that  $u|_{\Gamma_D} = 0$  for  $\Gamma_D \subset \partial\Omega$ .*

**Definition 5** (The  $H_{u_D}^1(\Omega)$  space). *The space  $H_{u_D}^1(\Omega)$  is the subspace of  $H^1(\Omega)$  such that  $u|_{\Gamma_D} = u_D$  for  $\Gamma_D \subset \partial\Omega$ .*

### 2.1.3 The $H(\operatorname{div}, \Omega)$ space, its trace and relevant subspaces

In mixed methods, one of the solution variables is the vector-valued flux field, whose divergence must be square-integrable.

**Definition 6** (The  $H(\operatorname{div}, \Omega)$  space).

$$H(\operatorname{div}, \Omega) := \{ \mathbf{v} \in [L^2(\Omega)]^d : \nabla \cdot \mathbf{v} \in L^2(\Omega) \},$$

$H(\operatorname{div}, \Omega)$  is equipped with the inner product:

$$(\mathbf{u}, \mathbf{v})_{H(\operatorname{div}, \Omega)} := (\mathbf{u}, \mathbf{v})_{[L^2(\Omega)]^d} + (\nabla \cdot \mathbf{u}, \nabla \cdot \mathbf{v})_{L^2(\Omega)}, \quad (2.5)$$

which induces the standard  $H(\operatorname{div}, \Omega)$  norm:

$$\| \cdot \|_{H(\operatorname{div}, \Omega)} := \sqrt{(\cdot, \cdot)_{H(\operatorname{div}, \Omega)}}. \quad (2.6)$$

For a function  $\mathbf{v} \in H(\operatorname{div}, \Omega)$  on  $\partial\Omega$ , there's an interest in the normal trace over  $(d-1)$  curves  $\Gamma$ , denoted by  $\mathbf{v} \cdot \mathbf{n}|_{\Gamma}$  (Figure 3).

We denote  $H^{-1/2}(\partial\Omega)$  a normed vector space of the normal traces of  $H(\operatorname{div}, \Omega)$ .

**Definition 7** (The  $H^{-1/2}(\partial\Omega)$  space).

$$H^{-1/2}(\partial\Omega) := \{ \mathbf{v} \cdot \mathbf{n}|_{\partial\Omega} : \mathbf{v} \in H(\operatorname{div}, \Omega) \}.$$

One of the most important characteristics of functions in  $H(\operatorname{div}, \Omega)$  is the continuity of the normal trace.

Once again we define subspaces of  $H(\operatorname{div}, \Omega)$  based on trace values:

**Definition 8** (The  $H_0(\operatorname{div}, \Omega)$  space). *The space  $H_0(\operatorname{div}, \Omega)$  is the subspace of  $H(\operatorname{div}, \Omega)$  such that  $\mathbf{v} \cdot \mathbf{n}|_{\Gamma_N} = 0$  for  $\Gamma_N \subset \partial\Omega$ .*

**Definition 9** (The  $H_{\sigma_N}(\operatorname{div}, \Omega)$  space). *The space  $H_{\sigma_N}(\operatorname{div}, \Omega)$  is the subspace of  $H(\operatorname{div}, \Omega)$  such that  $\mathbf{v} \cdot \mathbf{n}|_{\Gamma_N} = \sigma_N$  for  $\Gamma_N \subset \partial\Omega$ .*

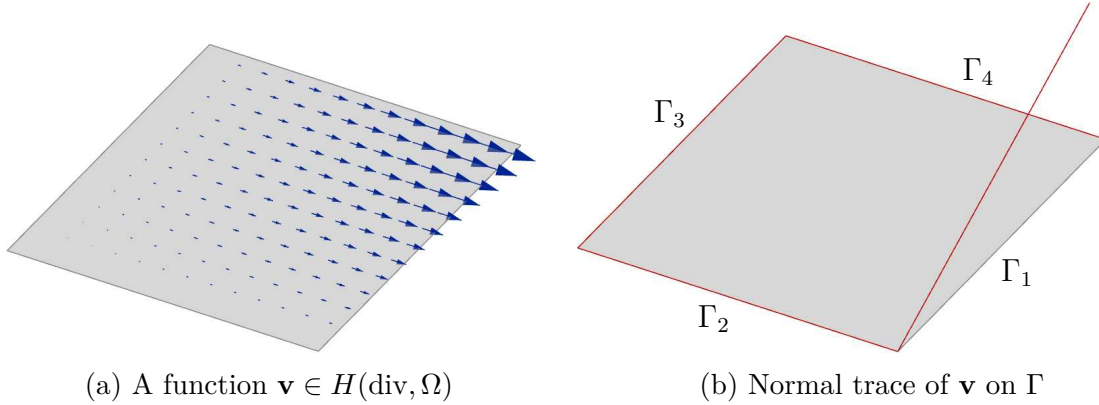


Figure 3 – Representation of the normal trace of a function  $\mathbf{v} \in H(\text{div}, \Omega)$  defined over a quadrilateral domain over  $\Gamma_1 \dots \Gamma_4 = \partial\Omega$ , such that  $\mathbf{v} \cdot \mathbf{n}|_{\Gamma_1} = g$ , where  $g$  is a linear function, and  $\mathbf{v} \cdot \mathbf{n}|_{\partial\Omega \setminus \Gamma_1} = 0$ .

## 2.2 Finite-dimensional spaces

The functional spaces described in the previous section are infinite-dimensional and serve as basis for the understanding and analysis of the mathematical problem we are facing.

Naturally, it is not possible to use an infinite-dimensional space when solving practical problems. To be able to generate algebraic systems and solve a problem computationally, we define finite-dimensional subspaces, called *approximation spaces* or *discrete spaces*, with the same properties of these infinite functional spaces but having finite dimension.

Consider a domain discretization  $\mathcal{T}_h$ , called the finite element mesh. The discrete spaces treated in this work are spanned by basis functions with local support on the elements of  $\mathcal{T}_h$ , and sometimes extending over adjacent elements, denoted by shape functions. The generation of shape functions and the construction of finite-dimensional spaces are detailed in the next sections.

### 2.2.1 Finite element mesh

To apply the finite element method we need to discretize  $\Omega$  into the so-called finite element mesh. The mesh is a partition  $\mathcal{T}_h = \{K\}$  consisting of a finite collection of open subdomains, referred to as elements, such that  $\bar{\Omega} = \cup_{K \in \mathcal{T}_h} \bar{K}$ . The parameter  $h$  is used as an indicator of the size of the elements in the mesh, such that  $h = \max_{K \in \mathcal{T}_h} h_K$ , where  $h_K$  stands for the diameter of the element  $K$ .

For two different elements  $K^+, K^- \in \mathcal{T}_h$ , such that  $K^+ \neq K^-$ ,  $\partial K^+ \cap \partial K^-$  is either an empty set or their common  $d'$ -dimensional sides, with  $0 \leq d' < d$ .

A  $(d - 1)$ -dimensional face  $F \subset \bar{\Omega}$  is called an interface if  $F \subset \partial K^+ \cap \partial K^-$ ,

such that  $K^+ \neq K^-$ , or a boundary face if  $F \subset \partial K \cap \partial\Omega$ . We denote  $\mathcal{E}_h^\circ$  the union of interfaces,  $\mathcal{E}_h^\partial$  the union of boundary faces and  $\mathcal{E}_h = \mathcal{E}_h^\circ \cup \mathcal{E}_h^\partial$ .

An unitary outward normal vector  $\mathbf{n}_F$  is associated to each boundary face  $F \in \mathcal{E}_h^\partial$ . For an interface we have  $\mathbf{n}_F^+$  and  $\mathbf{n}_F^-$  according to the orientation illustrated in Figure 4.

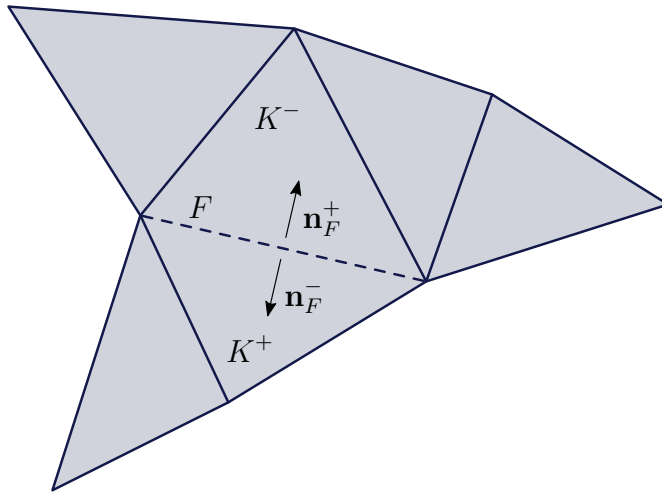


Figure 4 – Elements of the finite element mesh

## 2.2.2 Shape functions

This section presents the methodology of creation of  $L^2(\Omega)$ ,  $H^1(\Omega)$  and  $H(\text{div}, \Omega)$ -conforming shape functions as used in this work.

The shape functions considered in this work are constructed hierarchically, for simplicity of implementing and assembling the constrained finite element spaces required by the MHM-H(div)- $\mathcal{E}_\gamma$  method.

To illustrate the procedure, quadrilateral shape functions are presented.

The basis functions are defined on a parametric space over a reference element  $\hat{K}$  and then mapped to the geometrical space of each element  $K$ . There is a transformation  $\mathcal{F}_K$  mapping a point in parametric coordinates to the geometrical space of the deformed element  $K$  (Figure 5). Remark that the transformation  $\mathcal{F}_K$  may be non-affine.

Shape functions are associated to *sides* of the element. The sides of an element are its vertices, edges, faces and, for three-dimensional elements, its interior volume. For example, a quadrilateral has 9 sides: 4 vertices, 4 edges and 1 face (Figure 6); a hexahedron has 27 sides: 8 vertices, 12 edges, 6 faces and 1 volume, etc.

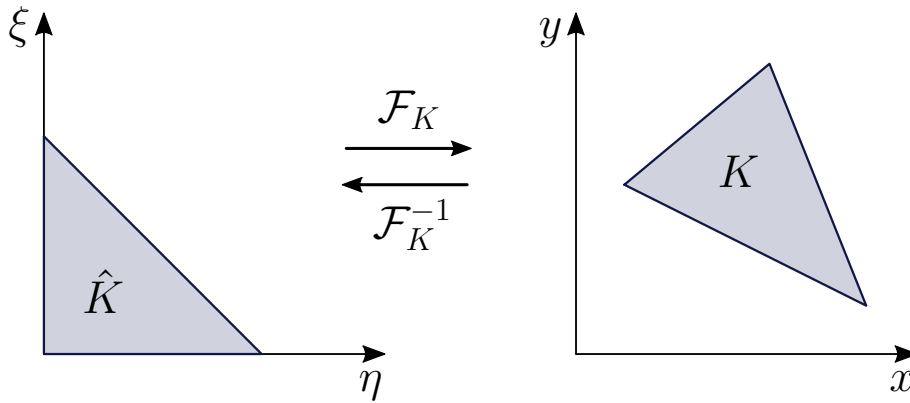


Figure 5 – Transformations between parametric and geometric spaces

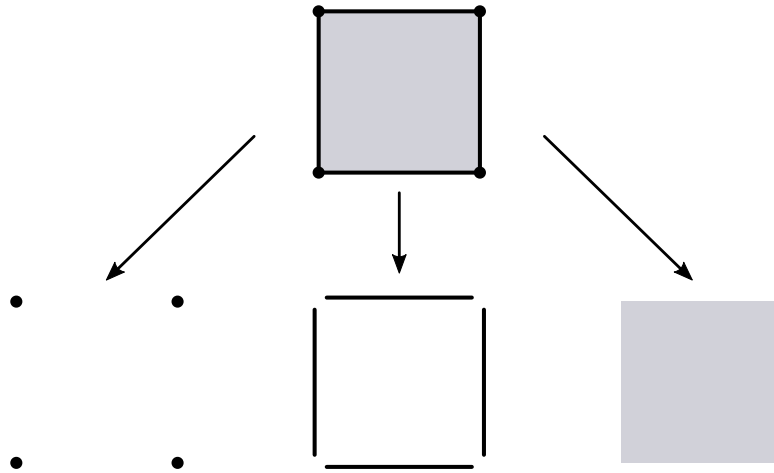


Figure 6 – Decomposition of a quadrilateral element into its sides

$L^2(\Omega)$ -conforming shape functions

For  $L^2(\Omega)$ , we create the shape functions through the definition of polynomial spaces of order  $k$  defined in the reference element  $\hat{K}$ , denoted  $P_k(K)$ , according to the procedure described in [DEVLOO; BRAVO; RYLO, 2009]. The polynomials are then mapped to the deformed element  $K \in \mathcal{T}_h$ . For two-dimensional elements there are shape functions associated with vertices, edges and faces. Three-dimensional elements have additional volume functions.

In order to present shape functions for the quadrilateral element  $\mathcal{Q}$ , the reference element must be defined:

$$\hat{K} = \{(\xi, \eta) \in \mathbb{R}^2 : -1 \leq \xi, \eta \leq 1\} \subset \mathbb{R}^2.$$

The construction of shape functions are based on a sequence of one-dimensional polynomials. Here, Chebyshev polynomials of first kind are considered. The Chebyshev

polynomial of order  $n$ , denoted by  $f_n(t)$ , is defined by the following recursive relation:

$$\begin{cases} f_0(t) = 1 \\ f_1(t) = t \\ f_n(t) = 2tf_{n-1}(t) - f_{n-2}(t), \quad n \geq 2. \end{cases} \quad (2.7)$$

From the developments above, we define the following set of shape functions on the quadrilateral element:

- 4 vertex functions:  $\hat{\phi}^{v_i}(\xi, \eta)$ ,  $i = \{0, 1, 2, 3\}$ :

$$\hat{\phi}^{v_0}(\xi, \eta) = \frac{(1-\xi)}{2} \frac{(1-\eta)}{2}, \quad (2.8)$$

$$\hat{\phi}^{v_1}(\xi, \eta) = \frac{(1+\xi)}{2} \frac{(1-\eta)}{2}, \quad (2.9)$$

$$\hat{\phi}^{v_2}(\xi, \eta) = \frac{(1+\xi)}{2} \frac{(1+\eta)}{2}, \quad (2.10)$$

$$\hat{\phi}^{v_3}(\xi, \eta) = \frac{(1-\xi)}{2} \frac{(1+\eta)}{2}, \quad (2.11)$$

- $4(k-1)$  edge functions  $\hat{\phi}^{e_i, n}(\xi, \eta)$ ,  $i = \{0, 1, 2, 3\}$ ,  $0 \leq n \leq k-2$ :

$$\hat{\phi}^{e_0, n}(\xi, \eta) = \hat{\phi}^{v_0}(\xi, \eta) \left[ \hat{\phi}^{v_1}(\xi, \eta) + \hat{\phi}^{v_2}(\xi, \eta) \right] f_n(\xi), \quad (2.12)$$

$$\hat{\phi}^{e_1, n}(\xi, \eta) = \hat{\phi}^{v_1}(\xi, \eta) \left[ \hat{\phi}^{v_2}(\xi, \eta) + \hat{\phi}^{v_3}(\xi, \eta) \right] f_n(\eta), \quad (2.13)$$

$$\hat{\phi}^{e_2, n}(\xi, \eta) = \hat{\phi}^{v_2}(\xi, \eta) \left[ \hat{\phi}^{v_3}(\xi, \eta) + \hat{\phi}^{v_0}(\xi, \eta) \right] f_n(-\xi), \quad (2.14)$$

$$\hat{\phi}^{e_3, n}(\xi, \eta) = \hat{\phi}^{v_3}(\xi, \eta) \left[ \hat{\phi}^{v_0}(\xi, \eta) + \hat{\phi}^{v_1}(\xi, \eta) \right] f_n(-\eta), \quad (2.15)$$

- $(k-1)^2$  face functions  $\hat{\phi}^{f, n_0, n_1}(\xi, \eta)$ ,  $0 \leq n_0, n_1 \leq k-2$ :

$$\hat{\phi}^{f, n_0, n_1}(\xi, \eta) = \hat{\phi}^{v_0}(\xi, \eta) \hat{\phi}^{v_2}(\xi, \eta) f_{n_0}(\xi) f_{n_1}(\eta), \quad (2.16)$$

To illustrate the creation of shape functions in this section, we consider the partition  $\mathcal{T}_h = \{K_1, K_2\}$ , depicted in Figure 7. In this example,  $K_1$  is defined by the vertices  $P_1 = \{(4.0, 2.0), (8.5, 3.5), (3.5, 8.5), (2.0, 4.0)\}$  and  $K_2$  is defined by  $P_2 = \{(8.5, 3.5), (10.0, 8.0), (8.0, 10.0), (3.5, 8.5)\}$ .

Examples of  $L^2(\Omega)$  vertex, edge and face functions are shown in Figures 8, 9 and 10 respectively.

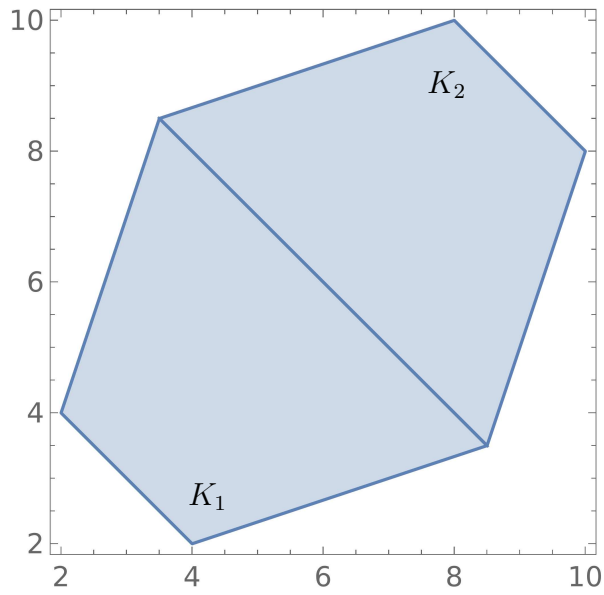
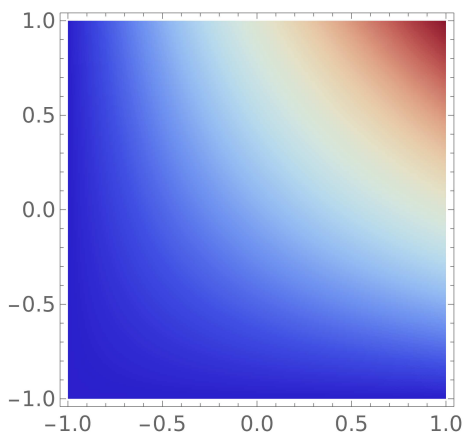
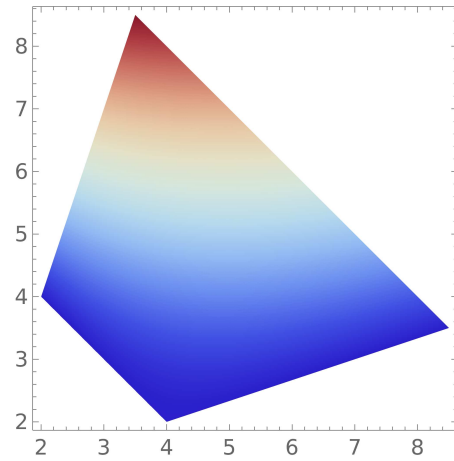


Figure 7 – Partition  $\mathcal{T}_h = \{K_1, K_2\}$

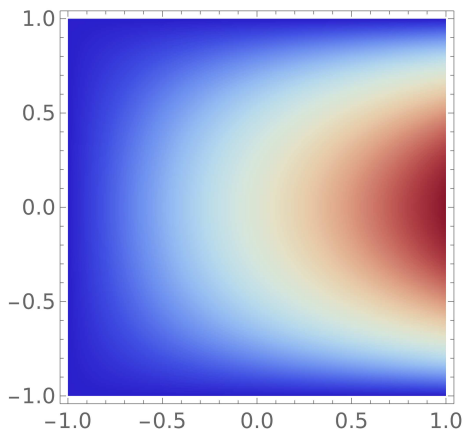


(a)  $\hat{\phi}^{v_2}(\xi, \eta)$

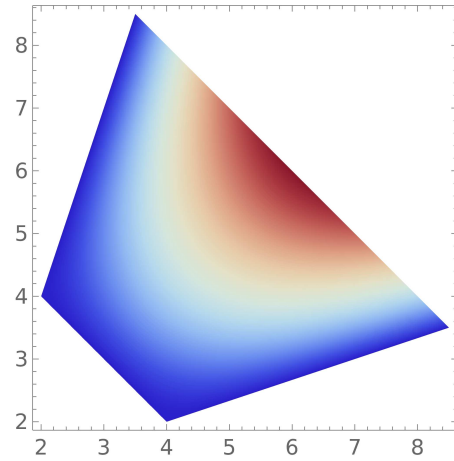


(b)  $\phi \in L^2(\Omega)$  such that  $\mathcal{F}_{K_1}^{-1}(\phi|_{K_1}) = \hat{\phi}^{v_2}(\xi, \eta)$

Figure 8 – Example of an  $L^2(\Omega)$  vertex function

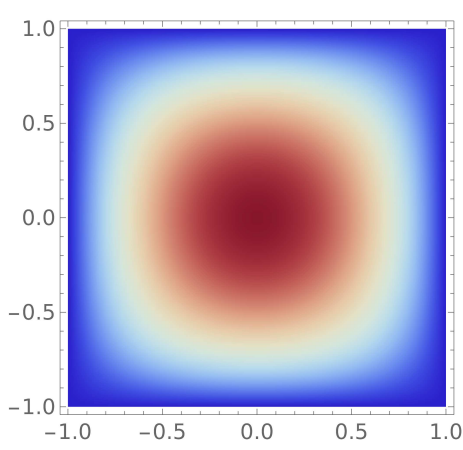
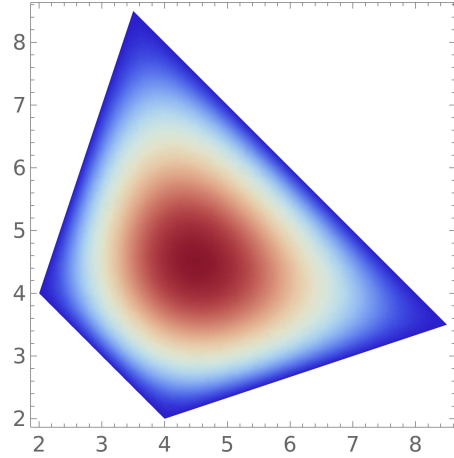


(a)  $\hat{\phi}^{e_{1,0}}(\xi, \eta)$



(b)  $\phi \in L^2(\Omega)$  such that  $\mathcal{F}_{K_1}^{-1}(\phi|_{K_1}) = \hat{\phi}^{e_{1,0}}(\xi, \eta)$

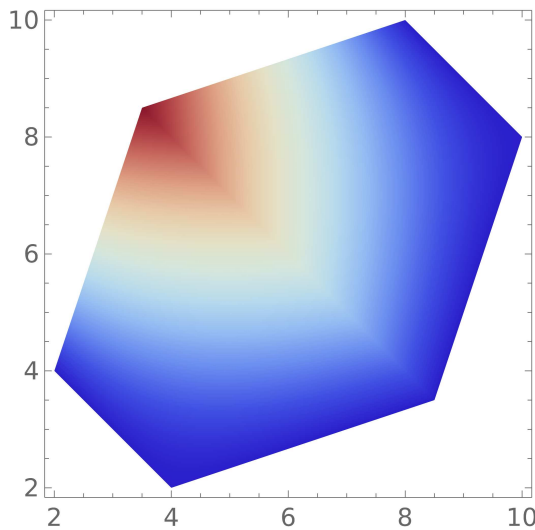
Figure 9 – Example of an  $L^2(\Omega)$  edge function

(a)  $\hat{\phi}^{f,0,0}(\xi, \eta)$ (b)  $\phi \in L^2(\Omega)$  such that  $\mathcal{F}_{K_1}^{-1}(\phi|_{K_1}) = \hat{\phi}^{f,0,0}(\xi, \eta)$ Figure 10 – Example of an  $L^2(\Omega)$  face function $H^1(\Omega)$ -conforming shape functions

The generation of  $H^1(\Omega)$  shape functions is similar to the creation of the  $L^2(\Omega)$  finite space. The main difference is that shape functions associated to vertices, edges and faces may be extended to adjacent elements to ensure continuity of the space.

$H^1(\Omega)$ -conforming shape functions are also created by backtracing polynomials defined on the reference element, but if the shape function is associated to a side that is shared by multiples elements, the *NeoPZ* structure ensures that the mapped polynomials are oriented correctly and share the same degree of freedom.

Figures 11, 12, and 13 illustrate  $H^1(\Omega)$ -conforming vertex, edge and face functions on the partition presented on Figure 7 respectively.

Figure 11 –  $\phi \in H^1(\Omega)$  such that  $\mathcal{F}_{K_1}^{-1}(\phi|_{K_1}) = \hat{\phi}^{v_2}(\xi, \eta)$  and  $\mathcal{F}_{K_2}^{-1}(\phi|_{K_2}) = \hat{\phi}^{v_3}(\xi, \eta)$

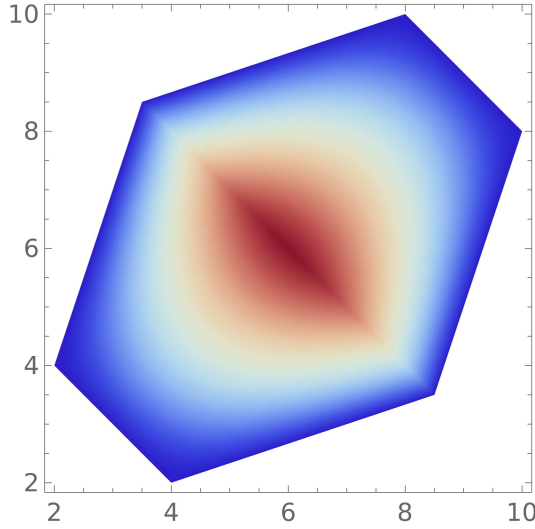


Figure 12 –  $\phi \in H^1(\Omega)$  such that  $\mathcal{F}_{K_1}^{-1}(\phi|_{K_1}) = \hat{\phi}^{e_1,0}(\xi, \eta)$  and  $\mathcal{F}_{K_2}^{-1}(\phi|_{K_2}) = \hat{\phi}^{e_3,0}(\xi, \eta)$

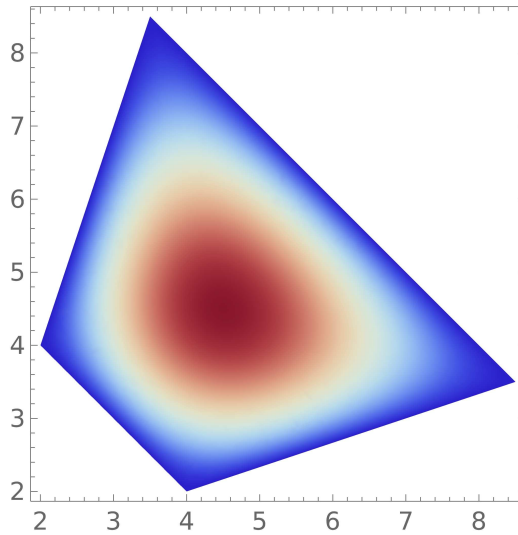


Figure 13 –  $\phi \in H^1(\Omega)$  such that  $\mathcal{F}_{K_1}^{-1}(\phi|_{K_1}) = \hat{\phi}^{f,0,0}(\xi, \eta)$

### $H(\text{div}, \Omega)$ -conforming shape functions

The generation of  $H(\text{div}, \Omega)$ -conforming shape functions in *NeoPZ* is treated in [CASTRO et al., 2016] and [DEVLOO et al., 2016]. The central idea is that functions on the reference element are defined by the multiplication of scalar polynomials and constant vector fields.

There are no  $H(\text{div}, \Omega)$ -conforming functions associated with vertices.  $H(\text{div}, \Omega)$  shape functions are either associated with faces or to volumes in three-dimensional elements.

For scalar-valued functions, the polynomials are mapped from the reference element  $\hat{K}$  to the geometric element  $K$  by the same geometric transformation that deforms  $\hat{K}$  into  $K$ . This transformation, however, does not preserve the normal continuity required by the  $H(\text{div}, \Omega)$  space.

For  $H(\text{div}, \Omega)$ -conforming shape functions the contravariant Piola transformation  $\mathcal{F}_{\text{div}, K}$  is employed. Let  $\hat{\phi} = \hat{\phi} \cdot \hat{\mathbf{v}}$  a vector-valued function defined on  $\hat{K}$  by the multiplication of polynomial  $\hat{\phi}$  and an appropriate constant vector  $\hat{\mathbf{v}}$ , the mapped function  $\phi$  is given by:

$$\phi = \mathcal{F}_{\text{div}, K}(\hat{\phi}) = \mathcal{F}_K \cdot \left[ \frac{1}{\det(\mathbf{J}_K)} \mathbf{J}_K \hat{\phi} \right], \quad (2.17)$$

where  $\mathbf{J}_K$  is the Jacobian matrix of the transformation  $\mathcal{F}_K$ .

The constant vectors  $\hat{\mathbf{v}}_i$ ,  $i = 0, \dots, 17$ , of the quadrilateral element are shown in Figure 14.

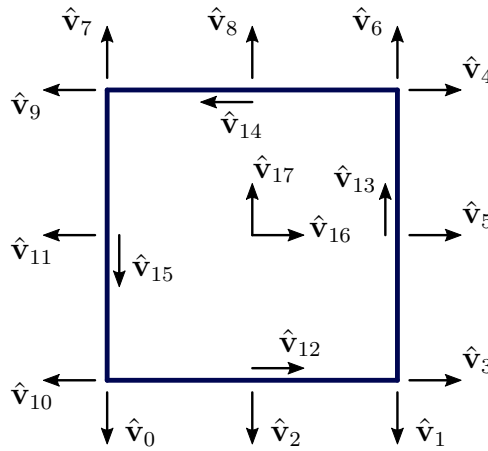


Figure 14 – Constant vector fields defined on the quadrilateral element

Examples of  $H(\text{div}, \Omega)$  shape functions on the reference element are shown in Figure 15.

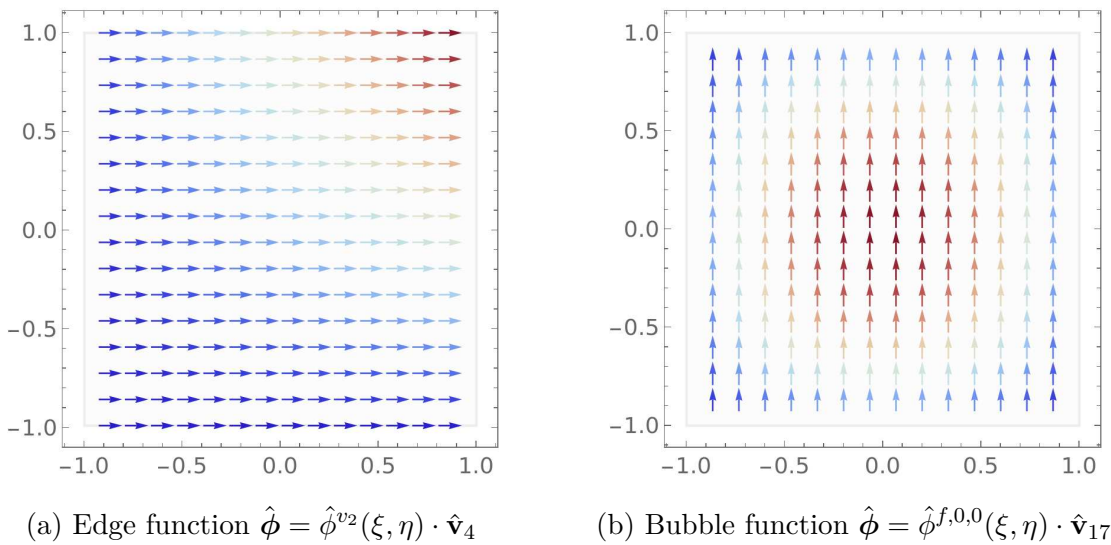


Figure 15 – Examples of  $H(\text{div}, \Omega)$  functions on the reference element

Mapped  $H(\text{div}, \Omega)$ -conforming shape functions are illustrated in Figures 16 and 17.

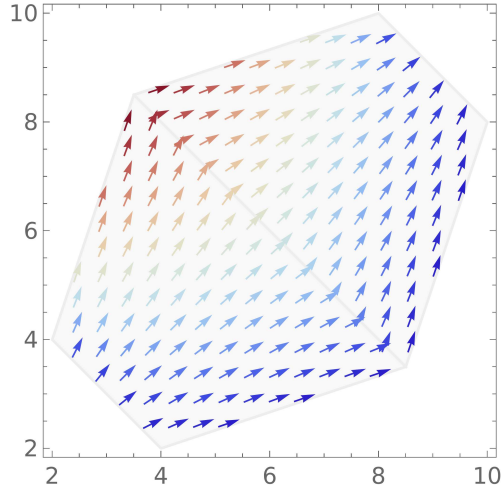


Figure 16 – Example of an edge quadrilateral  $H(\text{div}, \Omega)$  function  $\phi \in H(\text{div}, \Omega)$  such that  $\mathcal{F}_{\text{div}, K_1}^{-1}(\phi|_{K_1}) = \hat{\phi}^{v_2}(\xi, \eta) \cdot \hat{\mathbf{v}}_4$  and  $\mathcal{F}_{\text{div}, K_2}^{-1}(\phi|_{K_2}) = -\hat{\phi}^{v_3}(\xi, \eta) \cdot \hat{\mathbf{v}}_9$

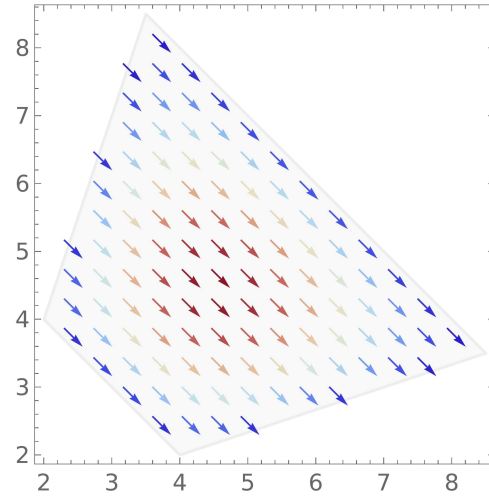


Figure 17 – Example of an edge quadrilateral  $H(\text{div}, \Omega)$  function  $\phi \in H(\text{div}, \Omega)$  such that  $\mathcal{F}_{\text{div}, K_1}^{-1}(\phi|_{K_1}) = \hat{\phi}^{f,0,0}(\xi, \eta) \cdot \hat{\mathbf{v}}_{17}$

### 2.2.3 Finite element spaces

#### Polynomial spaces $P_k$

The starting point for constructing finite element spaces is the definition of a scalar polynomial space on the reference element  $\hat{K}$ . Consider  $P_k(\hat{K})$  the scalar polynomials of total degree at most  $k$ .

#### $L^2(\Omega)$ -conforming finite element space

Finite dimensional spaces  $U_h \subset L^2$  are constructed by backtracking polynomial spaces defined in the master element such that:

$$U_h = \{u \in L^2(\Omega) : \mathcal{F}_K^{-1}(u|_K) \in P_k(\hat{K}), \quad \forall K \in \mathcal{T}_h\}.$$

$H^1(\Omega)$ -conforming finite element space

Analogously, finite dimensional spaces  $V_h \subset H^1$  are constructed as follows:

$$V_h = \{v \in H^1(\Omega) : \mathcal{F}_K^{-1}(v|_K) \in P_k(\hat{K})\}, \quad \forall K \in \mathcal{T}_h.$$

$H(\text{div}, \Omega)$ -conforming finite element space

Finite dimensional spaces  $\mathbf{V}_h \subset H(\text{div}, \Omega)$  are constructed by backtracking vector polynomial spaces  $\mathbf{P}_k = [P_k]^d$  defined in the master element:

$$\mathbf{V}_h = \{\mathbf{q} \in H(\text{div}, \Omega) : \mathcal{F}_{\text{div}, K}^{-1}(\mathbf{q}|_K) \in \mathbf{P}_k^d(\hat{K})\}, \quad \forall K \in \mathcal{T}_h.$$

### 3 Classical finite element formulations

In this chapter, the model problem and classical finite element methods are presented, namely the primal  $H^1(\Omega)$  and mixed formulation.

#### 3.1 The model problem

Let  $\Omega \subset \mathbb{R}^d$ ,  $d = 2, 3$ , an open, bounded Lipschitz domain with boundary  $\partial\Omega$ . The outward normal vector field of  $\partial\Omega$  is denoted by  $\mathbf{n}$ . The boundary  $\partial\Omega$  is decomposed into two disjoint parts  $\Gamma_D$  and  $\Gamma_N$ . A diagram of  $\Omega$  is shown in Figure 18.

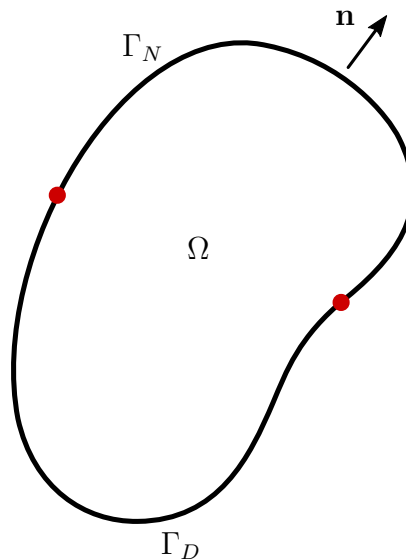


Figure 18 – Problem domain with boundary parts  $\Gamma_D$ ,  $\Gamma_N$  and outward unit normal field  $\mathbf{n}$

The phenomenon of flow in porous media, in the steady state, is governed by Darcy's equation:

$$-\nabla \cdot \mathbb{K} \nabla u = f \text{ in } \Omega, \quad (3.1)$$

along with the boundary conditions:

$$\begin{aligned} u &= u_D \text{ on } \Gamma_D, \\ \mathbb{K} \nabla u \cdot \mathbf{n} &= \sigma_N \text{ on } \Gamma_N, \end{aligned}$$

where  $f \in L^2(\Omega)$ ,  $u_D \in H^{1/2}(\Gamma_D)$  and  $\sigma_N \in H^{-1/2}(\Gamma_N)$ .

Here,  $u$  represents the pressure field to be calculated. The other variables are defined by the problem statement, specifically,  $\mathbb{K}$  is a symmetric, positive definite

permeability tensor and  $f$  is an arbitrary function in  $L^2(\Omega)$ . On  $\Gamma_D$  the function value is prescribed (Dirichlet boundary condition) and on  $\Gamma_N$  the normal derivative is prescribed (Neumann boundary condition).

Frequently, in problems that arise in petroleum engineering, the variable of interest is not the pressure field, but rather the flux, denoted  $\boldsymbol{\sigma}$ , which relates to the pressure gradient. Equation 3.1 is rewritten in terms of  $\boldsymbol{\sigma}$  as follows:

$$\boldsymbol{\sigma} = -\mathbb{K}\nabla u \text{ in } \Omega, \quad (3.2)$$

$$\nabla \cdot \boldsymbol{\sigma} = f \text{ in } \Omega. \quad (3.3)$$

## 3.2 Primal $H^1(\Omega)$ formulation

The primal  $H^1(\Omega)$  formulation [BECKER; CAREY; ODEN, 1981] is the most popular method due to its simplicity and ease of implementation. Its statement reads: find  $u \in H_{u_D}^1(\Omega)$  such that  $\forall v \in H_0^1(\Omega)$  the following holds:

$$\int_{\Omega} \mathbb{K}\nabla u \nabla v \, dx = \int_{\Omega} f v \, dx + \int_{\Gamma_N} \sigma_N v \, ds \quad (3.4)$$

The discrete version of 3.4 seeks an approximation of  $u$ , denoted by  $u_h$ , in a finite dimensional subspace  $V_h \subset H^1(\Omega)$ . The problem reads: Find  $u_h$  such that  $u_h = u_D$  on  $\Gamma_D$  and  $\forall v_h \in V_h \subset H_0^1(\Omega)$ :

$$\int_{\Omega} \mathbb{K}\nabla u_h \nabla v_h \, dx = \int_{\Omega} f v_h \, dx + \int_{\Gamma_N} \sigma_N v_h \, ds \quad (3.5)$$

We can write as the variational formulation:

$$a(u_h, v_h) = f(v_h)$$

where  $a(u_h, v_h)$  is the bilinear term:

$$a(u_h, v_h) = \int_{\Omega} \mathbb{K}\nabla u_h \nabla v_h \, dx$$

and  $f(v_h)$  is the linear term:

$$f(v_h) = \int_{\Omega} f v_h \, dx + \int_{\Gamma_N} \sigma_N v_h \, ds.$$

Since our solution is a linear combination of the elements of  $V_h$ , which are its basis functions  $\phi_i : i \leq n$ , where  $n$  is the cardinality of  $V_h$ , we write  $u_h = \sum_{i=0}^n \alpha_i \phi_i$ . Which leads to the matricial form:

$$\mathbf{K} \cdot \boldsymbol{\alpha} = \mathbf{f},$$

where  $\mathbf{K} = (k_{ij}) = a(\phi_i, \phi_j)$ ,  $\boldsymbol{\alpha}^T = (\alpha_i)$  and  $\mathbf{f} = f(\phi_j)$ .

This method solves a continuous pressure field  $u_h$ . If a flux approximation  $\boldsymbol{\sigma}_h$  is desired, it can be computed by post-processing the pressure variable through the calculation of  $\boldsymbol{\sigma}_h = -\mathbb{K}\nabla u_h$  over each element. However, this yields a non-conservative vector-field with lower accuracy order.

### 3.3 $H(\operatorname{div}, \Omega)$ -conforming mixed formulation

Mixed methods, introduced in [RAVIART; THOMAS, 1977], are adequate for applications where the flux field is the variable of interest. In the mixed formulation, we solve for a vector-valued flux field and a discontinuous pressure simultaneously. The pressure variable in this case acts as a Lagrange multiplier, constraining the divergence equation. The flux field is  $H(\operatorname{div}, \Omega)$ -conforming, meaning that the continuity of the normal component is ensured, satisfying local mass conservation.

The flux solved by mixed methods have higher convergence rates than the primal  $H^1(\Omega)$  method. A comparison between different approximation schemes methods in 2D applications is available in [FORTI et al., 2016].

The weak statement of the mixed method reads: find  $\boldsymbol{\sigma}, u \in H_{\sigma_N}(\operatorname{div}, \Omega) \times L^2(\Omega)$  such that for all  $\mathbf{q}, v \in H_0(\operatorname{div}, \Omega) \times L^2(\Omega)$  there holds:

$$\begin{aligned} \int_{\Omega} \mathbb{K}^{-1} \boldsymbol{\sigma} \cdot \mathbf{q} \, dx - \int_{\Omega} u \nabla \cdot \mathbf{q} \, dx &= - \int_{\Gamma_D} u_D \mathbf{q} \cdot \mathbf{n} \, ds \\ \int_{\Omega} \nabla \cdot \boldsymbol{\sigma} v \, dx &= \int_{\Omega} f v \, dx \end{aligned} \quad (3.6)$$

#### 3.3.1 Finite-dimensional space pairs for mixed approximations

In mixed methods, we consider a pair of approximation spaces  $\mathbf{V}_h \subset H(\operatorname{div}, \Omega)$  and  $U_h \subset L^2(\Omega)$ , piecewise defined over the elements  $K$  of the partition  $\mathcal{T}_h$ .  $\mathbf{V}_h$  and  $U_h$  are created by backtracking a vector polynomial space  $\hat{\mathbf{V}}$  and a scalar polynomial space  $\hat{U}$  defined on the reference element  $\hat{K}$ . For stability, De Rham's property needs to hold:

$$\nabla \cdot \hat{\mathbf{V}} \equiv \hat{U}.$$

A natural choice is to approximate the flux variable by a vector-valued polynomial space  $\mathbf{P}_k = [P_k]^d$  and the pressure by a scalar-valued polynomial space  $P_{k-1}$ . This family corresponds to the Brezzi-Douglas-Marini approximation space BDM for triangles and tetrahedra [BREZZI; DOUGLAS; MARINI, 1985], but does not hold for quadrilateral, prism and hexahedra geometries.

There exists a variety of stable finite element pairs  $\mathbf{V}(\hat{K}) \times U(\hat{K})$ , using different polynomial functions according to the element geometry [BOFFI; BREZZI; FORTIN, 2013; FUENTES et al., 2015].

#### Enriched spaces $\mathbf{V}_{h,k}^{n+}$ and $U_{h,k}^{n+}$

In this work we consider the enriched spaces  $\mathbf{V}_{h,k}^{n+}$  and  $U_{h,k}^{n+}$  deocumented in [DEVLOO; FARIAS; GOMES, 2019].

Let  $\hat{\mathbf{V}} = \hat{\mathbf{V}}^\partial \oplus \hat{\mathbf{V}}^\circ$  a direct factorization of  $\hat{\mathbf{V}}$ , where  $\hat{\mathbf{V}}^\circ$  is spanned by interior shape functions, with vanishing normal components over all element edges, and  $\hat{\mathbf{V}}^\partial$  is spanned by external functions, with non-zero normal component over an edge. The divergence space is of the form  $\nabla \cdot \hat{\mathbf{V}} = \hat{U} = \hat{U}_0 \oplus \hat{U}^\perp$ , where  $\hat{U}_0$  are constant functions and  $\hat{U}^\perp$  are functions with zero mean, such that  $\hat{U}^\perp = \nabla \cdot \hat{\mathbf{V}}^\circ$ .

Let  $\hat{\mathbf{V}}_k = \hat{\mathbf{V}}_k^\partial \oplus \hat{\mathbf{V}}_k^\circ$  a space spanned by vector polynomials of order  $k$  defined on the reference element. The enriched versions  $\hat{\mathbf{V}}_k^{n+}$ ,  $n \geq 1$ , are created by adding internal shape functions of degree  $k + n$ , while maintaining the external fluxes at order  $k$ :

$$\hat{\mathbf{V}}_k^{n+} = \hat{\mathbf{V}}_k^\partial \oplus \hat{\mathbf{V}}_{k+n}^\circ.$$

With the corresponding enriched divergence space:

$$\hat{U}_k^{n+} = \nabla \cdot \hat{\mathbf{V}}_k^{n+} = \hat{U}_{k+n}.$$

These types of spaces are able to enhance the accuracy of the pressure approximation.

### 3.3.2 Finite element formulation

The finite element version of the mixed method reads: find  $(\boldsymbol{\sigma}_h, u_h) \in \mathbf{V}_h \times U_h \subset H_{\sigma_N}(\text{div}, \Omega) \times L^2(\Omega)$  with  $-\boldsymbol{\sigma}_h \cdot \mathbf{n} = \sigma_N$  on  $\Gamma_N$  such that for all  $(\mathbf{q}_h, v_h) \in \mathbf{V}_h \times U_h$  there holds:

$$\int_{\Omega} \mathbb{K}^{-1} \boldsymbol{\sigma}_h \mathbf{q}_h \, dx - \int_{\Omega} u_h \nabla \cdot \mathbf{q}_h \, dx = - \int_{\Gamma_D} u_D \mathbf{q}_h \cdot \mathbf{n} \, ds \quad (3.7)$$

$$\int_{\Omega} \nabla \cdot \boldsymbol{\sigma}_h v_h \, dx = \int_{\Omega} f v_h \, dx \quad (3.8)$$

Equations (3.7)-(3.8) can be written in the form:

$$\begin{bmatrix} \mathbf{A} & \mathbf{B}^T \\ \mathbf{B} & 0 \end{bmatrix} \cdot \begin{bmatrix} \boldsymbol{\alpha}_\sigma \\ \boldsymbol{\alpha}_u \end{bmatrix} = \begin{bmatrix} \mathbf{f}_\Gamma \\ \mathbf{f}_f \end{bmatrix},$$

with

$$\begin{aligned} \mathbf{A} &= (a_{ij}) = \int_{\Omega} \mathbb{K}^{-1} \boldsymbol{\phi}_i \boldsymbol{\phi}_j \, dx, \\ \mathbf{B} &= (b_{ij}) = \int_{\Omega} \nabla \cdot \boldsymbol{\phi}_i \boldsymbol{\phi}_j \, dx, \\ \mathbf{f}_\Gamma &= - \int_{\Gamma_D} u_D \boldsymbol{\phi}_j \cdot \mathbf{n} \, ds, \\ \mathbf{f}_f &= \int_{\Omega} f \boldsymbol{\phi}_j \, dx. \end{aligned}$$

The terms  $\boldsymbol{\alpha}_\sigma$  and  $\boldsymbol{\alpha}_u$  are the coefficients that multiply the basis functions  $\boldsymbol{\phi}_i, u_i$  of the flux and pressure approximation spaces respectively.

### Static condensation

Static condensation is a technique employed to reduce the number of degrees of freedom of a linear system. It modifies the original problem such that secondary degrees of freedom are removed (condensed) from the system of equations and solved at a later stage.

Typically, mixed finite element methods yield a much bigger linear system when compared to the classical  $H^1(\Omega)$  formulation. However, in the mixed approximations, a great percentage of the shape functions is internal, which makes static condensation highly efficient and, ultimately, allows for its competitiveness.

The set of equations of a mixed element can be partitioned in terms of the coefficients that multiply the basis functions corresponding to internal fluxes  $\alpha_{\sigma,i}$ , external fluxes  $\alpha_{\sigma,e}$ , a constant average pressure  $\alpha_{u,0}$  and the remainder pressure degrees of freedom  $\alpha_{u,i}$ :

$$\left[ \begin{array}{cc|cc} \mathbf{A}_{ii} & \mathbf{B}_{ii}^T & \mathbf{B}_{ie}^T & \mathbf{A}_{ie} \\ \mathbf{B}_{ii} & 0 & 0 & \mathbf{B}_{ie} \\ \hline \mathbf{B}_{ie} & 0 & 0 & \mathbf{B}_{ee} \\ \mathbf{A}_{ei} & \mathbf{B}_{ie}^T & \mathbf{B}_{ee}^T & \mathbf{A}_{ee} \end{array} \right] \cdot \begin{bmatrix} \alpha_{\sigma,i} \\ \alpha_{u,i} \\ \alpha_{u,0} \\ \alpha_{\sigma,e} \end{bmatrix} = \begin{bmatrix} \mathbf{f}_\Gamma \\ \mathbf{f}_{f,i} \\ f_{f,0} \\ 0 \end{bmatrix}, \quad (3.9)$$

where,  $\mathbf{f}_\Gamma$  is the contribution to the load vector of the Dirichlet and Robin boundary conditions,  $\mathbf{f}_{f,i}$  is the contribution of the source term associated with scalar shape functions to be condensed and  $f_{f,0}$  the contribution of the source term associated with the constant pressure.

Which can be rewritten as:

$$\left[ \begin{array}{c|c} \mathbf{K}_{ii} & \mathbf{K}_{ie} \\ \hline \mathbf{K}_{ei} & \mathbf{K}_{ee} \end{array} \right] \cdot \begin{bmatrix} \alpha_i \\ \alpha_e \end{bmatrix} = \begin{bmatrix} \mathbf{f}_i \\ \mathbf{f}_e \end{bmatrix}$$

Isolating  $\alpha_i$  we obtain:

$$\alpha_i = \mathbf{K}_{ii}^{-1} (\mathbf{f}_i - \mathbf{K}_{ie} \cdot \alpha_e) \quad (3.10)$$

Doing the same for  $\mathbf{f}_e$  gives us:

$$\mathbf{K}_{ei} \cdot \alpha_i + \mathbf{K}_{ee} \cdot \alpha_e = \mathbf{f}_e \quad (3.11)$$

Substituting Equation 3.10 in 3.11 yields:

$$\left( \mathbf{K}_{ee} - \mathbf{K}_{ei} \cdot \mathbf{K}_{ii}^{-1} \cdot \mathbf{K}_{ie} \right) \alpha_e = \mathbf{f}_e - \mathbf{K}_{ei} \cdot \mathbf{K}_{ii}^{-1} \cdot \mathbf{f}_i \quad (3.12)$$

We now obtain a system with only degrees of freedom corresponding to the primary degrees of freedom:

$$\tilde{\mathbf{K}} \cdot \alpha_e = \tilde{\mathbf{f}}, \quad (3.13)$$

where  $\tilde{\mathbf{K}} = \mathbf{K}_{ee} - \mathbf{K}_{ei} \cdot \mathbf{K}_{ii}^{-1} \cdot \mathbf{K}_{ie}$  and  $\tilde{\mathbf{f}} = \mathbf{f}_e - \mathbf{K}_{ei} \cdot \mathbf{K}_{ii}^{-1} \cdot \mathbf{f}_i$ .

The internal degrees of freedom  $\alpha_i$  are called *secondary* and are solved at a later stage by the substitution of  $\alpha_e$  in Equation 3.10.

Remark that using static condensation, the global condensed system of pairs  $\mathbf{V}_{h,k}^{n+}$  and  $U_{h,k}^{n+}$  have the same number of degrees of freedom regardless of the choice for  $n$ , since the number of primary degrees of freedom is proportional to the number of *external* flux functions and  $n$  refers to the enrichment level for the internal functions.

## 4 The MHM-H(div)- $\mathcal{E}_\gamma$ method

The focus of the current study is on a posteriori error estimation for the multiscale hybrid-mixed finite element method, MHM-H(div)- $\mathcal{E}_\gamma$ , versions of formulation (3.6), recently proposed in the [DURÁN et al., 2019]. The multiscale framework allows the incorporation of fine scale effects internally of the coarse elements, while keeping only coarse scale degrees of freedom in the global linear system.

As shall be detailed in next sections, in addition to the flux and potential variables, hybridization occurs by a domain decomposition and by the introduction of a new unknown  $\lambda$  representing the normal trace of the flux  $\boldsymbol{\sigma}$  over subregion boundaries.

### 4.1 Concepts regarding geometry

The hybrid mixed variational finite element formulations for (3.6) shall be presented here as subordinated to a conformal partition  $\mathcal{T} = \{\Omega_i\}$  of  $\Omega$  by non-overlapping subdomains  $\Omega_i$ , which may have one of the usual element geometry. The union of all facets  $F \subset \partial\Omega_i$  of the subregions (edges in 2D or faces in 3D) is called the skeleton  $\Gamma$ .

We set a partition  $\mathcal{T}^\Gamma$  of  $\Gamma$  by the conglomeration of facet sub-partitions  $\mathcal{T}^F$ . Refined conformal sub-partitions  $\mathcal{T}^{\Omega_i} = \{K\}$  are also defined inside the subdomains. The following mesh consistency property is supposed to hold.

*Mesh consistency:* the elements in  $\mathcal{T}^\Gamma$  included in  $\partial\Omega_i$  are coarser than (or equal to) the ones induced on  $\partial\Omega_i$  by the partitions  $\mathcal{T}^{\Omega_i}$ .

In other words, mesh consistency means that the partition induced by  $\mathcal{T}^{\Omega_i}$  over a facet  $F \subset \partial\Omega_i$  is a refinement of the partition  $\mathcal{T}^\Gamma|_F$ . The method can deal with non-conformal  $\mathcal{T}^{\Omega_i}$  and  $\mathcal{T}^{\Omega_j}$  over interfaces  $\Gamma_{i,j} = \partial\Omega_i \cap \partial\Omega_j$  between neighboring subdomains  $\Omega_i$  and  $\Omega_j$ . However, for the definition of the potential reconstruction only the conformal cases are treated.

### 4.2 Finite element space settings

For flux and potential discretizations, the method is based on a finite element pair  $\mathbf{V}_\gamma \times \mathcal{W}_{\gamma_{in}} \subset H(\text{div}, \Omega) \times L^2(\Omega)$  obtained by the assembly of local divergence-consistent finite element pairs  $\mathcal{V}_\gamma(\Omega_i) \times \mathcal{W}_{\gamma_{in}}(\Omega_i)$  defined in each  $\Omega_i \in \mathcal{T}$ . Similarly, a finite element trace space  $\Lambda_\gamma$  of piecewise polynomials over the partition  $\mathcal{T}^\Gamma$  is required. The index  $\gamma = (\gamma_{in}, \gamma_{sk})$  is used to represent discretization parameters  $\gamma_{in}$  and  $\gamma_{sk}$  (mesh widths and polynomial degrees) associated to refined and coarse scale levels, which shall be specified

in some examples presented in Section 4.5. In summary, the following hypotheses shall be assumed in the definition of these local finite element spaces.

*Refined divergence-consistent finite element pairs*  $\mathcal{V}_{\gamma_{in}}(\Omega_i) \times \mathcal{U}_{\gamma_{in}}(\Omega_i)$  constructed on top of the partitions  $\mathcal{T}^{\Omega_i}$ :

$$\begin{aligned}\mathcal{V}_{\gamma_{in}}(\Omega_i) &= \left\{ \boldsymbol{\tau} \in H(\text{div}, \Omega_i); \boldsymbol{\tau}|_K \in \mathbf{V}_h(K), \forall K \in \mathcal{T}^{\Omega_i} \right\}, \\ \mathcal{U}_{\gamma_{in}}(\Omega_i) &= \left\{ u \in L^2(\Omega_i); u|_K \in U_h(K), \forall K \in \mathcal{T}^{\Omega_i} \right\},\end{aligned}$$

verifying  $\nabla \cdot \mathcal{V}_{\gamma_{in}}(\Omega_i) = \mathcal{U}_{\gamma_{in}}(\Omega_i)$ . Notice that  $\mathcal{V}_{\gamma_{in}}(\Omega_i)$  admits a direct sum decomposition  $\mathcal{V}_{\gamma_{in}}(\Omega_i) = \mathcal{V}_{\gamma_{in}}^\partial(\Omega_i) \oplus \mathring{\mathcal{V}}_{\gamma_{in}}(\Omega_i)$ , the vector functions  $\boldsymbol{\tau} \in \mathring{\mathcal{V}}_{\gamma_{in}}(\Omega_i)$  having vanishing normal traces  $\boldsymbol{\tau} \cdot \mathbf{n}^{\Omega_j}|_{\partial\Omega_i} = 0$  (bubble flux functions). The functions  $\boldsymbol{\tau} \in \mathcal{V}_{\gamma_{in}}^\partial(\Omega_i)$  (of facet type) are supported in the layer of elements  $K \in \mathcal{T}^{\Omega_i}$  having a facet included in  $\partial\Omega_i$ .

*Local trace finite element spaces*  $\Lambda_\gamma(F)$  are piecewisely defined over the elements of  $\mathcal{T}^F$  backtracking scalar polynomials of their corresponding master elements. The discretization parameters are assumed to be  $\gamma_{sk}$  on the internal facets  $F \cap \partial\Omega = \emptyset$  and  $\gamma_{in}$  otherwise. The next property is crucial for the trace constraint operation.

*Trace consistency:* for  $F \subset \partial\Omega_i$  the finite element trace subspace  $\Lambda_{\gamma_{in}}(F) = \{\boldsymbol{\tau} \cdot \mathbf{n}|_F; \boldsymbol{\tau} \in \mathcal{V}_{\gamma_{in}}(\Omega_i)\}$  contains  $\Lambda_\gamma(F)$ .

*Constrained finite element spaces in  $\Omega_i$ :* assuming the aforementioned conditions, we introduce constrained vector finite element spaces

$$\mathcal{V}_\gamma(\Omega_i) = \left\{ \boldsymbol{\tau} \in \mathcal{V}_{\gamma_{in}}(\Omega_i); \boldsymbol{\tau} \cdot \mathbf{n}|_F \in \Lambda_\gamma(F), F \subset \partial(\Omega_i) \right\}.$$

Due to the trace consistency property, the constrained vector space  $\mathcal{V}_\gamma(\Omega_i)$  is well defined. Moreover, their decompositions in terms of facet and bubble components become  $\mathcal{V}_\gamma(\Omega_i) = \mathcal{V}_\gamma^\partial(\Omega_i) \oplus \mathring{\mathcal{V}}_{\gamma_{in}}(\Omega_i)$ . The facet fluxes in  $\mathcal{V}_\gamma^\partial(\Omega_i)$  have coarser resolution  $\gamma_{sk}$  over  $\partial\Omega_i \setminus \partial\Omega$ . Moreover, the divergence-compatibility property  $\nabla \cdot \mathcal{V}_\gamma(\Omega_i) = \mathcal{U}_{\gamma_{in}}(\Omega_i)$  is preserved.

*Finite element space setting*  $\mathcal{E}_\gamma = \mathbf{V}_\gamma \times U_{\gamma_{in}} \times \Lambda_\gamma$  : let  $\mathcal{V}_\gamma \times \mathcal{U}_{\gamma_{in}} \subset H(\text{div}, \Omega) \times L^2(\Omega)$ , be the divergence-consistent finite element pair whose restrictions to  $\Omega_i \in \mathcal{T}$  are the local finite element pairs  $\mathcal{V}_\gamma(\Omega_i) \times \mathcal{U}_{\gamma_{in}}(\Omega_i)$ . Similarly, let  $\Lambda_\gamma \subset L^2(\Gamma)$  be composed by trace functions  $\mu \in L^2(\Gamma)$  whose restrictions on  $F \subset \Gamma$  are in  $\Lambda_\gamma(F)$ . By construction,  $\boldsymbol{\tau} \cdot \mathbf{n}|_\Gamma \in \Lambda_\gamma$ , for all  $\boldsymbol{\tau} \in \mathbf{V}_\gamma$ .

Uniformly bounded projection-based interpolants ([DEMKOWICZ, 2008; DURÁN et al., 2019]) Define the projection operator  $\mathbf{\Pi}_\gamma^\sigma : H^1(\Omega_i, \mathbb{R}^d) \rightarrow \mathbf{V}_\gamma$  such that

$$\int_{\Omega} \nabla \cdot (\boldsymbol{\tau} - \mathbf{\Pi}_\gamma^\sigma \boldsymbol{\tau}) \psi dx = 0, \quad \forall \psi \in \mathcal{U}_{\gamma_{in}}, \quad (4.1)$$

meaning that  $\nabla \cdot \mathbf{\Pi}_\gamma^\sigma \boldsymbol{\tau} = \Pi_{\gamma_{in}} \nabla \cdot \boldsymbol{\tau}$ , where  $\Pi_{\gamma_{in}} : L^2(\Omega) \rightarrow U_{\gamma_{in}}$  is the  $L^2$ -orthogonal projection. Moreover, in the definition of  $\mathbf{\Pi}_\gamma^\sigma$  the property  $\int_{\partial\Omega_i} (\boldsymbol{\tau} - \mathbf{\Pi}_\gamma^\sigma \boldsymbol{\tau}) \cdot \mathbf{n}_i^\Omega \mu ds = 0, \quad \forall \mu \in \Lambda_\gamma$  is also enforced. This projection operator allows to demonstrate that the De Rham divergence commutative property holds for the finite element pair  $(\mathbf{V}_\gamma, U_{\gamma_{in}})$ , an essential property for demonstrating the convergence of mixed finite element approximations.

Procedures for the construction of hierarchic partitions and space settings verifying mesh and trace consistency properties are described in Sec. 4.5: there are general purpose two-level settings and two  $h$ -adaptive procedures (for subregion and skeleton trace adaptations). The example of Figure 19 gives an illustration of a two-level finite element space setting: a macro-partition  $\mathcal{T}$  of  $3 \times 3$  square subregions  $\Omega_i$ , local refined partitions  $\mathcal{T}^{\Omega_i}$ , skeleton partition  $\mathcal{T}^\Gamma$ , and examples of parameter discretizations adopted inside the subregions and over the skeleton partition. In this example, the local partitions  $\mathcal{T}^{\Omega_i}$  and  $\mathcal{T}^{\Omega_j}$  are conformal over  $\Gamma_{i,j} = \partial\Omega_i \cap \partial\Omega_j$ . The discretization parameters are  $\gamma_{sk} = (h_{sk}, k_{sk})$ ,  $\gamma_{in} = (h_{in}, k_{in})$ , where  $k_{sk} = 1$ ,  $k_{in} = 2$ ,  $h_{in} = h_{sk}/4$ . Thus mesh consistency and trace consistency are verified. Consequently, the resulting two-level finite element setting  $\mathcal{E}_\gamma = \mathbf{V}_\gamma \times U_{\gamma_{in}} \times \Lambda_\gamma$  is well defined and stable. Examples of adaptive settings are shown in the numerical tests of Sec. 6.3.1.

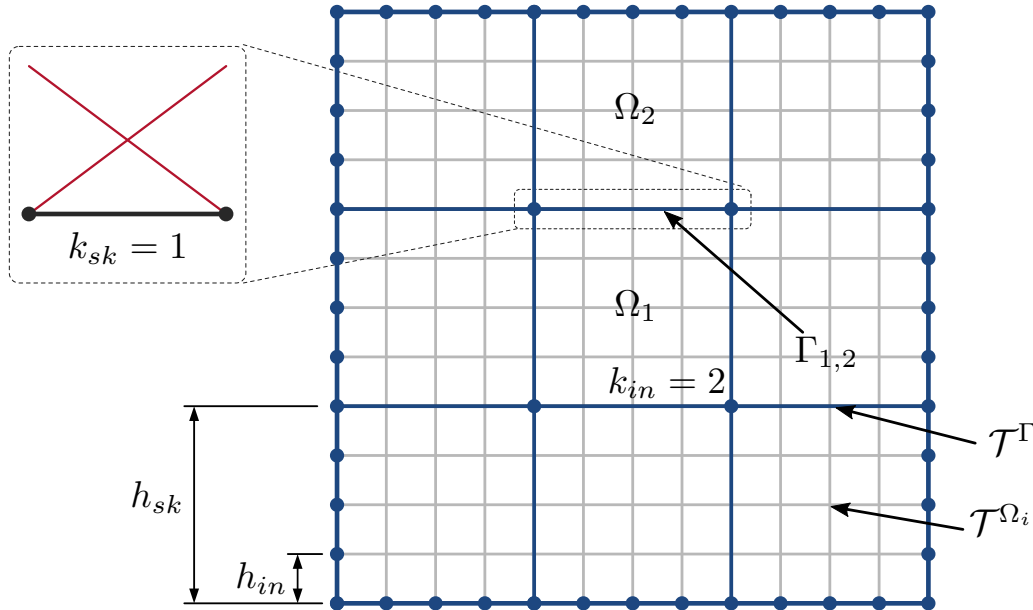


Figure 19 – Example of a hierarchy of partitions  $\mathcal{T}$ ,  $\mathcal{T}^\Gamma$ , and  $\mathcal{T}_{h_{in}}^{\Omega_i}$  for the MHM-H(div)- $\mathcal{E}_\gamma$  method.

### 4.3 Global-local algorithms

The MHM-H(div)- $\mathcal{E}_\gamma$  method can be interpreted as a scheme to compute approximations  $(\tilde{\boldsymbol{\sigma}}, \tilde{u}, \tilde{\lambda}) \in \mathcal{E}_\gamma$  by global-local algorithms, by exploiting the hierarchical structure of the finite element space setting  $\mathcal{E}_\gamma = \mathbf{V}_\gamma \times U_{\gamma_{in}} \times \Lambda_\gamma$ .

1. An orthogonal decomposition  $\tilde{u} = \tilde{u}_0 + \tilde{u}^\perp$  is set for the potential, where  $\tilde{u}_0 \in U_0 \subset U_{\gamma_{in}}$  is piecewise constant over  $\mathcal{T}$ , and  $\tilde{u}^\perp \in U_{\gamma_{in}}^\perp$  is in the  $L^2$ -orthogonal complement of  $U_0$  in  $U_{\gamma_{in}}$ .
2.  $\tilde{\lambda} \in \Lambda_\gamma$  and  $\tilde{u}_0 \in U_0$  are the primary variables computed at the coarse level by a stable global system (upscaling stage).
3.  $\tilde{\boldsymbol{\sigma}} \in \mathbf{V}_\gamma$  and  $\tilde{u}^\perp \in U_{\gamma_{in}}^\perp$  are the secondary variables computed in the refined level by solving a set of completely independent mixed finite element systems, each one restricted to a subregion  $\Omega_i \in \mathcal{T}$  (downscaling stage).

Unlike the MHM-H<sup>1</sup> strategy, [HARDER; PAREDES; VALENTIN, 2013] the MHM-H(div)- $\mathcal{E}_\gamma$  does not use the trace variable  $\tilde{\lambda}$  as a Lagrange multiplier. Instead, the role of  $\tilde{\lambda}$  is to constrain the degrees of freedom required to couple the local mixed problems.

Once  $\tilde{\lambda} \in \Lambda_\gamma$  and  $\tilde{u}_0 \in U_{\gamma_{sk}}$  are computed, the approximate fields  $(\tilde{\boldsymbol{\sigma}}, \tilde{u})$  are determined by the composition

$$\tilde{\boldsymbol{\sigma}} = \boldsymbol{\sigma}^{\tilde{\lambda}} + \boldsymbol{\sigma}^f, \quad \tilde{u} = \tilde{u}_0 + \tilde{u}^\perp = \tilde{u}_0 + u^{\tilde{\lambda}} + u^f, \quad (4.2)$$

where the components of the secondary variables are defined by operators  $\tilde{T}(\tilde{\lambda})$  and  $\hat{T}(f)$  representing well-posed local Neumann boundary value problems. Given  $\mu \in \Lambda_\gamma$ ,  $\tilde{T}(\mu) = (\boldsymbol{\sigma}^\mu, u^\mu) \in \mathbf{V}_\gamma \times U_{\gamma_{in}}^\perp$  verifies  $\boldsymbol{\sigma}^\mu \cdot \mathbf{n}|_{\partial\Omega_i} = \mu|_{\partial\Omega_i}$  and

$$\begin{cases} \int_{\Omega_i} \mathbb{K}^{-1} \boldsymbol{\sigma}^\mu \cdot \mathbf{q} \, dx - \int_{\Omega_i} u^\mu \nabla \cdot \mathbf{q} \, dx = 0, & \forall \mathbf{q} \in \dot{\mathcal{V}}_{\gamma_{in}}(\Omega_i), \\ \int_{\Omega_i} \nabla \cdot \boldsymbol{\sigma}^\mu \varphi \, dx = 0 & \forall \varphi \in U_{\gamma_{in}}^\perp, \end{cases} \quad (4.3)$$

Giving  $f \in L^2(\Omega)$ , consider  $\hat{T}(f) = (\boldsymbol{\sigma}^f, u^f) \in \mathbf{V}_\gamma \times U_{\gamma_{in}}^\perp$  verifying  $\boldsymbol{\sigma}^f \cdot \mathbf{n}|_{\partial\Omega_i} = 0$  and

$$\begin{cases} \int_{\Omega_i} \mathbb{K}^{-1} \boldsymbol{\sigma}^f \cdot \mathbf{q} \, dx - \int_{\Omega_i} u^f \nabla \cdot \mathbf{q} \, dx = 0, & \forall \mathbf{q} \in \dot{\mathcal{V}}_{\gamma_{in}}(\Omega_i), \\ \int_{\Omega_i} \nabla \cdot \boldsymbol{\sigma}^f \varphi \, dx = \int_{\Omega_i} f \varphi \, dx, & \forall \varphi \in U_{\gamma_{in}}^\perp, \end{cases} \quad (4.4)$$

The requirements  $u^\mu, u^f \in U_{\gamma_{in}}^\perp$  are solvability constraints for these pure Neumann boundary condition problems.

The primary variables  $\tilde{u}_0 \in U_0$  and  $\tilde{\lambda} \in \Lambda_\gamma$ , with  $\tilde{\lambda}|_{\Gamma_N} = \Pi_{N,\gamma_{in}} \sigma_N$ , solve the next global system of equations: Find  $\tilde{\lambda} \in \Lambda_\gamma$ , with  $\tilde{\lambda}|_{\Gamma_N} = \Pi_{N,\gamma_{in}} \sigma_N$  and  $\tilde{u}_0 \in U_0$  such that:

$$\begin{cases} \int_{\Omega} \mathbb{K}^{-1} \boldsymbol{\sigma}^{\tilde{\lambda}} \cdot \boldsymbol{\sigma}^\mu dx - \int_{\Omega} \tilde{u}_0 \nabla \cdot \boldsymbol{\sigma}^\mu dx = - \int_{\Omega} \mathbb{K}^{-1} \boldsymbol{\sigma}^f \cdot \boldsymbol{\sigma}^\mu dx - \int_{\Gamma_D} \mu u_D ds, \\ \int_{\Omega} \nabla \cdot \boldsymbol{\sigma}^{\tilde{\lambda}} \varphi dx = \int_{\Omega} f \varphi dx, \end{cases} \quad (4.5)$$

$\forall (\mu, \varphi) \in \Lambda_\gamma \times U_0$ , with  $\mu|_{\Gamma_N} = 0$ , where  $\Pi_{N,\gamma_{in}} \sigma_N$  denotes the orthogonal projection of the Neumann boundary condition onto the space  $\Lambda_\gamma|_{\Gamma_N}$  (which is formed by piecewise polynomials of degree  $k_{in}$  over the facets  $F \in \mathcal{T}^\Gamma$  included in  $\Gamma_N$ ). Observe that the test functions  $\boldsymbol{\sigma}^\mu$  and the target solution  $\boldsymbol{\sigma}^{\tilde{\lambda}}$  are required to solve the local problems (4.3) with Neumann boundary data  $\mu$  and  $\tilde{\lambda}$ , respectively.

#### 4.4 Important properties

There are some crucial properties that qualify the MHM-H(div)- $\mathcal{E}_\gamma$  method as a stable, accurate and efficient option for the model problem. The first one concerns with computational implementation of the MHM-H(div)- $\mathcal{E}_\gamma$  method, the global and local stages being crucial for the construction of an efficient algorithm. They offer the possibility of decomposing the resolution of the problem in terms of expensive, but independent, local solvers that can profit from parallel strategies, and of cheaper coupled global systems. The adopted algorithms correspond to standard static condensation procedures, which can be performed in two computational cycles. The first one applies to assemble and solve the condensed global problem (static condensation applied to macro-subregions  $\Omega_i \in \mathcal{T}$ ): the resulting global system is composed of facet fluxes  $\tilde{\lambda} \in \Lambda_\gamma$  over the skeleton and  $\tilde{u}_0 \in U_0$  and one pressure DoF per macro-subregion. It also provides the downscaling operation for the computation of the secondary internal solutions inside macro elements. Figure 20 illustrates this interpretation.

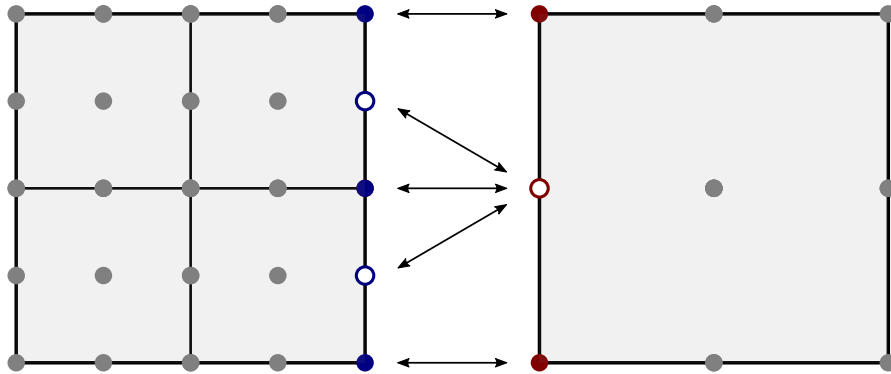


Figure 20 – Interpretation of the upscaling operation as DoF constraints coupling local mixed problems on each macro domain.

Another (optional) static condensation may be employed for order model reduction of the local Neumann solvers occurring in the downscaling operation (static condensation on micro elements  $K \in \mathcal{T}^{\Omega_i}$  using similar principles as for the first level cycle). Other essential properties of the MHM-H(div)- $\mathcal{E}_\gamma$  method are stated in the next theorems as demonstrated in [DURÁN et al., 2019] for full Dirichlet boundary problems. The proofs for the case  $\Gamma_N \neq \emptyset$  are outlined in the Appendix A.1 and Appendix A.2, following similar arguments.

**Theorem 1.** *Uniqueness holds for the solutions of the global and local systems.*

**Theorem 2.** *The MHM-H(div)- $\mathcal{E}_\gamma$  method is equivalent to the well posed mixed formulation for problem (3.2)-(3.3) associated to the finite element spaces  $\mathbf{V}_\gamma \times U_{\gamma_{in}} \subset \mathbf{H}(\text{div}, \Omega) \times L^2(\Omega)$ : find  $\tilde{\boldsymbol{\sigma}} \in \mathbf{V}_\gamma$ , with  $\tilde{\boldsymbol{\sigma}} \cdot \mathbf{n}^\Omega|_{\Gamma_N} = \Pi_{N, \gamma_{in}} \sigma_N$ , and  $\tilde{u} \in U_{\gamma_{in}}$  such that the next equations are verified for all  $\mathbf{q} \in \mathbf{V}_\gamma$ , with  $\mathbf{q} \cdot \mathbf{n}^\Omega|_{\Gamma_N} = 0$ , and all  $v \in U_{\gamma_{in}}$ :*

$$\begin{aligned} \int_{\Omega} \mathbb{K}^{-1} \tilde{\boldsymbol{\sigma}} \cdot \mathbf{q} \, dx - \int_{\Omega} \tilde{u} \nabla \cdot \mathbf{q} \, dx &= - \int_{\Gamma_D} u_D (\mathbf{q} \cdot \mathbf{n}^\Omega) \, ds, \\ \int_{\Omega} \nabla \cdot \tilde{\boldsymbol{\sigma}} v \, dx &= \int_{\Omega} f v \, dx. \end{aligned} \quad (4.6)$$

As a consequence, the MHM-H(div)- $\mathcal{E}_\gamma$  method inherits the positive properties of general stable finite element mixed methods. Moreover, classical tools adopted for mixed methods can be used for stability and error analyses of MHM-H(div)- $\mathcal{E}_\gamma$  solutions. For example, when sufficiently smooth exact solutions in convex regions  $\Omega$  are approximated using Raviart-Thomas space configurations  $\mathcal{E}_\gamma$  for shape regular triangular, tetrahedral or for affine quadrilateral and hexahedral local partitions  $\mathcal{T}^{\Omega_i}$  using uniformly distributed discretization parameters  $\gamma_{sk} = (h_{sk}, k_{sk})$  and  $\gamma_{in} = (h_{in}, k_{in})$ ,  $h_{in} \leq h_{sk}$  and  $k_{in} \geq k_{sk}$ , the following optimal convergence rates

$$\|\boldsymbol{\sigma} - \tilde{\boldsymbol{\sigma}}\|_{\mathbf{L}^2(\Omega)} \lesssim h^{k_{sk}+1} \|\boldsymbol{\sigma}\|_{H^{k_{sk}+1}(\Omega)}, \quad (4.7)$$

$$\|\nabla \cdot (\boldsymbol{\sigma} - \tilde{\boldsymbol{\sigma}})\|_{L^2(\Omega)} \lesssim h_{in}^{k_{in}+1} \|\nabla \cdot \boldsymbol{\sigma}\|_{H^{k_{in}+1}(\Omega)}, \quad (4.8)$$

$$\|u - \tilde{u}\|_{L^2(\Omega)} \lesssim h_{sk}^{k_{sk}+2} \|u\|_{H^{k_{sk}+2}} + h_{in}^{k_{in}+1} \|u\|_{H^{k_{in}+1}(\Omega)}. \quad (4.9)$$

are proven in [DURÁN et al., 2019] for the particular case  $\Gamma_N = \emptyset$ . The flux has the same characteristic accuracy  $O(h_{sk}^{k_{sk}+1})$  of trace approximations in  $\Lambda_\gamma$ , whilst super-convergence  $O(h_{in}^{k_{in}+1})$  holds for the divergence of the flux. Concerning potential error, the two terms on the right hand side may have different influence on the results. Without polynomial degree enrichment  $k_{in} = k_{sk} = k$ , the second term becomes dominant for less refined internal sub-partitions. For instance, when  $h_{sk} = h_{in} = h$  it gives the standard well known convergence rate  $O(h^{k+1})$ , as for the flux variable. However, when  $k_{in} > k_{sk}$ , the influence of second term reduces as compared with the first one, independently of internal mesh refinement, to produce enhanced pressure accuracy of  $O(h_{sk}^{k_{sk}+2})$ .

## 4.5 Examples of hierarchic MHM settings

### Stable two-level finite element settings $\mathcal{E}_\gamma$

Let  $\gamma = (\gamma_{in}, \gamma_{sk})$  be a parameter representing mesh widths and polynomial degrees in two scale levels:  $\gamma_{in} = (h_{in}, k_{in})$  and  $\gamma_{sk} = (h_{sk}, k_{sk})$  at the fine and coarse levels, respectively. That is,  $h_{in} \leq h_{sk}$  and  $k_{in} \geq k_{sk}$ . A procedure for the construction of a consistent two-level finite element setting  $\mathcal{E}_\gamma$  for the MHM-H(div)- $\mathcal{E}_\gamma$  method can be obtained by the following procedures.

1. The mesh hierarchy starts by considering a coarse conformal shape regular partition  $\mathcal{T}$  of  $\Omega$  formed by the conglomeration of sub-partitions  $\mathcal{T}_{h_{sk}}^{\Omega_i} = \{\bar{K}\}$  of the subdomains  $\Omega_i \in \mathcal{T}$ , all of them with characteristic mesh width  $h_{sk}$ .
2. Refined local sub-partitions  $\mathcal{T}_{h_{in}}^{\Omega_i}$  are obtained by the subdivision of  $\mathcal{T}_{h_{sk}}^{\Omega_i}$ . On the skeleton  $\Gamma$  we set a partition  $\mathcal{T}^\Gamma$  by taking facets induced by  $\mathcal{T}_{h_{sk}}$  over  $\Gamma \setminus \partial\Omega$  and induced by  $\mathcal{T}_{h_{in}}^{\Omega_i}$  otherwise.
3. Define local divergence-consistent finite element pairs  $\mathcal{V}_{\gamma_{in}}(\Omega_i) \times \mathcal{U}_{\gamma_{in}}(\Omega_i)$  based in  $\mathcal{T}_{h_{in}}^{\Omega_i}$ . The degree  $k_{in}$  is assumed to be the polynomial degree associated to the normal traces  $\boldsymbol{\tau} \cdot \mathbf{n}^K|_{\partial K}$ ,  $\boldsymbol{\tau} \in \mathbf{V}(K)$ .

Notice that, by construction, mesh consistency and trace consistency are verified, and the resulting two-level finite element setting  $\mathcal{E}_\gamma = \mathbf{V}_\gamma \times U_{\gamma_{in}} \times \Lambda_\gamma$  described in Chapter 4 is well defined and stable. Moreover, the discretization of the flux and potential fields inside the subregions may be enriched to different extents: concerning mesh width  $h_{in} \leq h_{sk}$ , polynomial degree  $k_{in} \geq k_{sk}$ , or both.

## 5 Error estimation

As mentioned before, when working with partial differential equations, we only obtain the exact solution for very simple problems. In practice, we rely on numerical methods that deliver an approximated solution. If the method is convergent, like the finite element methods presented in Chapters 3 and 4, the solution can be as close as needed to the exact solution, but they will never be identical.

One of the tasks of the numerical analyst is to ensure the quality of the result, i.e., if the solution is within the tolerance required by the application. In this context, two questions naturally arise: if the solution is not exact, how large is the error and how can we minimize it?

While knowing the exact approximation error would require one to know the exact solution, algorithms called error estimators have been developed to provide an estimate to the approximation error.

Error estimators are divided into two main classes: *a priori* and *a posteriori*. *A posteriori* estimators are based on the finite element approximation and its input data only, which ensures generality and, thus, renders them adequate for automatic adaptivity processes. In this work, we consider a *a posteriori* error estimator as presented in [VOHRALÍK, 2010] and [AINSWORTH, 2010].

For a pressure approximation  $u_h$ , an *a posteriori* estimation is represented as follows:

$$\|u - u_h\|_{L^2(\Omega)} \leq C \left( \sum_{K \in \mathcal{T}_h} \eta_K^2 \right)^{1/2} \quad (5.1)$$

where  $u$  is the exact solution,  $\eta_K$  is the local error indicator of the element  $K \in \mathcal{T}_h$  and  $C$  is a positive constant independent of the sizes of each element  $K$ .

According to [VOHRALÍK, 2015], an effective estimator should satisfy the following properties:

- i) Guarantee the upper bound described in equation 5.1 is valid and that  $\eta_K$  is computable for every element  $K \in \mathcal{T}_h$ . This property allows for error control and ensures the result is within a desired tolerance.
- ii) Guarantee that in the neighbourhood of  $K$ , denoted  $\mathfrak{T}_K$ ,  $\eta_K$  represents a lower bound of the error  $\|u - u_h\|_{\mathfrak{T}_K}$ , given a constant  $C > 0$  for all  $K \in \mathcal{T}_h$ :

$$\eta_K \leq C \|u - u_h\|_{\mathfrak{T}_K}, \quad \forall K \in \mathcal{T}_h. \quad (5.2)$$

This property allows us to locate regions of the domain where the approximation errors are more prominent, making possible to tweak or improve only the elements of this regions, instead of refining the whole mesh and introducing unneeded degrees of freedoms to be solved.

- iii)** Ensure the estimated error approaches the exact error as the mesh is refined. To evaluate the quality of the estimation we define a parameter called effectivity index,  $I_{eff}$ , that is equal to the ratio between the estimated error and the real error [VOHRALÍK, 2015]:

$$I_{eff} := \frac{\left(\sum_{K \in \mathcal{T}_h} \eta_K^2\right)^{1/2}}{\|u - u_h\|} \quad (5.3)$$

In other words, we want  $I_{eff} \rightarrow 1$  as  $h \rightarrow 0$ . This property is important to avoid overestimating the error. In that case, properties **i** and **ii** could still be satisfied, but the analyst would have little idea whether the result is within desired tolerance or not.

- iv)** Ensure robustness: properties **i**, **ii** e **iii** must be satisfied independently of the problem parameters.
- v)**  $\eta_K$  must be computable locally (for each element separately), with a much lower computational cost in comparison with the calculation of the finite element solution.
- vi)** Identify the most relevant error components to allow for a efficient adaptative refinement process.

## 5.1 Estimates for the flux

Our main goal is the derivation of a posteriori estimates for the MHM-H(div)- $\mathcal{E}_\gamma$  method. Having in mind the equivalence property stated in Theorem 2, the idea is to apply arguments already known in other circumstances of the mixed finite element method. As stated in Theorem 3, the estimates shall be given in terms of weighted norms  $\|\boldsymbol{\tau}\|_{\mathcal{R}, \mathbb{K}^{-1}}^2 := \int_{\mathcal{R}} \mathbb{K}^{-1} \boldsymbol{\tau} \cdot \boldsymbol{\tau} \, d\mathbf{x}$ . The index  $\mathcal{R}$  is omitted when  $\mathcal{R} = \Omega$ .

The a posteriori estimator proposed in [AINSWORTH; MA, 2012], based on the Prager Synge equality, seems appropriate for this purpose. It was designed for the mixed method based on constrained finite element spaces  $\mathbf{V}_{\text{BDM}} \times U_{\text{BDM}}$  of  $hp$ -BDM type for conformal triangular partitions of  $\Omega$ . The estimator is expressed in terms of a *potential reconstruction*  $s \in H^1(\Omega) \cap C(\bar{\Omega})$ , which is obtained from the approximate solution  $(\tilde{\boldsymbol{\sigma}}, \tilde{u})$  given by the mixed finite element method, with  $s|_{\Gamma_D} = u_D$ . Recall that in such methods the approximate potential  $\tilde{u}$  is searched in finite element subspaces in  $L^2(\Omega)$  without any interface continuity constraint, and Dirichlet boundary conditions are weakly enforced. Thus,  $\tilde{u}$  is not a candidate for the role of a potential reconstruction.

The potential reconstruction  $s$  proposed in the [AINSWORTH; MA, 2012] involves post-processing procedures, which hold for problems with continuous piecewise polynomial Dirichlet data  $u_D$  compatible with the potential approximation space.

Our purpose is to adapt these ideas to the mixed method for more general constrained finite element space settings  $\mathbf{V}_\gamma \times U_{\gamma_{in}}$  occurring in the MHM-H(div)- $\mathcal{E}_\gamma$  method applied to problems with general continuous Dirichlet data  $u_D$  and Neumann boundary flux  $\sigma_N \in L^2(\Gamma_N)$ . Under these circumstances, we redefine the potential reconstruction as any function verifying

$$s \in H^1(\Omega) \cap C(\bar{\Omega}); \quad s|_{\Gamma_D} = \mu_D, \quad (5.4)$$

where  $\mu_D \approx u_D$  is a continuous piecewise polynomial approximation of  $u_D$  over the partition  $\mathcal{T}^\Gamma|_{\bar{\Gamma}_D}$ . The following Poincaré inequality (5.5), trace inequality (5.6) on the subregions  $\mathcal{R} = \Omega_i$  forming the partition  $\mathcal{T}$ , with computable constants, and auxiliary solution  $(\bar{\sigma}, \bar{u})$  are required in the proof of the estimated errors.

1. *Poincaré inequality:* There exists a constant  $C_{P,\mathcal{R}} > 0$  such that

$$\|\varphi - \varphi_0\|_{L^2(\mathcal{R})} \leq C_{P,\mathcal{R}} \delta_{\mathcal{R}} \|\nabla \varphi\|_{L^2(\mathcal{R})}, \quad \forall \varphi \in H^1(\mathcal{R}), \quad (5.5)$$

where  $\varphi_0$  is the average of  $\varphi$  in  $\mathcal{R}$  and  $\delta_{\mathcal{R}}$  is the diameter of  $\mathcal{R}$ . This is a result valid for general bounded Lipschitz domains. It is well known that  $C_{P,\mathcal{R}} = \pi^{-1}$  if  $\mathcal{R}$  is convex. Otherwise, the value of  $C_{P,\mathcal{R}}$  may not be so clear. However, if  $\mathcal{R}$  is star-shaped with respect to a ball of radius  $r_{\mathcal{R}}$  then  $C_{P,\mathcal{R}}$  depends only on  $d$  and  $r_{\mathcal{R}}$  [PIETRO; DRONIOU, 2017]. Estimates for  $C_{P,\mathcal{R}}$  can be obtained by numerical algorithms [PAULY; VALDMAN, 2020].

2. *Trace inequality:* There exists a constant  $C_{tr,\mathcal{R}} > 0$  such that

$$\|\varphi\|_{L^2(\partial\mathcal{R})}^2 \leq C_{tr,\mathcal{R}} \left( \frac{d}{\delta_{\mathcal{R}}} \|\varphi\|_{L^2(\mathcal{R})} + 2\|\nabla \varphi\|_{L^2(\mathcal{R})} \right) \|\varphi\|_{L^2(\mathcal{R})}, \quad \forall \varphi \in H^1(\mathcal{R}). \quad (5.6)$$

This inequality is well known for simplices  $T$ , for which  $C_{tr,T}$  depends only on  $d$  and on the aspect ratio  $\frac{\delta_T}{\rho_T}$ ,  $\rho_T$  being the diameter of the larger ball inscribed in  $T$  (in fact,  $C_{tr,T} = \frac{\delta_T}{\rho_T}$  for triangles). Otherwise, the verification of similar results for more general regions usually imposes some constraints on the shape of  $\mathcal{R}$ . As indicated in the book by Di Pietro and Ern [PIETRO; ERN, 2012], Lemma 1.49, the property holds provided  $\mathcal{R}$  is a polytope admitting a matching shape- and contact-regular simplicial sub-partition  $\mathcal{T}^{\mathcal{R}} = \{T\}$ . In such case,

$$C_{tr,\mathcal{R}} = (d+1) \frac{C_{tr,\mathcal{T}^{\mathcal{R}}}}{\varrho_{\mathcal{R}}},$$

where  $C_{tr,\mathcal{T}^{\mathcal{R}}} := \min_{T \in \mathcal{T}^{\mathcal{R}}} C_{tr,T}$ , and  $\varrho_{\mathcal{R}} := \frac{\min_{T \in \mathcal{T}^{\mathcal{R}}} \delta_T}{\delta_{\mathcal{R}}}$ .

*Corollary:* Suppose (5.5) and (5.6) are verified. Then

$$\|\varphi - \varphi_0\|_{L^2(\partial\mathcal{R})}^2 \leq C_{\text{tr},\mathcal{R}} C_{P,\mathcal{R}} \delta_{\mathcal{R}} (dC_{P,\mathcal{R}} + 2) \|\nabla\varphi\|_{L^2(\mathcal{R})}^2, \quad \forall \varphi \in H^1(\mathcal{R}). \quad (5.7)$$

3. Auxiliary functions  $(\bar{\boldsymbol{\sigma}}, \bar{u}) \in H(\text{div}, \Omega) \times L^2(\Omega)$  are defined by the solution of the mixed formulation (3.7)-(3.8) with boundary conditions  $\bar{\boldsymbol{\sigma}} \cdot \mathbf{n}^\Omega = \tilde{\boldsymbol{\sigma}} \cdot \mathbf{n}^\Omega = \Pi_{N,\gamma_{in}} \sigma_N$  on  $\Gamma_N$ ,  $\bar{u}|_{\Gamma_D} = u_D$ , and source term  $\Pi_{\gamma_{in}} f$ . Notice that  $(\bar{\boldsymbol{\sigma}}, \bar{u})$  can also be interpreted as the MHM-H(div)- $\mathcal{E}_\gamma$  approximation of  $(\bar{\boldsymbol{\sigma}}, \bar{u})$ , using the same source and Neumann data. Thus,  $\|\bar{\boldsymbol{\sigma}} - \tilde{\boldsymbol{\sigma}}\|_{\mathbb{K}^{-1}}^2$  can be seen as a discretization error by the method MHM-H(div)- $\mathcal{E}_\gamma$  applied to this auxiliary problem. The following extension of Lemma 1 of [AINSWORTH, 2007] (which was obtained for full homogeneous Dirichlet boundary condition) holds under the current space setting circumstances.

**Lemma 1.** *Let  $(\tilde{\boldsymbol{\sigma}}, \tilde{u}) \in \mathbf{V}_\gamma \times U_{\gamma_{in}}$  be the solution of the mixed formulation (4.6). Then,*

$$\begin{aligned} \|\bar{\boldsymbol{\sigma}} - \tilde{\boldsymbol{\sigma}}\|_{\mathbb{K}^{-1}}^2 &= \min_{\substack{v \in H^1(\Omega) \\ v|_{\Gamma_D} = u_D}} \|\mathbb{K}\nabla v + \tilde{\boldsymbol{\sigma}}\|_{\mathbb{K}^{-1}}^2. \end{aligned}$$

*Proof.* Using the fact that  $\bar{\boldsymbol{\sigma}} - \tilde{\boldsymbol{\sigma}}$  is divergence-free and  $(\bar{\boldsymbol{\sigma}} - \tilde{\boldsymbol{\sigma}}) \cdot \mathbf{n}^\Omega|_{\Gamma_N} = 0$ , we obtain

$$\begin{aligned} \|\bar{\boldsymbol{\sigma}} - \tilde{\boldsymbol{\sigma}}\|_{\mathbb{K}^{-1}}^2 &= \int_{\Omega} \mathbb{K}^{-1}(\bar{\boldsymbol{\sigma}} - \tilde{\boldsymbol{\sigma}}) \cdot (\bar{\boldsymbol{\sigma}} - \tilde{\boldsymbol{\sigma}}) \, d\mathbf{x} \\ &= - \int_{\Omega} \mathbb{K}^{-1} \tilde{\boldsymbol{\sigma}} \cdot (\bar{\boldsymbol{\sigma}} - \tilde{\boldsymbol{\sigma}}) \, d\mathbf{x} - \int_{\Gamma_D} u_D (\bar{\boldsymbol{\sigma}} - \tilde{\boldsymbol{\sigma}}) \cdot \mathbf{n}^\Omega \, ds \\ &= - \int_{\Omega} \mathbb{K}^{-1} \tilde{\boldsymbol{\sigma}} \cdot (\bar{\boldsymbol{\sigma}} - \tilde{\boldsymbol{\sigma}}) \, d\mathbf{x} - \int_{\partial\Omega} v (\bar{\boldsymbol{\sigma}} - \tilde{\boldsymbol{\sigma}}) \cdot \mathbf{n}^\Omega \, ds \\ &= - \int_{\Omega} [\nabla v + \mathbb{K}^{-1} \tilde{\boldsymbol{\sigma}}] \cdot (\bar{\boldsymbol{\sigma}} - \tilde{\boldsymbol{\sigma}}) \, d\mathbf{x} = - \int_{\Omega} \mathbb{K}^{-1} [\mathbb{K}\nabla v + \tilde{\boldsymbol{\sigma}}] \cdot (\bar{\boldsymbol{\sigma}} - \tilde{\boldsymbol{\sigma}}) \, d\mathbf{x}, \end{aligned}$$

for arbitrary  $v \in H^1$ , with  $v|_{\Gamma_D} = u_D$ . By the application of the Cauchy–Schwarz inequality we obtain

$$\begin{aligned} \|\bar{\boldsymbol{\sigma}} - \tilde{\boldsymbol{\sigma}}\|_{\mathbb{K}^{-1}}^2 &\leq \min_{\substack{v \in H^1(\Omega) \\ v|_{\Gamma_D} = u_D}} \|\mathbb{K}\nabla v + \tilde{\boldsymbol{\sigma}}\|_{\mathbb{K}^{-1}}^2, \end{aligned}$$

and equality holds by taking  $v = \bar{u}$ , such that  $-\mathbb{K}\nabla \bar{u} = \bar{\boldsymbol{\sigma}}$ .  $\square$

**Theorem 3.** *Let  $(\tilde{\boldsymbol{\sigma}}, \tilde{u}) \in \mathbf{V}_\gamma \times U_{\gamma_{in}}$  be the solution of the mixed formulation (3.6) corresponding to the MHM-H(div)- $\mathcal{E}_\gamma$  method, for which the aforementioned hypotheses are valid concerning  $u_D$ , Poincaré and trace inequalities on the subregions  $\Omega_i$ . If  $s \in H^1(\Omega) \cap U_{\gamma_{in}}$  is a potential reconstruction, then the upper bound holds:*

$$\|\boldsymbol{\sigma} - \tilde{\boldsymbol{\sigma}}\|_{\mathbb{K}^{-1}}^2 \leq \sum_{\Omega_i} (\eta_{\Omega_i}^{(a)})^2 + (\eta_{\Omega_i}^{(b)})^2, \quad (5.8)$$

for  $\eta_{\Omega_i}^{(a)} = \eta_{P,\Omega_i} + \eta_{D,\Omega_i}$ ,  $\eta_{\Omega_i}^{(b)} = \eta_{R,\Omega_i} + \eta_{N,\Omega_i}$ , where  $\eta_{P,\Omega_i} = \|\mathbb{K}\nabla s + \tilde{\sigma}\|_{\Omega_i, \mathbb{K}^{-1}}$ ,

$$\eta_{D,\Omega_i} := \min_{w \in H_{u_D, \mu_D}^1(\Omega_i)} \|\mathbb{K}\nabla w\|_{\Omega_i, \mathbb{K}^{-1}}, \quad (5.9)$$

$$\eta_{R,\Omega_i} := \frac{\delta_{\Omega_i} C_{P,\Omega_i}}{\sqrt{C_{\mathbb{K},\Omega_i}}} \|f - \Pi_{\gamma_{in}} f\|_{L^2(\Omega_i)}, \quad (5.10)$$

and

$$\eta_{N,\Omega_i} := \frac{[C_{\text{tr},\Omega_i} C_{P,\Omega_i} \delta_{\Omega_i} (dC_{P,\Omega_i} + 2)]^{1/2}}{\sqrt{C_{\mathbb{K},\Omega_i}}} \|\sigma_N - \Pi_{N,\gamma_{in}} \sigma_N\|_{L^2(\partial\Omega_i \cap \Gamma_N)} \quad (5.11)$$

In the above expressions,  $H_{u_D, \mu_D}^1(\Omega_i) = \{w \in H^1(\Omega_i) : w|_{\Gamma_D \cap \Omega_i} = u_D - \mu_D, w|_{\Omega_i \setminus \Gamma_D} = 0\}$ , the constants  $C_{\mathbb{K},\Omega_i}$  correspond to the smallest eigenvalues of  $\mathbb{K}$  on  $\Omega_i$ ,  $C_{P,\Omega_i}$  and  $C_{\text{tr},\Omega_i}$  are the constants of the Poincaré and trace inequalities (5.5)-(5.6) on  $\Omega_i$ .

*Proof.* Closely inspired by Theorem 1 of [AINSWORTH; MA, 2012], the route for the proof has the following main stages.

The terms  $\eta_{\Omega_i}^{(a)}$  and  $\eta_{\Omega_i}^{(b)}$  of the upper bound (5.8) come from estimates of the terms (a) and (b) appearing on the right hand side of the valid Pythagorean identity

$$\|\sigma - \tilde{\sigma}\|_{\mathbb{K}^{-1}}^2 = \|\bar{\sigma} - \tilde{\sigma}\|_{\mathbb{K}^{-1}}^2 + \|\sigma - \bar{\sigma}\|_{\mathbb{K}^{-1}}^2 = (a) + (b), \quad (5.12)$$

where  $(\bar{\sigma}, \bar{u}) \in H(\text{div}, \Omega) \times L^2(\Omega)$  is the aforementioned auxiliary solution. The first component is the discretization error treated in Lemma 1, and second component  $(b) = \|\sigma - \bar{\sigma}\|_{\mathbb{K}^{-1}}^2$  represents the error introduced through data approximation  $f \approx \Pi_{\gamma_{in}} f$  and  $\sigma_N \approx \Pi_{N,\gamma_{in}} \sigma_N$ .

- Estimation of the first term  $(a) = \|\bar{\sigma} - \tilde{\sigma}\|_{\mathbb{K}^{-1}}^2$  in (5.12): Using Lemma 1 and proceeding as in the proof of Theorem 3.3 in [DOLEJŠÍ; ERN; VOHRALÍK, 2016] for a similar estimate, we conclude that

$$\begin{aligned} \|\bar{\sigma} - \tilde{\sigma}\|_{\mathbb{K}^{-1}}^2 &= \min_{\substack{v \in H^1(\Omega) \\ v|_{\Gamma_D} = u_D}} \|\mathbb{K}\nabla v + \tilde{\sigma}\|_{\mathbb{K}^{-1}}^2 \\ &\leq \min_{\substack{v \in H^1(\Omega) \\ v|_{\Gamma_D} = u_D}} \sum_{\Omega_i \in \mathcal{T}} (\|\mathbb{K}\nabla s + \tilde{\sigma}\|_{\Omega_i, \mathbb{K}^{-1}} + \|\mathbb{K}\nabla(v - s)\|_{\Omega_i, \mathbb{K}^{-1}})^2 \\ &\leq \sum_{\Omega_i \in \mathcal{T}} \left( \|\mathbb{K}\nabla s + \tilde{\sigma}\|_{\Omega_i, \mathbb{K}^{-1}} + \min_{w \in H_{u_D, \mu_D}^1(\Omega_i)} \|\mathbb{K}\nabla(w)\|_{\Omega_i, \mathbb{K}^{-1}} \right)^2, \end{aligned}$$

leading to the terms composing  $\eta_{\Omega_i}^{(a)}$ .

- The second term  $(b) = \|\boldsymbol{\sigma} - \bar{\boldsymbol{\sigma}}\|_{\mathbb{K}^{-1}}^2$  in (5.12) may be expressed as,

$$\begin{aligned}
\|\boldsymbol{\sigma} - \bar{\boldsymbol{\sigma}}\|_{\mathbb{K}^{-1}}^2 &= \int_{\Omega} \mathbb{K}^{-1}(\boldsymbol{\sigma} - \bar{\boldsymbol{\sigma}}) \cdot (\boldsymbol{\sigma} - \bar{\boldsymbol{\sigma}}) \, d\mathbf{x} = \int_{\Omega} \nabla(\bar{u} - u) \cdot (\boldsymbol{\sigma} - \bar{\boldsymbol{\sigma}}) \, d\mathbf{x} \\
&= \int_{\Omega} (u - \bar{u}) \nabla \cdot (\boldsymbol{\sigma} - \bar{\boldsymbol{\sigma}}) \, d\mathbf{x} + \int_{\Gamma_N} (\bar{u} - u)(\boldsymbol{\sigma} - \bar{\boldsymbol{\sigma}}) \cdot \mathbf{n}^{\Omega} \, ds \\
&= \sum_{\Omega_i} \int_{\Omega_i} (u - \bar{u})(f - \Pi_{\gamma_{in}} f) \, d\mathbf{x} + \sum_{\Omega_i} \int_{\partial\Omega_i \cap \Gamma_N} (\bar{u} - u)(\sigma_N - \Pi_{\gamma_{in}} \sigma_N) \, ds \\
&= I_1 + I_2.
\end{aligned}$$

The estimations of  $I_1$  and  $I_2$  need some elaboration, using particular properties with respect to the mesh setting associated to  $\mathcal{E}_{\gamma}$ , which are required in Poincaré and trace inequalities. Since  $\int_{\Omega_i} (f - \Pi_{\gamma_{in}} f) \, d\mathbf{x} = 0$ , the application of the Cauchy-Schwartz inequality to  $I_1$  followed by the Poincaré inequality in  $\Omega_i$  gives

$$\begin{aligned}
I_1 &\leq \sum_{\Omega_i} \delta_{\Omega_i} C_{P,\Omega_i} \|\nabla(u - \bar{u})\|_{L^2(\Omega_i)} \|f - \Pi_{\gamma_{in}} f\|_{L^2(\Omega_i)} \\
&\leq \sum_{\Omega_i} \frac{\delta_{\Omega_i} C_{P,\Omega_i}}{\sqrt{C_{\mathbb{K},\Omega_i}}} \|f - \Pi_{\gamma_{in}} f\|_{L^2(\Omega_i)} \|\boldsymbol{\sigma} - \bar{\boldsymbol{\sigma}}\|_{\mathbb{K}^{-1},\Omega_i} = \sum_{\Omega_i} \eta_{R,\Omega_i} \|\boldsymbol{\sigma} - \bar{\boldsymbol{\sigma}}\|_{\mathbb{K}^{-1},\Omega_i}.
\end{aligned}$$

The use of similar arguments combined with the trace inequality (5.7) in  $\Omega_i$  implies

$$\begin{aligned}
I_2 &\leq \sum_{\Omega_i} \frac{[C_{\text{tr},\Omega_i} C_{P,\Omega_i} \delta_{\Omega_i} (dC_{P,\Omega_i} + 2)]^{1/2}}{\sqrt{C_{\mathbb{K},\Omega_i}}} \|\sigma_N - \Pi_{N,\gamma_{in}} \sigma_N\|_{L^2(\partial\Omega_i \cap \Gamma_N)} \|\boldsymbol{\sigma} - \bar{\boldsymbol{\sigma}}\|_{\mathbb{K}^{-1},\Omega_i} \\
&= \sum_{\Omega_i} \eta_{N,\Omega_i} \|\boldsymbol{\sigma} - \bar{\boldsymbol{\sigma}}\|_{\mathbb{K}^{-1},\Omega_i}.
\end{aligned}$$

At the end, for  $\eta_{\Omega_i} = \eta_{R,\Omega_i} + \eta_{N,\Omega_i}$ ,

$$\|\boldsymbol{\sigma} - \bar{\boldsymbol{\sigma}}\|_{\mathbb{K}^{-1}}^2 \leq \left( \sum_{\Omega_i} \eta_{\Omega_i}^2 \right)^{1/2} \left( \sum_{\Omega_i} \|\boldsymbol{\sigma} - \bar{\boldsymbol{\sigma}}\|_{\mathbb{K}^{-1},\Omega_i}^2 \right)^{1/2} = \left( \sum_{\Omega_i} \eta_{\Omega_i}^2 \right) \|\boldsymbol{\sigma} - \bar{\boldsymbol{\sigma}}\|_{\mathbb{K}^{-1}},$$

so that  $\|\boldsymbol{\sigma} - \bar{\boldsymbol{\sigma}}\|_{\mathbb{K}^{-1}}^2 \leq \sum_{\Omega_i} \eta_{\Omega_i}^2$ .

□

## Remarks

1. We emphasize that, excepting  $\eta_{D,\Omega_i}$ , all other quantities  $\eta_{P,\Omega_i}$ ,  $\eta_{N,\Omega_i}$ , and  $\eta_{R,\Omega_i}$  are fully computable in terms of the approximation  $(\tilde{\boldsymbol{\sigma}}, \tilde{u})$ , the data  $f$ ,  $\sigma_N$ , and geometrical information on the subregions.
2. The error components  $\eta_{D,\Omega_i}$  comes from the approximation of the Dirichlet boundary condition  $u_D \approx \mu_D$ , and vanishes for the cases where  $u_D = \mu_D$  is itself is a continuous piecewise polynomial function. Otherwise, the minimization expression for  $\eta_{D,\Omega_i}$  is

not computable, but it is expected to be of higher order whenever  $u_D$  has enough regularity. A bound for this quantity is proposed in Theorem 3.4 of [DOLEJŠÍ; ERN; VOHRALÍK, 2016] for two-dimensional problems with  $\mathbb{K} = \mathbb{I}$ .

3. The residual error component  $\eta_R^2 = \sum_{\Omega_i \in \mathcal{T}} \eta_{R,\Omega_i}^2 = \sum_{\Omega_i \in \mathcal{T}} \frac{C_{P,\Omega_i}^2 \delta_{\Omega_i}^2}{C_{\mathbb{K},\Omega_i}} \|f - \Pi_{\gamma_{in}} f\|_{L^2(\Omega_i)}^2$  is expected to have fast convergence history of rate  $O(h_{in}^{k_{in}+1})$  for sufficiently smooth  $f$ , due to the adopted enriched approximation space  $U_{\gamma_{in}}$ .
4. The role of the error components  $\eta_{N,\Omega_i}$ , which are only applied to subregions  $\Omega_i$  interacting with  $\Gamma_N$ , is to take into account the error induced by the normal boundary enforcement  $\tilde{\boldsymbol{\sigma}} \cdot \mathbf{n}^\Omega|_{\Gamma_N \cap \partial\Omega_i} = \Pi_{N,\gamma_{in}} \sigma_N|_{\Gamma_N \cap \partial\Omega_i}$ . Thus,  $\eta_{N,\Omega_i} = 0$  for  $\Gamma_N = \emptyset$ ,  $\sigma_N = 0$ , or for  $\sigma_N \in \Lambda_\gamma|_{\Gamma_N}$ . Otherwise, recalling that  $\Lambda_\gamma|_{\Gamma_N}$  is formed by piecewise polynomials of degree  $k_{in}$  over the facets  $F \in \mathcal{T}^\Gamma$  included in  $\Gamma_N$ , the normal component  $\eta_N = \left( \sum_{\Omega_i} \eta_{N,\Omega_i}^2 \right)$  is also expected to have fast convergence history of rate  $O(h_{in}^{k_{in}+1})$  for sufficiently smooth  $\sigma_N$ .

## 5.2 Potential reconstruction

To apply Theorem 3 as a viable tool for efficient error control of numerical simulations by the MHM-H(div)- $\mathcal{E}_\gamma$  method, an efficient reconstructed potential  $s$  is required. Our goal is to extend the methodology proposed in [AINSWORTH; MA, 2012] to more general constrained finite element space settings adopted in the MHM-H(div)- $\mathcal{E}_\gamma$  method for two-dimensional problems. Recall that the mixed method in [AINSWORTH; MA, 2012] is for  $hp$  finite element spaces based on conformal triangular partitions. The proposed potential reconstruction has three stages: (1) solution  $\hat{u}^o$  of independent local  $H^1$ -conforming Neumann problems over each element, (2) inter-element smoothing of the resulting potential  $\hat{u}^o$  by an averaging procedure to get a piecewise continuous trace function  $\mu$  over  $\Gamma$ , and (3) solution of independent local  $H^1$ -conforming Dirichlet problems over each element using  $\mu$  as Dirichlet data.

Since the polynomial degree of a BDM potential space  $U_{\text{BDM}}$  is one unit less than the degree of the corresponding flux space  $\mathbf{V}_{\text{BDM}}$ , the first stage is used to equilibrate the polynomial degrees in both fields. Notice that such first post-processing stage is not necessary for our current  $\mathbf{V}_\gamma \times U_{\gamma_{in}}$  finite element context, for the potential approximation  $\tilde{u} \in U_{\gamma_{in}}$  is already sufficiently accurate with respect to  $\tilde{\boldsymbol{\sigma}} \in \mathbf{V}_\gamma$ . Moreover, the third stage is a standard procedure once the piecewise continuous trace function  $\mu$  over  $\Gamma$  is available. Concerning inter-element smoothing procedure for the construction of  $\mu$ , the original version in [AINSWORTH; MA, 2012] refers to a triangular conformal partition  $\mathcal{T}$  without any refined sub-partitions inside to be matched over interfaces.

Instead, for the definition of the inter-element smoothing procedure under the more general circumstances of the MHM-H(div)- $\mathcal{E}_\gamma$  method, we assume that the internal partitions  $\mathcal{T}^{\Omega_i}$  and  $\mathcal{T}^{\Omega_j}$  are conformal over interfaces  $\Gamma_{i,j} = \partial\Omega_i \cap \partial\Omega_j$  between neighboring subdomains  $\Omega_i$  and  $\Omega_j$ . Under this hypothesis, the skeleton partition  $\mathcal{T}^\Gamma$  admits a refined partition  $\mathcal{T}_+^\Gamma$  controlling the contact of elements  $K_i \in \mathcal{T}_{h_{in}}^{\Omega_i}$  and  $K_j \in \mathcal{T}_{h_{in}}^{\Omega_j}$  at interfaces  $F_{i,j} = K_i \cap K_j$ , in the sense that  $F_{i,j} \in \mathcal{T}_+^\Gamma$ . Moreover, for simplicity purpose, we assume uniform polynomial degree distribution  $k_{in}$  over the subregions and within the local partitions  $\mathcal{T}_{h_{in}}^{\Omega_i}$ . Then, a trace space  $\Lambda_{\gamma_{in}}^c$  is defined over  $\mathcal{T}_+^\Gamma$  by continuous piecewise polynomials of degree distribution  $k_{in}$ . For instance, these properties are verified by the example of two-level setting shown in Fig. 19.

In summary, under these hypotheses, and given an approximate solution  $(\tilde{\sigma}, \tilde{u}) \in \mathbf{V}_\gamma \times U_{\gamma_{in}}$  by the MHM-H(div)- $\mathcal{E}_\gamma$  method, an associated potential reconstruction  $s \in H^1(\Omega)$  is the result of the following two stages: inter-element smoothing procedure to get a piecewise continuous trace function  $\mu \in \Lambda_{\gamma_{in}}^c$  and solving local Dirichlet problems in the subdomains  $\Omega_i$  using  $\mu$  as Dirichlet data over  $\partial\Omega_i$ .

### 5.2.1 Inter-element smoothing procedure

Firstly, set  $\mu|_{\Gamma_D} = \mathcal{I}_{D,\gamma_{in}} u_D \in \Lambda_{\gamma_{in}}^c|_{\Gamma_D}$  by a trace interpolant  $\mathcal{I}_{D,\gamma_{in}} : C(\Gamma_D) \rightarrow \Lambda_{\gamma_{in}}^c|_{\Gamma_D}$ . Elsewhere, the purpose is to construct a function  $\mu \in \Lambda_{\gamma_{in}}^c$  from the approximate potential  $\tilde{u}$ .

The inter-element smoothing procedure for 3D approximations occurs in three steps: weighted averaging of the potential over faces, weighted averaging of the face values over ribs and weighted averaging of the rib values at nodes.

The averaged solution values over the faces and ribs are represented by 2d and 1d discontinuous elements of appropriate polynomial order. To this end, the ease of generating elements spaces of any dimension in the NeoPZ library is very useful.

1. Weighted average over interfaces : for  $F_{i,j} = \partial K^i \cap \partial K^j \in \mathcal{T}_+^\Gamma$  not included in  $\Gamma_D$  set  $\mu|_{F_{i,j}} \in \Lambda_{\gamma_{in}}^c|_{F_{i,j}}$  such that

$$\int_{F_{i,j}} \left[ \frac{\omega(\mathbb{K}, K^i) \tilde{u}|_{K^i} + \omega(\mathbb{K}, K^j) \tilde{u}|_{K^j}}{\omega(\mathbb{K}, K^i) + \omega(\mathbb{K}, K^j)} - \mu|_{F_{i,j}} \right] v ds = 0, \quad \forall v \in \Lambda_{\gamma_{in}}^c|_{F_{i,j}}.$$

where  $\omega(\mathbb{K}, K^r)$  is the largest eigenvalue of  $\mathbb{K}$  restricted to  $K^r$ .

2. Average over edges: for an edge  $e$  not included in  $\Gamma_D$  set the patch  $\mathcal{T}(e)$  formed by all the interfaces  $F_{i,j} = \partial K^i \cap \partial K^j \in \mathcal{T}_+^\Gamma$  having  $e$  as one their edges. Then, associate with  $\mu|_{F_{i,j}}$  a weight  $\omega(F_{i,j}) = \max \{ \omega(\mathbb{K}, K^i), \omega(\mathbb{K}, K^j) \}$ , and update  $\mu|_e \in \Lambda_{\gamma_{in}}^c|_e$  by fitting

$$\int_e \left[ \frac{\sum_{F_{i,j} \in \mathcal{T}(e)} \mu|_{F_{i,j}} \omega(F_{i,j})}{\sum_{F_{i,j} \in \mathcal{T}(e)} \omega(F_{i,j})} - \mu|_e \right] v ds, \quad \forall v \in \Lambda_{\gamma_{in}}^c|_e.$$

3. Average over vertexes: for a vertex  $\mathbf{a}$  of the partition  $\mathcal{T}_+^\Gamma$  not included in  $\Gamma_D$ , set the patch  $\mathcal{T}(\mathbf{a})$  of edges  $e$  of elements in  $\mathcal{T}_+^\Gamma$  having  $\mathbf{a}$  as one of their vertices. Then, associate with  $\mu|_e(\mathbf{a})$  a weight  $\omega(e) = \max_{F \in \mathcal{T}(e)} \{\omega(F)\}$ , and update the value  $\mu(\mathbf{a})$  by the average

$$\mu(\mathbf{a}) \leftarrow \frac{\sum_{e \in \mathcal{T}(\mathbf{a})} \mu|_e(\mathbf{a}) \omega(e)}{\sum_{e \in \mathcal{T}(\mathbf{a})} \omega(e)}.$$

Finally, update  $\mu|_{F_{i,j}}(\mathbf{x}) \leftarrow \mu_{\mathbf{a}}(\mathbf{x}) + \mu_e(\mathbf{x}) + \mu_{F_{i,j}}(\mathbf{x})$ , represented in terms of hierarchical vertex, edge and internal shape functions associated with  $F_{i,j}$ , by usual operations used in the assembly algorithms for  $hp$   $H^1$ -conforming finite element spaces [CALLE; DEVLOO; GOMES, 2015]. This is done in a sequence of steps, starting with vertexes, then throughout edges and the face  $F_{i,j}$  itself. The vertex component  $\mu_{\mathbf{a}}(\mathbf{x})$  is computed by first order Lagrange interpolation of the new values  $\mu(\mathbf{a})$  of Step 3 at the vertexes of  $F_{i,j}$ . Next, by incorporating the vertex term, the edge component  $\mu_e(\mathbf{x})$ , vanishing on the vertexes, is obtained by updating the edge averages of Step 2. Finally, by incorporating the vertex and edge terms, get the internal component  $\mu_{F_{i,j}}(\mathbf{x})$ , vanishing on  $\partial F_{i,j}$ , by updating the face average of Step 1. Plots illustrating average over edges and vertex updating are given in Figures 21 and 22.

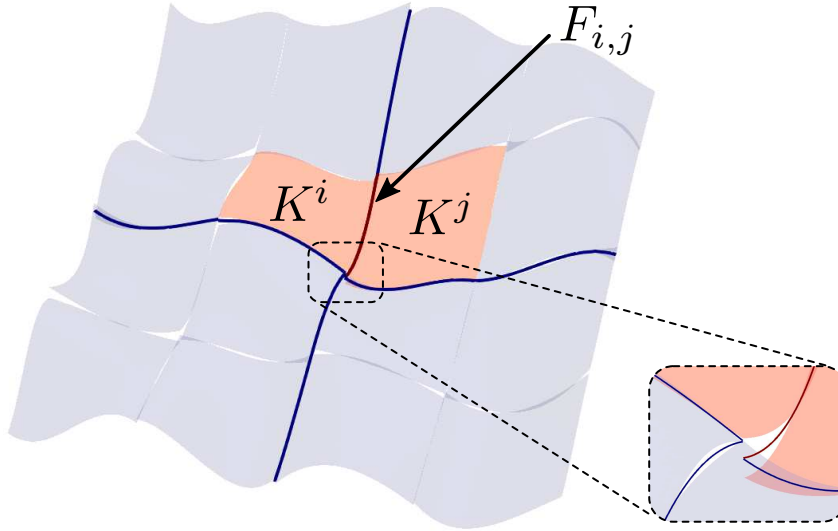


Figure 21 – Illustration of the inter-element smoothing procedure: average over edges.

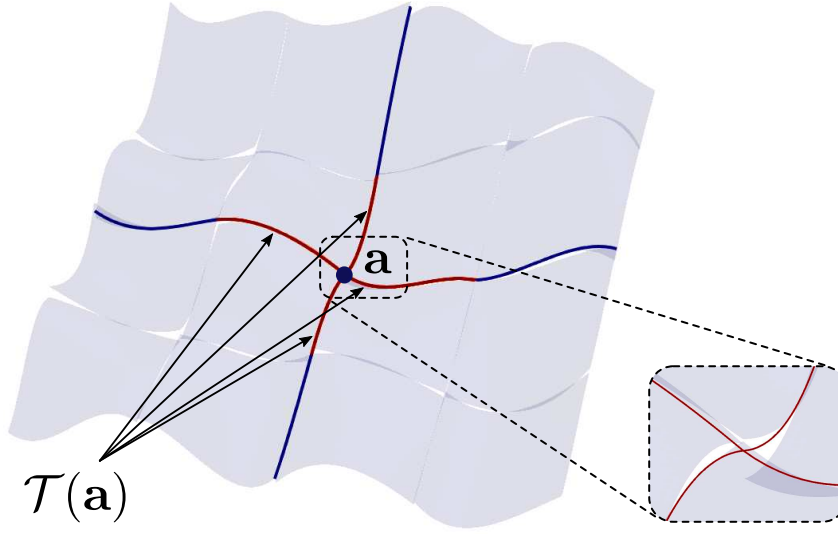


Figure 22 – Illustration of the inter-element smoothing procedure: update vertex values.

The inter-element smoothing procedure for two-dimensional problems requires some adjustments: we perform the average in Step 1 over edges  $e_{i,j} = K_i \cap K_j$  (instead of interfaces) and go straightforward to node update in Step 3, and the final smoothed trace has the form  $\mu|_{e_{i,j}}(\mathbf{x}) = \mu_{\mathbf{a}}(\mathbf{x}) + \mu_e(\mathbf{x})$ .

### 5.2.2 Solving local Dirichlet problems

Let  $\mu \in \Lambda_{\gamma_{in}}^c$  be given by the inter-element smoothing procedure, and set  $\tilde{\sigma}_i := \tilde{\sigma}|_{\Omega_i}$ . The reconstructed potential  $s \in H^1(\Omega)$  is defined as  $s|_{\Omega_i} = s_i$ , where the functions  $s_i$  are obtained by solving  $H^1$ -conforming Galerkin finite element formulations of local problems in  $\Omega_i$ . The solvers are for finite element spaces  $U_{\gamma_{in}}^c(\Omega_i) \subset H^1(\Omega_i) \cap U_{\gamma_{in}}(\Omega_i)$  and for  $\mu|_{\partial\Omega_i}$  as Dirichlet boundary data on  $\partial\Omega_i$ . Namely,  $s_i \in U_{\gamma_{in}}^c(\Omega_i)$  verifies  $s_i|_{\partial\Omega_i} = \mu|_{\partial\Omega_i}$  and

$$(\mathbb{K}\nabla s_i, \nabla w)_{\Omega_i} = -(\tilde{\sigma}_i, \nabla w)_{\Omega_i}, \quad \forall w \in U_{\gamma_{in}}^c(\Omega_i) \cap H_0^1(\Omega_i).$$

By the constraints  $s_i = \mu$  on  $\partial\Omega_i$  the continuity of  $s$  over interfaces is satisfied (i.e.  $s \in H^1(\Omega)$ ). Moreover, since by definition  $\mu|_{\Gamma_D} = \tilde{u}$ , we conclude that  $s$  is indeed a potential reconstruction for the MHM-H(div)- $\mathcal{E}_\gamma$  method.

An illustration is shown Figure 23 for a two-dimensional setting. An oscillatory problem is solved by the MHM-H(div)- $\mathcal{E}_\gamma$  method based on a coarse partition by  $2 \times 2$  square subregions, using parameter discretizations  $h_{in} = h_{sk}/2$ ,  $k_{sk} = 1$  and  $k_{in} = 3$ . The exact potential  $u$  and its discontinuous approximation  $\tilde{u}$  are shown in Figure 23 (a) and (b). The potential reconstruction  $s \in H^1(\Omega)$  shown in Figure 23 (c) is the result of the final stage, by solving local Dirichlet problems.

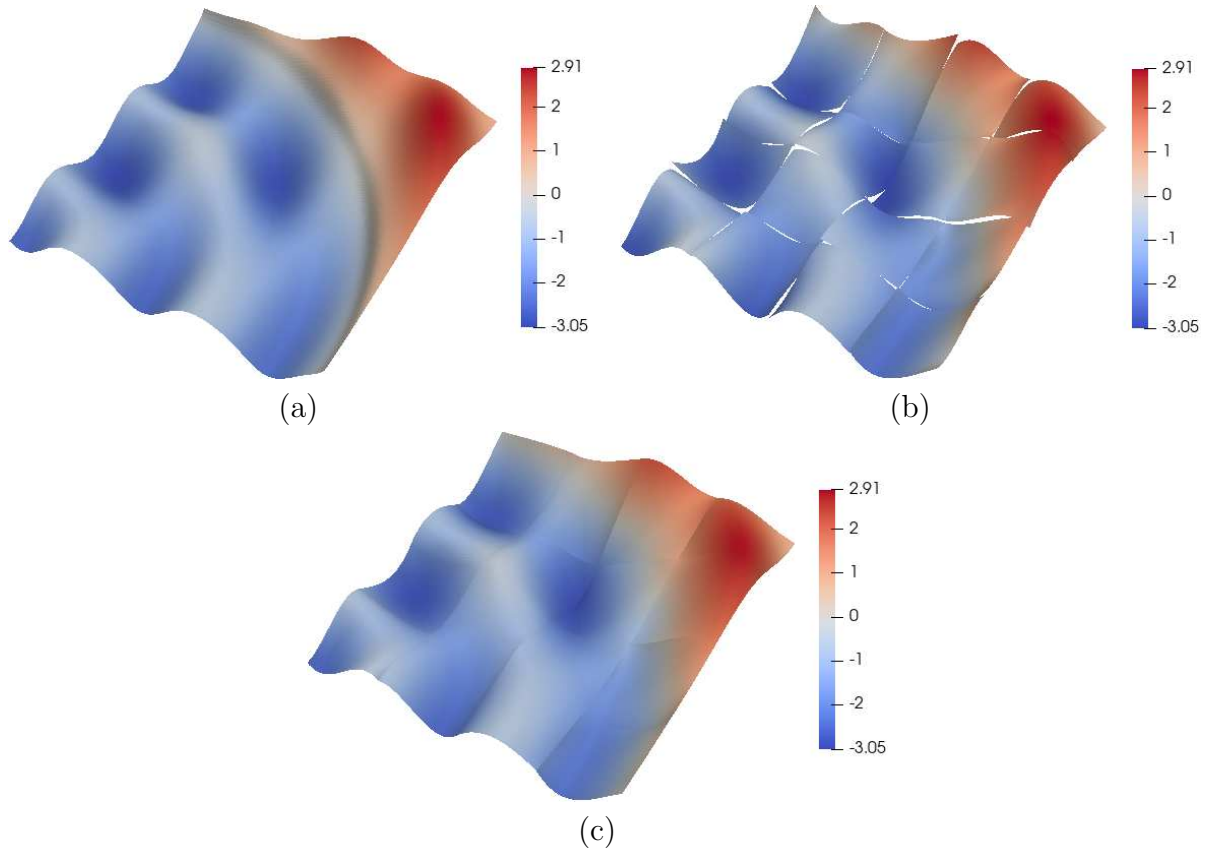


Figure 23 – Illustration of the potential reconstruction: (a) exact potential  $u$ , (b) MHM-H(div)- $\mathcal{E}_\gamma$  solution  $\tilde{u}$ , and (c) potential reconstruction  $s \in H^1(\Omega)$ .

## 5.3 Adaptivity

### 5.3.1 Stable $h$ -adaptive finite element settings $\mathcal{E}_\gamma$

The goal of any adaptive algorithm is to develop a way to check and improve the quality of the approximation. Based on the proposed a posteriori error estimator of Theorem 3, we propose a trace  $h$ -adaptive algorithm to guide a proper choice of the trace space. For comparison, we also define a classic  $h$ -adaptive strategy for subregion refinement. Recall that the estimator in Theorem 3 is composed of local estimated error indicators  $\eta_{\Omega_i}^{(a)} = \eta_{P,\Omega_i} + \eta_{D,\Omega_i}$ ,  $\eta_{\Omega_i}^{(b)} = \eta_{R,\Omega_i} + \eta_{N,\Omega_i}$ . In both examples, it is expected that the error indicators  $\eta_{D,\Omega_i}$ ,  $\eta_{R,\Omega_i}$  and  $\eta_{N,\Omega_i}$  are insignificant with respect to  $\eta_{P,\Omega_i}$ . Thus, they are not considered in the refinement process, and only the magnitude of  $\eta_{P,\Omega_i}$  is used in the decision to mark  $\Omega_i$  as candidate to be refined or to have the skeleton partition of its facets to be refined.

### 5.3.2 Trace $h$ -adaptivity

For the MHM-H(div)- $\mathcal{E}_\gamma$  formulation with internal mesh refinement, the normal fluxes coming from the finest scale inside the subregions are restricted to the coarse-scale trace space. The following  $h$ -adaptive process for the finite element space setting  $\mathcal{E}_\gamma$  based

on successive refinements of the skeleton partition  $\mathcal{T}^\Gamma$  is proposed. The estimator of Theorem 3 is used to indicate the distribution of the errors associated with the subregions. The skeleton partitions associated with selected subregions will be refined up to a level associated with the subregion.

Assume the shape-regular coarse partition  $\mathcal{T} = \{\Omega_i\}$  of  $\Omega$  is subjected to  $\text{ref}_{max}$  uniform refinement steps to give a conformal reference partition  $\mathcal{T}_{\text{ref}} = \{K\}$  by micro-elements  $K$  of characteristic mesh with  $h_{in}$ . These micro-elements are conglomerated to form sub-partitions  $\mathcal{T}^{\Omega_i}$ . This is a case where the partitions  $\mathcal{T}^{\Omega_i}$  and  $\mathcal{T}^{\Omega_j}$  of neighboring subdomains  $\Omega_i$  and  $\Omega_j$  are conformal over interfaces  $\Gamma_{i,j} = \partial\Omega_i \cap \partial\Omega_j$ . Fixed polynomial degrees  $k_{sk}$  and  $k_{in}$ ,  $k_{sk} \leq k_{in}$ , are applied to skeleton and subregion partitions, respectively.

The estimated errors are used to choose a consistent skeleton partition  $\mathcal{T}^\Gamma$  adapted to the approximation. Throughout the adaptivity process, the hierarchy of finite element space settings  $\mathcal{E}_\gamma$  are associated with discretization parameters  $\gamma = (\gamma_{in}, \gamma_{sk})$  of the form  $\gamma_{in} = (h_{in}, k_{in})$  and  $\gamma_{sk} = (\mathbf{h}_{sk}, k_{sk})$ , where  $\mathbf{h}_{sk}$  represents the non-uniform mesh size distribution of elements in  $\mathcal{T}^\Gamma$ . During the trace  $h$ -adaptive process  $\mathbf{h}_{sk}$  evolves, and therefore  $\gamma$  changes accordingly as well.

Starting from the coarsest skeleton partition,  $\mathcal{T}^\Gamma$  formed by the facets  $F$  of the subdomains  $\Omega_i$ , and with internal partition  $\mathcal{T}^{\Omega_i}$  defined by  $\text{ref}_{max}$ , the proposed adaptive Algorithm 1 is based on successive refinement loops of the skeleton partition. In each adaptive instance, a refinement level  $\text{ref}_{\Omega_i}$  is associated with each macro partition  $\Omega_i$ . Then,  $\text{ref}_{\Omega_i}$  is used to redefine the mesh width  $\mathbf{h}_{sk}$  of the skeleton partition.

In summary, given the error indicator of the current approximate solution, the adaptive procedures are summarized in Algorithm 1. Examples are shown in Section 6.3.2.

---

**Algorithm 1** Trace  $h$ -adaptivity

---

Input initial partitions  $\mathcal{T} = \{\Omega_i\}$  and  $\mathcal{T}^\Gamma$ , discretization parameter  $\gamma = (\gamma_{in}, \gamma_{sk})$ , finite element space setting  $\mathcal{E}_\gamma$ , threshold  $\epsilon \in (0, 1)$ , target global estimated error  $\eta_{goal}$ , maximum number of iterations  $maxiter$ , and set  $n_{\Omega_j} = 0$ . While  $\eta > \eta_{goal}$  or  $iter < maxiter$ :

1. Solve the problem using MHM-H(div)- $\mathcal{E}_\gamma$  method.
  2. Compute the error indicator  $\eta_{P,\Omega_i}$  associated to the subregions  $\Omega_i$ .
  3. Define  $\eta_{max} = \max_{\Omega_i} \{\eta_{P,\Omega_i} | \text{ref}_{\Omega_i} < \text{ref}_{max}\}$ .
  4. If  $\eta_{P,\Omega_i} > \epsilon \cdot \eta_{max}$  and  $\text{ref}_{\Omega_i} < \text{ref}_{max}$ , increment  $\text{ref}_{\Omega_i}$ .
  5. Refine  $\mathcal{T}^\Gamma$ , such that the refinement level of the skeleton  $F_{i,j} = \partial\Omega_i \cap \partial\Omega_j$  is equal to  $\max(\text{ref}_{\Omega_i}, \text{ref}_{\Omega_j})$ . Update  $\mathbf{h}_{sk}$  (and  $\gamma$  as well).
  6. Using the updated trace space  $\Lambda_\gamma$ , update the flux space  $\mathbf{V}_\gamma$  constrained to it, and proceed to a new iteration.
-

### 5.3.3 Classic $h$ -adaptivity

For comparison with respect to the trace adaptivity Algorithm 1, we also consider a classic  $h$ -adaptive algorithm for the mixed method, where a hierarchy of adaptive configurations  $\mathcal{E}_\gamma$  for adapted partitions  $\mathcal{T} = \{\Omega_i\}$  are defined. We restrict the case to subregions  $\Omega_i$  of usual element geometry, without internal sub-partitions, i.e.,  $\mathcal{T}^{\Omega_i} = \Omega_i$  (each macro domain is a single element). They are supposed to be the conglomeration of micro-elements of a refined conformal reference partition  $\mathcal{T}_{ref}$ . This way, the elements obtained from the refinement of  $\Omega_i$  are also supposed to share this property. Consequently, consistent skeleton meshes  $\mathcal{T}^\Gamma$  and  $\mathcal{T}_+^\Gamma$  are feasible. An example is illustrated by numerical simulations in Section 6.3.1.

At each step of  $h$ -adaptivity,  $\mathcal{E}_\gamma$  is a multilevel finite element setting in the sense that  $\gamma = (\gamma_{in}, \gamma_{sk})$  has the form  $\gamma_{in} = (\mathbf{h}_{in}, k_{in})$  and  $\gamma_{sk} = (\mathbf{h}_{sk}, k_{sk})$ , where  $\mathbf{h}_{in}$  and  $\mathbf{h}_{sk}$  are vectors representing the non-uniform mesh size distributions over the adaptive partitions  $\mathcal{T}$  and  $\mathcal{T}^\Gamma$ . Both polynomial degrees  $k_{in}$  and  $k_{sk}$ ,  $k_{sk} < k_{in}$ , are assumed to have uniform distribution over  $\mathcal{T}$  and  $\mathcal{T}^\Gamma$ .

At each instance of the  $h$ -adaptive process, given the MHM-H(div)- $\mathcal{E}_\gamma$  approximation, we apply the estimator of Theorem 3 to compute the distribution of errors over the subregions. The computed error distribution is used to mark the subdomains to be refined. The domain partition  $\mathcal{T}$  evolves by the substitution of a subdomain in the current partition by new ones obtained after refinement. Accordingly, the skeleton  $\Gamma$  and skeleton partition  $\mathcal{T}^\Gamma$  evolve as well. Based on the new mesh setting, new trace spaces  $\Lambda^\Gamma$  and local divergence-consistent finite element pairs  $\mathcal{V}_\gamma(\Omega_i) \times \mathcal{U}_{\gamma_{in}}(\Omega_i)$  are created to form a new finite element setting  $\mathcal{E}_\gamma$ .

The successive  $h$ -refinement loops are summarized in Algorithm 2.

---

#### Algorithm 2 Subregion $h$ -adaptivity

---

Input initial partitions  $\mathcal{T} = \{\Omega_i\}$  and  $\mathcal{T}^\Gamma$ , discretization parameter  $\gamma = (\gamma_{in}, \gamma_{sk})$ , finite element space setting  $\mathcal{E}_\gamma$ , threshold  $\epsilon \in (0, 1)$ , target global estimated error  $\eta_{goal}$ , and maximum number of iterations  $maxiter$ . While  $\eta > \eta_{goal}$  or  $iter > maxiter$ :

1. Solve the problem using MHM-H(div)- $\mathcal{E}_\gamma$  method.
  2. Compute the error indicator  $\eta_{P,\Omega_i}$  associated with each subregions  $\Omega_i$ .
  3. Define  $\eta_{max} = \max_{\Omega_i} \{\eta_{P,\Omega_i}\}$
  4. If  $\eta_{P,\Omega_i} > \epsilon \cdot \eta_{max}$ , mark  $\Omega_i$  to be refined.
  5. Refine  $\mathcal{T}$  and create  $\mathcal{T}^\Gamma$  keeping mesh consistency, and update  $\mathbf{h}_{in}$ ,  $\mathbf{h}_{sk}$ , and  $\gamma$ , accordingly.
  6. Create a new finite element space setting  $\mathcal{E}_\gamma$  and proceed to a new iteration.
-

## 6 Numerical results

This section is dedicated to present and discuss some verification tests for a posteriori error estimation based on MHM- $H(\text{div})$ - $\mathcal{E}_\gamma$  formulation analyzed in the previous sections.

In the presented tests, the macro partitions  $\mathcal{T} = \{\Omega_i\}$ , as well as the internal sub-partitions  $\mathcal{T}^{\Omega_i}$ , are formed by uniform quadrilaterals. The boundary conditions are of pure Dirichlet type ( $\Gamma_N = \emptyset$ ) or else of combined Dirichlet and vanishing Neumann type ( $\sigma_N = 0$ ). Thus,  $\eta_{N,\Omega_i} = 0$  in all the cases, and trace constants  $C_{\text{tr},\Omega_i}$  are not required. Notice that the Poincaré constant for the convex quadrilateral subregions is  $C_{P,\Omega_i} = \frac{1}{\pi}$ .

The quality of the error estimators shall be measured by comparing known exact errors  $E_{\text{ex}} = \|\boldsymbol{\sigma} - \tilde{\boldsymbol{\sigma}}\|_{\mathbb{K}^{-1}}$  and estimated errors  $E_{\text{est}}$ . Global and local effectivity indexes are also computed:

$$I_{\text{eff}} = \frac{E_{\text{est}}}{E_{\text{ex}}}, \quad I_{\text{eff}}(\Omega_i) = \frac{E_{\text{est}}(\Omega_i)}{E_{\text{ex}}(\Omega_i)}.$$

All tests are implemented in C++ using the framework *NeoPZ*, which is an object oriented environment for the development finite element simulations, where tools for the construction of the required constrained  $H(\text{div})$ -conforming spaces are available (e.g., a hierarchy of shape functions of high degree for a variety of element geometry, data structure allowing the identification of facet and internal shape functions of different degrees, and procedures for shape function constraints).

### 6.1 Tests with two-level finite element space settings $\mathcal{E}_\gamma$

Two test problems with know exact solutions are solved by the MHM- $H(\text{div})$ - $\mathcal{E}_\gamma$  method using two-level finite element space settings described in Section 4.5: one with smooth solution for constant permeability and the second one with an inner point singularity and piecewise constant permeability.

#### 6.1.1 Problem with smooth solution

Let us start with the test problem for unit constant permeability (i.e.,  $\mathbb{K} = \mathbb{I}$  is the  $2 \times 2$  identity matrix) having the smooth exact solution  $u(x, y) = \sin\pi x \cos\pi y$  (Figure 25 (a)) verifying the full homogeneous Dirichlet boundary condition  $u_D = 0$  on  $\partial\Omega$ . Thus, the estimated errors are given by

$$E_{\text{est}} = \left( \sum_{\Omega_i \in \mathcal{T}_{h_{sk}}} \left( \eta_{P,\Omega_i}^2 + \eta_{R,\Omega_i}^2 \right) \right)^{1/2}.$$

## 6.1.1.1 Effect of the shape of the macro domain

We start by testing the robustness of  $E_{\text{est}}$  using two different kinds of sub-region geometry.

Firstly, we take  $4 \times 4$  square subregions with refined sub-partitions  $\mathcal{T}^{\Omega_i}$  obtained by a single uniform subdivision, as illustrated in Figure 25 (a). The second case is for L-shaped (non-convex) subregions, each composed of 3 quadrilateral elements (Figure 25 (b)). The skeleton partition  $\mathcal{T}^\Gamma$  is formed by the edges of the subregions. Thus,  $h_{sk} = 1/4$  and  $h_{in} = 1/8$  in both cases. For these geometric partitions, the space configurations  $\mathcal{E}_\gamma$  are for polynomial degree  $k_{sk} = 1$  over the skeleton partition and for finite element local subspaces  $\mathcal{V}_\gamma(\Omega_i) \times \mathcal{U}_{\gamma_{in}}(\Omega_i)$ , with  $k_{in} = 3$ .

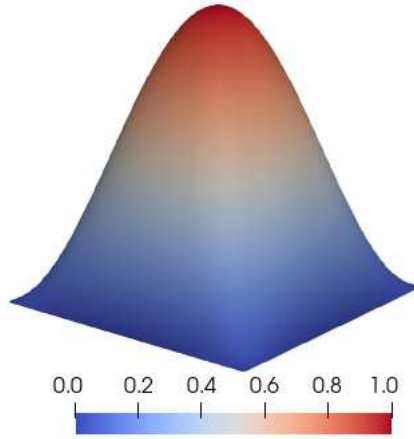


Figure 24 – Exact solution  $u(x, y)$  of the smooth problem.

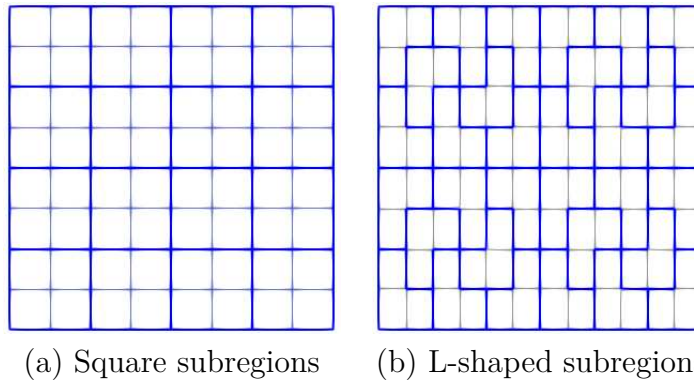


Figure 25 – Smooth solution problem: (a) square subregions and L-shaped subregions (b).

The results are presented in Figure 27 for the local exact errors  $E_{\text{ex}}(\Omega_i)$ , estimated errors  $\eta_{P, \Omega_i}$ , and local effectivity indexes  $I_{\text{eff}}(\Omega_i)$  over the subdomains. The global effectivity index is  $I_{\text{eff}} = 1.059$  for the square mesh setting, whilst  $I_{\text{eff}} = 1.09$  for the L-shaped case, indicating that the effect of geometry shape is not significant for the estimator efficiency.

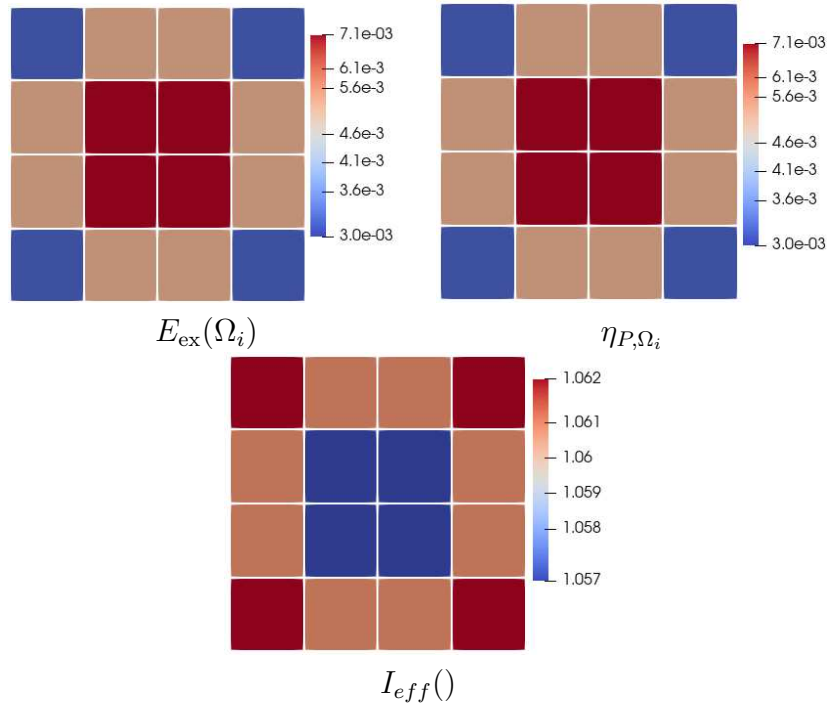


Figure 26 – Smooth solution approximated by the MHM-H(div)- $\mathcal{E}_\gamma$  method with square subregion geometry: exact errors  $E_{\text{ex}}(\Omega_i)$ , estimated errors  $\eta_{P,\Omega_i}$ , and local effectivity indexes  $I_{\text{eff}}(\Omega_i)$  in the subregions, for space configuration with  $h_{sk} = 1/4$ ,  $h_{in} = 1/8$ ,  $k_{sk} = 1$  and  $k_{in} = 3$ .

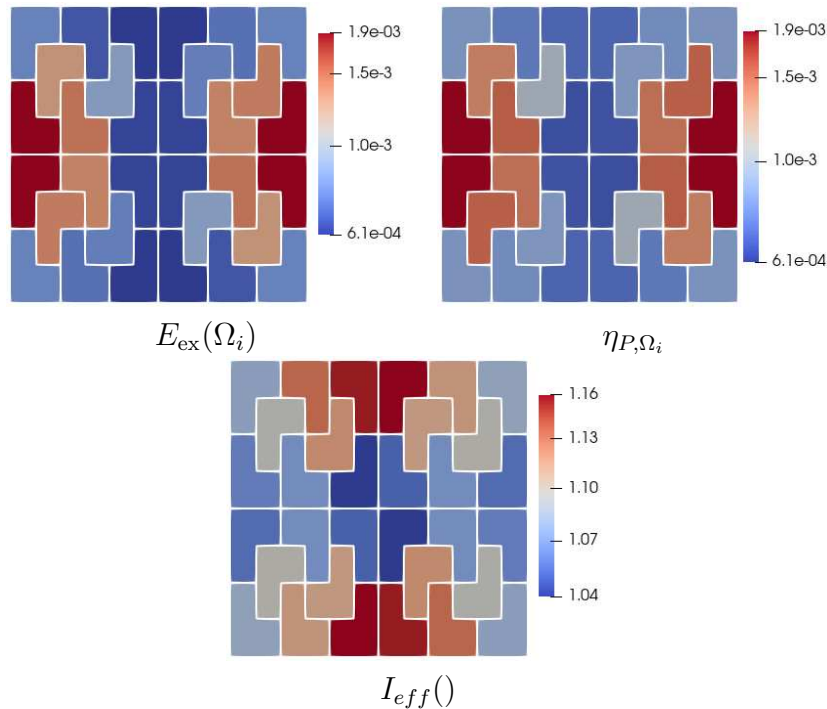


Figure 27 – Smooth solution approximated by the MHM-H(div)- $\mathcal{E}_\gamma$  method with L-shaped subregion geometry: exact errors  $E_{\text{ex}}(\Omega_i)$ , estimated errors  $\eta_{P,\Omega_i}$ , and local effectivity indexes  $I_{\text{eff}}(\Omega_i)$  in the subregions, for space configuration with  $h_{sk} = 1/4$ ,  $h_{in} = 1/8$ ,  $k_{sk} = 1$  and  $k_{in} = 3$ .

## 6.1.1.2 Effect of internal refinement

Next, we present convergence histories of flux approximations by the MHM-H(div)- $\mathcal{E}_\gamma$  method on a sequence of uniform square subregions for  $h_{sk} = 2^{-j}$ ,  $j = 2, \dots, 6$ , and internal uniform squared partitions with  $h_{in} = h_{sk}/2^l$ ,  $l = 0, 1$  and  $2$ . We take polynomial degrees  $k_{sk} = 1, 2$ , and  $3$ ,  $k_{in} = k_{sk} + i$ , with  $i = 1$  and  $2$ . Notice that in these cases the internal partitions  $\mathcal{T}_{h_{in}}^{\Omega_i}$  match over the skeleton  $\Gamma$ , so mesh and space consistency properties hold. Moreover, the hypotheses made for the well definition of inter-element smoothing procedure are clearly verified. An example of this two-scale finite element setting is shown in Fig. 19.

The results for the exact errors  $E_{ex}$ , estimated errors  $\eta_P$ , residual errors  $\eta_R$ , and effectivity indexes  $I_{eff}$  are summarized in Table 1, and graphical illustrations of these results are plotted in Figure 28. The rates of flux convergence of order  $O(h_{sk}^{k_{sk}+1})$  predicted by the a priori analysis are verified, a behavior closely followed by the estimated error term  $\eta_P$ . Concerning the residual term  $\eta_R$ , the convergence rate  $O(h_{in}^{k_{in}+1})$  is observed, verifying the typical error estimate of the  $L^2$ -projection of this smooth source term  $f$  over the potential finite element space  $U_{\gamma_{in}}$ .

Moreover, as compared with  $\eta_P$  in refined settings,  $\eta_R$  is several orders of magnitude smaller and can be neglected for practical purposes. We observe that the effective index  $I_{eff}$  is greatly improved by the refinement of the internal partitions  $\mathcal{T}_{h_{in}}^{\Omega_i}$ . For instance, with  $k_{sk} = 1$ ,  $I_{eff} \sim 2$  for  $h_{in} = h_{sk}$  and reduces to almost optimal efficiency  $I_{eff} \sim 1$  for  $h_{in} = h_{sk}/2$  or  $h_{in} = h_{sk}/4$ . The influence of increasing the polynomial degree  $k_{in}$  with respect to  $k_{sk}$  is also significant. For example,  $I_{eff} \sim 2.3$  for  $k_{sk} = 2$ ,  $k_{in} = 3$ , and  $h_{in} = h_{sk}$ , and evolves to optimal efficiency  $I_{eff} \sim 1$  for the same configuration but with higher internal degree  $k_{in} = 4$ .

$k_{sk} = 1, k_{in} = 2$					$k_{sk} = 1, k_{in} = 3$				
$h_{sk}$	$E_{ex}$	$\eta_P$	$\eta_R$	$I_{eff}$	$h_{sk}$	$E_{ex}$	$\eta_P$	$\eta_R$	$I_{eff}$
$h_{in} = h_{sk}$					$h_{in} = h_{sk}$				
1/4	2.955e-02	5.959e-02	2.114e-02	2.140	1/4	2.856e-02	3.219e-02	1.047e-03	1.128
1/8	7.323e-03	1.473e-02	2.657e-03	2.045	1/8	7.098e-03	7.917e-03	6.576e-05	1.115
1/16	1.826e-03	3.678e-03	3.326e-04	2.022	1/16	1.772e-03	1.972e-03	4.115e-06	1.113
1/32	4.563e-04	9.192e-04	4.159e-05	2.016	1/32	4.428e-04	4.925e-04	2.572e-07	1.112
1/64	1.141e-04	2.298e-04	5.200e-06	2.015	1/64	1.107e-04	1.231e-04	1.608e-08	1.112
Rate	2.000	2.000	3.000	-	Rate	2.000	2.000	4.000	-
$h_{in} = h_{sk}/2$					$h_{in} = h_{sk}/2$				
1/4	2.083e-02	2.535e-02	2.657e-03	1.224	1/4	2.070e-02	2.192e-02	6.576e-05	1.059
1/8	6.290e-03	7.390e-03	3.326e-04	1.176	1/8	6.259e-03	6.658e-03	4.115e-06	1.064
1/16	1.688e-03	1.963e-03	4.159e-05	1.163	1/16	1.680e-03	1.790e-03	2.572e-07	1.065
1/32	4.357e-04	5.044e-04	5.200e-06	1.158	1/32	4.337e-04	4.621e-04	1.608e-08	1.066
1/64	1.106e-04	1.278e-04	6.500e-07	1.155	1/64	1.101e-04	1.173e-04	1.005e-09	1.066
Rate	1.978	1.981	3.000	-	Rate	1.978	1.978	4.000	-
$h_{in} = h_{sk}/4$					$h_{in} = h_{sk}/4$				
1/4	1.977e-02	2.050e-02	3.326e-04	1.037	1/4	1.976e-02	2.018e-02	4.115e-06	1.021
1/8	6.113e-03	6.328e-03	4.159e-05	1.035	1/8	6.111e-03	6.255e-03	2.572e-07	1.024
1/16	1.651e-03	1.708e-03	5.200e-06	1.035	1/16	1.650e-03	1.690e-03	1.608e-08	1.024
1/32	4.270e-04	4.416e-04	6.500e-07	1.034	1/32	4.268e-04	4.372e-04	1.005e-09	1.024
1/64	1.085e-04	1.122e-04	8.125e-08	1.034	1/64	1.084e-04	1.111e-04	6.281e-11	1.024
Rate	1.977	1.977	3.000	-	Rate	1.977	1.977	4.000	-
$k_{sk} = 2, k_{in} = 3$					$k_{sk} = 2, k_{in} = 4$				
$h_{sk}$	$E_{ex}$	$\eta_P$	$\eta_R$	$I_{eff}$	$h_{sk}$	$E_{ex}$	$\eta_P$	$\eta_R$	$I_{eff}$
$h_{in} = h_{sk}$					$h_{in} = h_{sk}$				
1/4	1.666e-03	3.952e-03	1.047e-03	2.453	1/4	1.658e-03	1.684e-03	4.137e-05	1.016
1/8	2.109e-04	4.894e-04	6.576e-05	2.341	1/8	2.107e-04	2.113e-04	1.298e-06	1.003
1/16	2.645e-05	6.096e-05	4.115e-06	2.310	1/16	2.645e-05	2.647e-05	4.060e-08	1.001
1/32	3.309e-06	7.613e-06	2.572e-07	2.302	1/32	3.309e-06	3.310e-06	1.269e-09	1.000
1/64	4.138e-07	9.514e-07	1.608e-08	2.300	1/64	4.138e-07	4.138e-07	3.966e-11	1.000
Rate	3.000	3.000	4.000	-	Rate	3.000	3.000	5.000	-
$h_{in} = h_{sk}/2$					$h_{in} = h_{sk}/2$				
1/4	1.063e-03	1.166e-03	6.576e-05	1.099	1/4	1.059e-03	1.076e-03	1.298e-06	1.016
1/8	1.730e-04	1.822e-04	4.115e-06	1.053	1/8	1.727e-04	1.735e-04	4.060e-08	1.005
1/16	2.414e-05	2.511e-05	2.572e-07	1.040	1/16	2.411e-05	2.415e-05	1.269e-09	1.001
1/32	3.173e-06	3.285e-06	1.608e-08	1.035	1/32	3.171e-06	3.172e-06	3.966e-11	1.000
1/64	4.062e-07	4.198e-07	1.005e-09	1.034	1/64	4.060e-07	4.061e-07	1.240e-12	1.000
Rate	2.965	2.968	4.000	-	Rate	2.965	2.966	4.999	-
$h_{in} = h_{sk}/4$					$h_{in} = h_{sk}/4$				
1/4	1.009e-03	1.016e-03	4.115e-06	1.007	1/4	1.008e-03	1.014e-03	4.060e-08	1.006
1/8	1.685e-04	1.689e-04	2.572e-07	1.002	1/8	1.684e-04	1.687e-04	1.269e-09	1.002
1/16	2.377e-05	2.379e-05	1.608e-08	1.001	1/16	2.376e-05	2.377e-05	3.966e-11	1.000
1/32	3.139e-06	3.141e-06	1.005e-09	1.001	1/32	3.139e-06	3.139e-06	1.240e-12	1.000
1/64	4.029e-07	4.031e-07	6.281e-11	1.001	1/64	4.028e-07	4.029e-07	-	1.000
Rate	2.962	2.962	4.000	-	Rate	2.962	2.962	4.999	-

Table 1 – Smooth solution approximated by the MHM-H(div)- $\mathcal{E}_\gamma$  method on square sub-regions using discretization parameters  $h_{sk} = 2^{-j}$ ,  $j = 2, \dots, 6$ ,  $h_{in} = h_{sk}/2^l$ ,  $l = 0, 1$  and  $2$ ,  $k_{sk} = i$ , and  $k_{in} = k_{sk} + i$ ,  $i = 1, 2$ .

(\*) - this missing residual error was saturated by rounding errors.

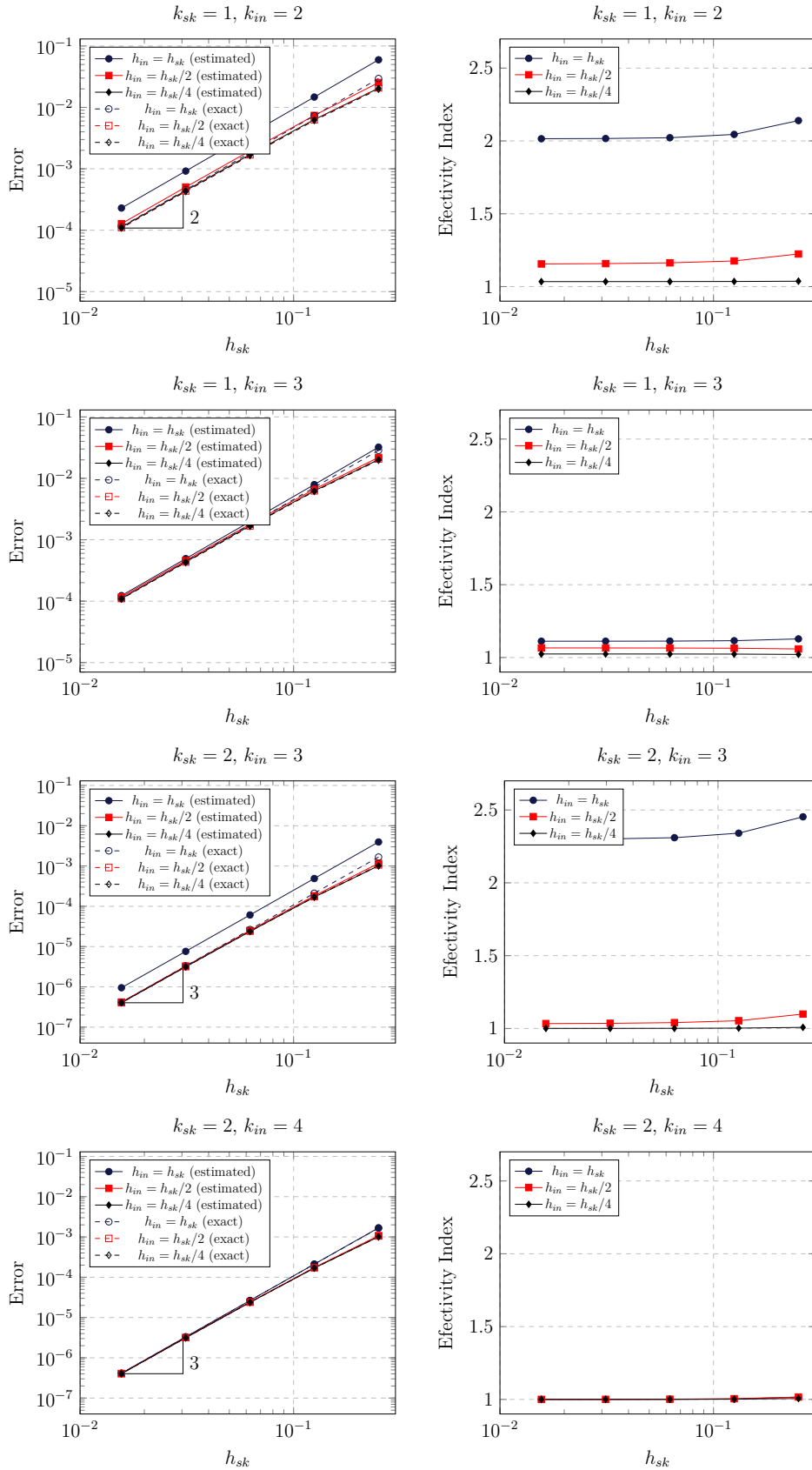


Figure 28 – Smooth solution approximated by the MHM-H(div)- $\mathcal{E}_\gamma$  method on square partitions using discretization parameters  $h_{sk} = 2^{-j}$ ,  $j = 2, \dots, 6$ ,  $h_{in} = h_{sk}/2^l$ ,  $l = 0, 1$  and  $2$ ,  $k_{sk} = i$ ,  $k_{in} = k_{sk} + i$ , with  $i = 1$  and  $2$ . Left plots: exact errors  $E_{ex}$  (dashed lines) and estimated errors  $E_{est}$  (continuous lines). Right plots: corresponding global effectivity indexes  $I_{eff}$ .

## 6.2 Singular solution on L- shape domain

The goal here is to study the performance of the error indicator and the effectivity index when the solution has a high gradient. For this purpose we consider the L-shaped domain  $\Omega = [-1, 1] \times [-1, 1] \setminus [0, 1] \times [-1, 0]$  and the exact solution given by  $u(r, \theta) = r^{2/3} \sin(2\theta/3)$  with Dirichlet boundary condition such that  $\partial\Omega = \Gamma_D$  and the permeability tensor  $\mathbb{K}$  is the identity. Observe that  $u(x, y) \in H^{3/2-\epsilon}$  for all  $\epsilon > 0$  and has the singularity at the origin of the L-shaped domain. There is no internal refinement with  $h_{in} = h_{sk} = 2^{-3}$ ,  $k_{sk} = 1$  and  $k_{in} = k_{sk} + 3 = 4$ .

The results for the local exact error and local estimated error per sub-region are plotted in Figure 29. Observed that the biggest values of the exact errors (Figure 29 (a)) and estimated errors (Figure 29 (b)) are around the origin of the domain, where the singularity is located. These results suggest that the error indicator defined on Theorem 3 can be used in adaptive process and the adaptive meshes should be refined into this corner.

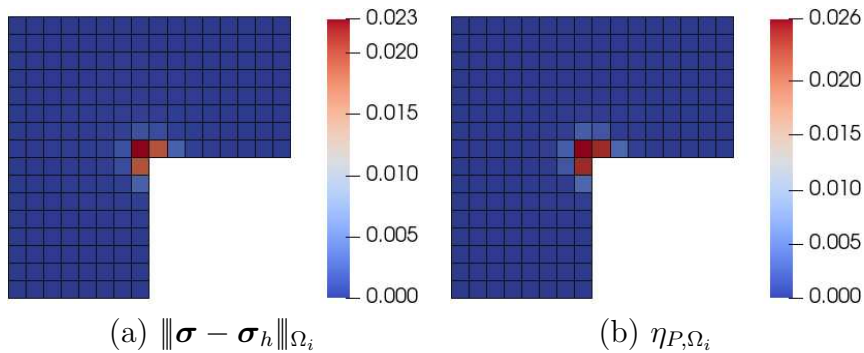
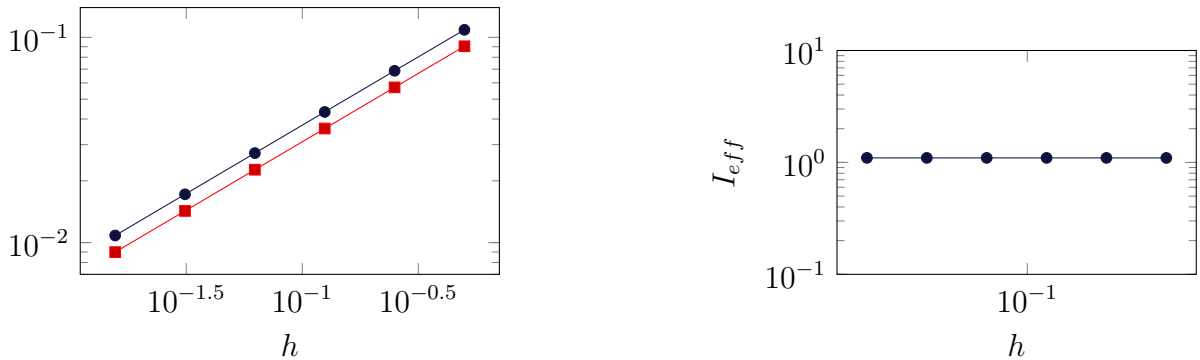


Figure 29 – Singular solution: (a) local exact error and (b) estimated error for L-shape mesh using space configurations of type  $k_{sk} = 1$  and  $k_{in} = k_{sk} + 3$ ,  $h_{in} = h_{sk} = 2^{-3}$ .

Figure 30 shows the history of convergence as  $h_{sk} \rightarrow 0$ .



(a) Estimated (blue) and exact (red) errors

(b) Effectivity index

Figure 30 – Historic of convergence for the singular problem. Left side: curves of estimated error and exact error; right side: curve of the effectivity index.

### 6.3 Solution with inner point singularity

The purpose of this numerical test is to observe the performance of the a posteriori estimator for the MHM-H(div)- $\mathcal{E}_\gamma$  method in the presence of the discontinuous permeability tensor  $\mathbb{K}$  defined in the region  $\Omega = [-1, 1] \times [-1, 1]$  by

$$\mathbb{K} = \begin{cases} 5\mathbb{I} & \text{for } \mathcal{R}_i \text{ with } i = 1, 3, \\ \mathbb{I} & \text{for } \mathcal{R}_i \text{ with } i = 2, 4, \end{cases} \quad (6.1)$$

where  $\mathcal{R}_1 = [0, 1] \times [0, 1]$ ,  $\mathcal{R}_2 = [-1, 0] \times [0, 1]$ ,  $\mathcal{R}_3 = [-1, 0] \times [-1, 0]$  and  $\mathcal{R}_4 = [0, 1] \times [-1, 0]$ .

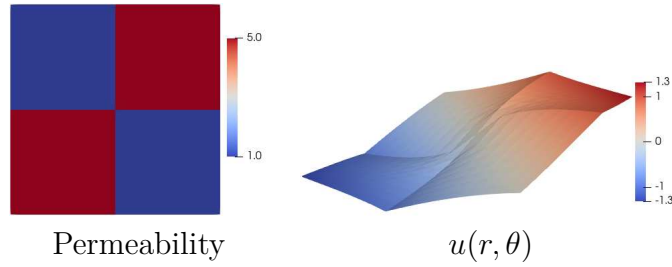


Figure 31 – Problem with inner singularity: permeability distribution and exact solution.

We solve the problem with  $f = 0$  and Dirichlet boundary condition associated to the exact solution

$$u(r, \theta) = \begin{cases} r^\alpha(0.447214\text{sen}(\alpha\theta) + \cos(\alpha\theta)), & \text{in } \mathcal{R}_1, \\ r^\alpha(2.33333 \cos(\alpha\theta) - 0.745356\text{sen}(\alpha\theta)), & \text{in } \mathcal{R}_2, \\ r^\alpha(1.0435\text{sen}(\alpha\theta) - 0.333333 \cos(\alpha\theta)), & \text{in } \mathcal{R}_3, \\ r^\alpha(2.23607\text{sen}(\alpha\theta) + \cos(\alpha\theta)) & \text{in } \mathcal{R}_4. \end{cases} \quad (6.2)$$

Note that  $u$  is the extension to  $\Omega$  of an eigenfunction of the Steklov problem on the unit circle  $S$  centered in the origin,  $-\mathbb{K}\nabla u \cdot \mathbf{n}^S = \alpha u$  on  $\partial S$ , with eigenvalue  $\alpha = 0.535441$ .  $\mathbb{K}$  and  $u$  are illustrated in Figure 31.

We apply the MHM-H(div)- $\mathcal{E}_\gamma$  method with discretization parameters  $k_{sk} = 1$ ,  $k_{in} = 2$  and 3, on a sequence of square subregions with  $h_{sk} = 2^{-j}$ , with  $j = 2, \dots, 6$ , and uniform square internal local partitions with  $h_{in} = h_{sk}/2^l$ ,  $l = 0, 1$ , and 2. For this divergence-free problem, with full Dirichlet boundary condition, the estimated errors are taken as  $E_{\text{est}} = \eta_P = \left( \sum_{\Omega_i \in \mathcal{T}_{h_{sk}}} \eta_{P, \Omega_i}^2 \right)^{1/2}$ . The more complex error indicators  $\eta_{D, \Omega_i}$  are not included in the estimators, since they are expected to be negligible with respect to  $\eta_{P, \Omega_i}$ .

The results for the exact errors  $E_{\text{ex}}$ , estimated errors  $\eta_P$ , and effectivity indexes  $I_{\text{eff}}$  are summarized in Table 2. Convergence histories are presented in the left plots of Figure 32 for the exact errors (dashed lines) and the estimated errors (continuous lines), versus  $h_{sk}$ .

$k_{sk} = 1, k_{in} = 2$				$k_{sk} = 1, k_{in} = 3$			
$h_{sk}$	$E_{ex}$	$\eta_P$	$I_{eff}$	$h_{sk}$	$E_{ex}$	$\eta_P$	$I_{eff}$
$h_{in} = h_{sk}$				$h_{in} = h_{sk}$			
1/4	4.594e-01	7.879e-01	1.715	1/4	4.540e-01	7.706e-01	1.697
1/8	3.178e-01	5.465e-01	1.720	1/8	3.141e-01	5.344e-01	1.702
1/16	2.195e-01	3.780e-01	1.722	1/16	2.170e-01	3.696e-01	1.704
1/32	1.516e-01	2.611e-01	1.723	1/32	1.498e-01	2.553e-01	1.705
1/64	1.046e-01	1.802e-01	1.723	1/64	1.034e-01	1.762e-01	1.705
Rate	0.534	0.532	-	Rate	0.534	0.532	-
$h_{in} = h_{sk}/2$				$h_{in} = h_{sk}/2$			
1/4	4.560e-01	6.693e-01	1.468	1/4	4.557e-01	6.610e-01	1.450
1/8	3.155e-01	4.642e-01	1.471	1/8	3.153e-01	4.584e-01	1.454
1/16	2.179e-01	3.210e-01	1.473	1/16	2.178e-01	3.170e-01	1.456
1/32	1.504e-01	2.218e-01	1.474	1/32	1.504e-01	2.190e-01	1.457
1/64	1.038e-01	1.531e-01	1.474	1/64	1.038e-01	1.512e-01	1.457
Rate	0.534	0.532	-	Rate	0.534	0.532	-
$h_{in} = h_{sk}/4$				$h_{in} = h_{sk}/4$			
1/4	4.558e-01	6.003e-01	1.317	1/4	4.558e-01	5.955e-01	1.307
1/8	3.153e-01	4.164e-01	1.320	1/8	3.153e-01	4.130e-01	1.310
1/16	2.178e-01	2.880e-01	1.322	1/16	2.178e-01	2.856e-01	1.311
1/32	1.504e-01	1.989e-01	1.323	1/32	1.504e-01	1.973e-01	1.312
1/64	1.038e-01	1.373e-01	1.323	1/64	1.038e-01	1.362e-01	1.312
Rate	0.534	0.532	-	Rate	0.534	0.532	-

Table 2 – Solution with inner singularity approximated by the MHM-H(div)- $\mathcal{E}_\gamma$  method based on square partitions, with discretization parameters  $h_{sk} = 2^{-j}$ ,  $j = 2, \dots, 6$ ,  $h_{in} = h_{sk}/2^l$ ,  $l = 0, 1$ , and  $2$ ,  $k_{sk} = 1$ ,  $k_{in} = 2$  and  $3$ .

Due to the low regularity of the true solution around the origin, the observed rate of convergence is of order  $\sim 0.535$ , both for exact and estimated errors, a result compatible with the regularity index of the exact solution inside the quadrants  $\mathcal{R}_i$  of constant permeability.

The plots on the right in Figure 32 are for the corresponding global effectivity indexes, indicating a stable good behavior as the coarse partitions are refined. Moreover, the effectivity index improves when  $h_{in}$  decreases, but it seems to be less influenced by the adopted polynomial degree adopted inside the subregions.

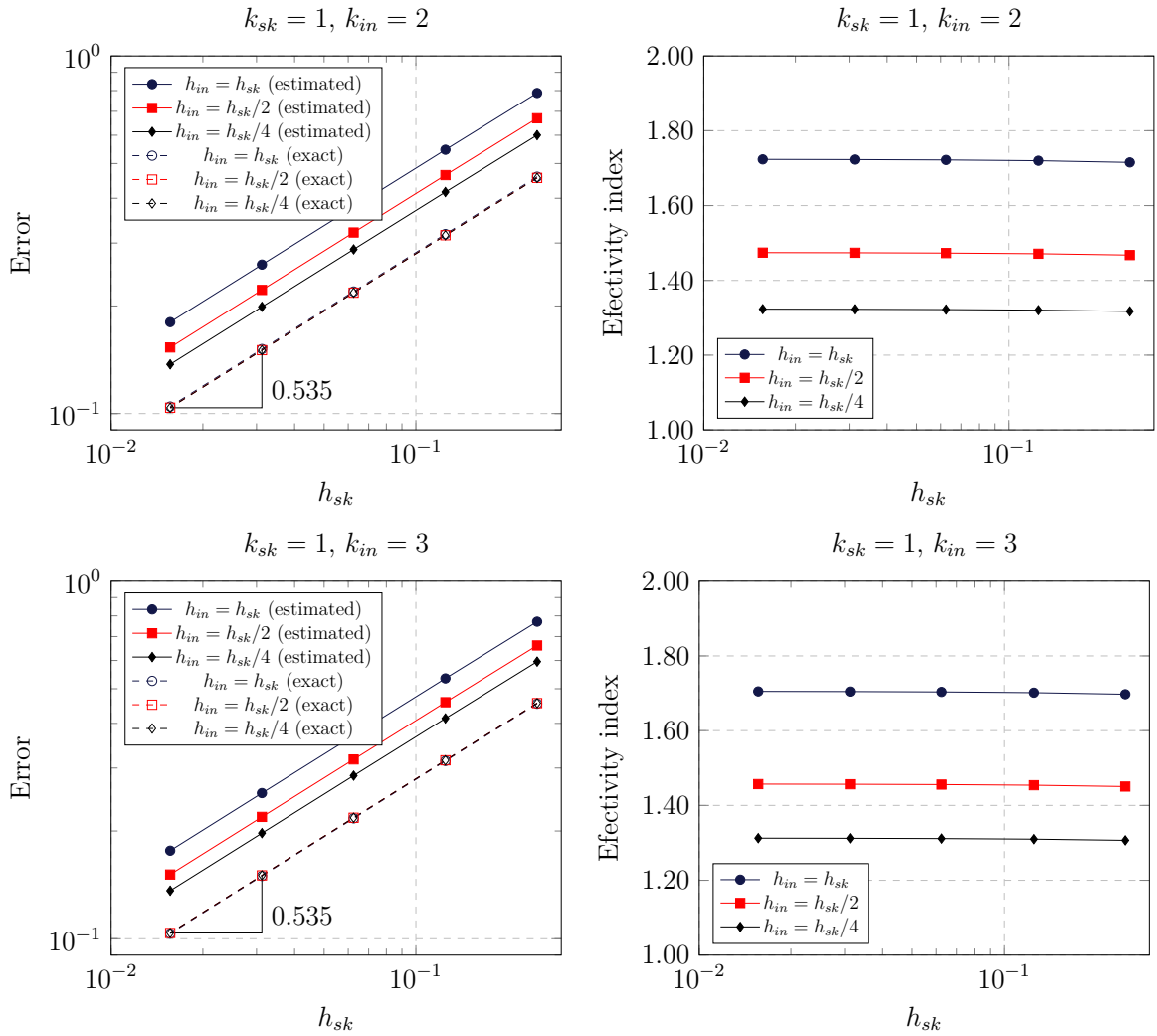


Figure 32 – Solution with inner singularity approximated by the MHM-H(div)- $\mathcal{E}_\gamma$  method based on square partitions using discretization parameters  $h_{sk} = 2^{-j}$ ,  $j = 2, \dots, 6$ ,  $h_{in} = h_{sk}/2^l$ ,  $l = 0, 1$  and  $2$ ,  $k_{sk} = 1$ ,  $k_{in} = 2$ , and  $3$ . Left plots: exact errors (dashed lines) and the estimated errors (continuous lines). Right plots: corresponding global effectivity indexes.

### 6.3.1 Solution with a corner strong gradient

In this section the numerical tests are for the model problem with  $\mathbb{K} = \mathbb{I}$  in  $\Omega = [0, 1] \times [0, 1]$ ,  $\Gamma_D = \partial\Omega$ ,  $u_D = 0$ . The source term  $f$  is such that  $u(x, y) = xy(1-x)(1-y)e^{10x+10y}/537930$  is the exact solution, having strong gradient around the corner  $(1, 1)$ , as illustrated in Figure 33. For this problem we show simulation results obtained using a two-level setting and by the application of the two  $h$ -adaptive Algorithm 1 and Algorithm 2.

#### 6.3.1.1 A two-level numerical test

The first test is for a two-level setting for  $\mathcal{T}$  composed by  $5 \times 5$  square elements ( $h_{sk} = \frac{1}{5}$ ), and sub-partitions  $\mathcal{T}_{h_{in}}^{\Omega_i}$  with  $h_{in} = h_{sk}/2$ . The finite element spaces are for polynomial degrees  $k_{sk} = 1$  and  $k_{in} = 3$ .

The local errors in each macro domain  $\Omega_i \in \mathcal{T}$  are shown in Figure 33 (in logarithmic scale). Observe that, as expected, the exact and estimated local errors are more significant around the corner  $(1, 1)$ . Figure 33 also shows the local effectivity indexes  $\eta_{P,\Omega_i}$  indicating that the estimated errors are effective when applied to a problem with high gradient. In this case, the global effectivity index is  $I_{eff} = 1.07$ .

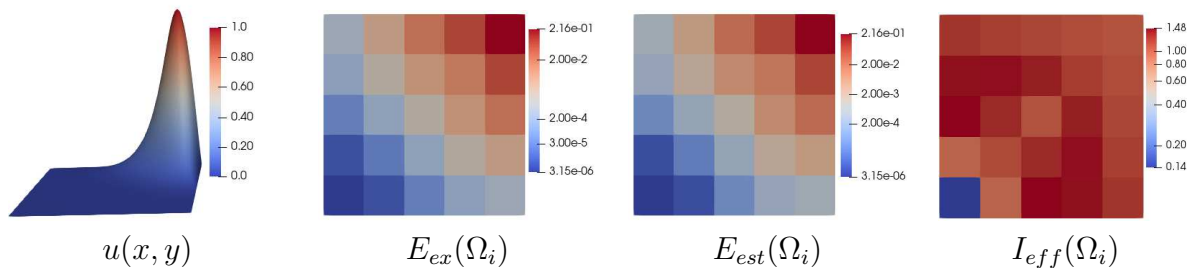


Figure 33 – Solution with high corner gradient approximated by the MHM-H(div)- $\mathcal{E}_\gamma$  method based two-level finite element setting for uniform coarse square partition, for  $h_{sk} = 1/5$ ,  $h_{in} = h_{sk}/2$ ,  $k_{ks} = 1$ , and  $k_{in} = 3$ : the exact solution  $u(x, y)$ , local exact errors, local estimated errors, and local effectivity indexes in each macro domain  $\Omega_i \in \mathcal{T}$ .

#### 6.3.1.2 Comparison of adaptive strategies

We apply Algorithm 1, with the fixed partition  $\mathcal{T}^0$  of  $3 \times 3$  square subregions ( $h_{sk} = 1/3$ ). The subregion partitions  $\mathcal{T}_{h_{in}}^{\Omega_i}$ , as well as the boundary edges, are at the finest refinement level  $h_{in} = h_{sk}/2^6$ . The finite element space settings  $\mathcal{E}_\gamma$  use polynomial degrees  $k_{sk} = 1$  and  $k_{in} = 2$ . Starting from the initial skeleton partition  $\mathcal{T}^{\Gamma,0}$ , six refinement steps of Algorithm 1 are applied to give  $h$ -adapted skeleton partitions  $\mathcal{T}^{\Gamma,\ell}$ ,  $\ell = 1, \dots, 6$ .

Illustrations of  $\mathcal{T}^{\Gamma,\ell}$ , for  $\ell = 0, 1, 4$  and  $6$ , are plotted on the top side of Figure 34. Initially, at level  $\ell = 1$ , only the internal edges of the three subregions closest to the

corner  $(1, 1)$  are refined. At the final refinement level  $\ell = 6$ , the edges of all subregions have been submitted to some refinement extent, which increases towards the corner singularity point. As shown in the zoom in detail, the finest mesh width  $h_{in}$  is reached on the edges of  $\mathcal{T}^{\Gamma,6}$  on the closest subregion to the singularity corner. For comparison, we perform the

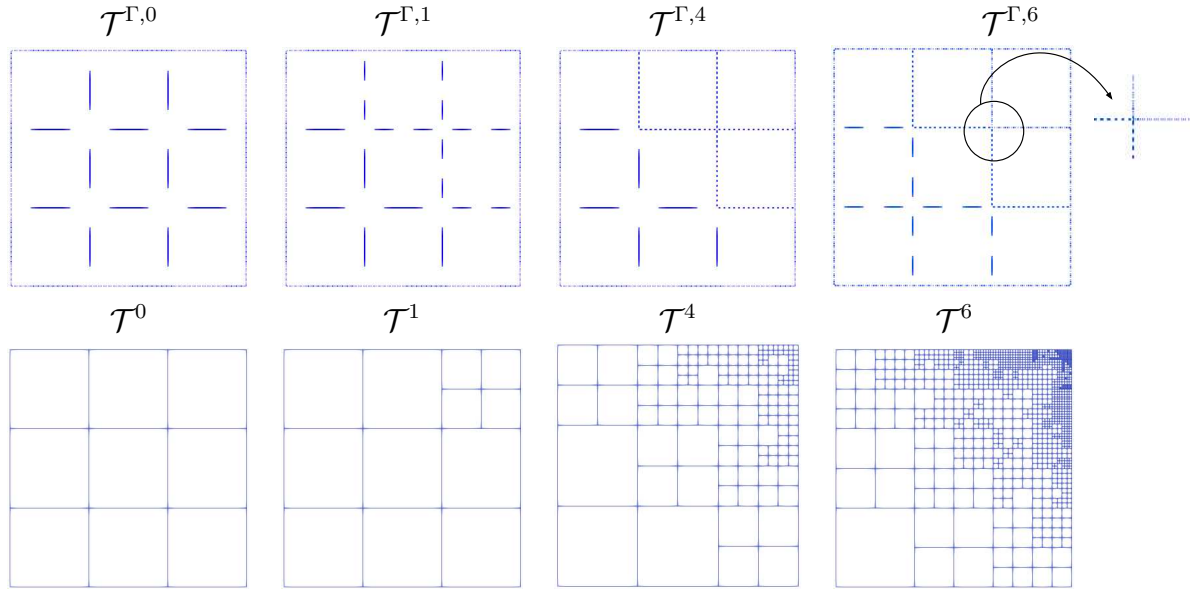


Figure 34 – Solution with high corner gradient approximated by the MHM-H(div)- $\mathcal{E}_\gamma$  method for  $\mathcal{E}_\gamma$  based on a sequence of six  $h$ -adaptive partitions: by refinement of the skeleton partition of Algorithm 1 (top meshes), and refinement of the subregions of Algorithm 2 (bottom meshes).

MHM-H(div)- $\mathcal{E}_\gamma$  method by the classic  $h$ -adaptive process of Algorithm 2, using tolerance threshold  $\epsilon = 0.2$  (meaning that 20% of the elements with largest error indicators are refined in each step). Recall that the square subregions  $\Omega_i$  do not have internal sub-partitions, i.e.,  $\mathcal{T}^{\Omega_i} = \Omega_i$ . We start with the same initial coarse partition  $\mathcal{T}^0$  composed by  $3 \times 3$  subregions and apply six refinement steps to obtain  $h$ -adapted partitions  $\mathcal{T}^\ell$ ,  $\ell = 1, \dots, 6$ . Some of them, for  $\ell = 0, 1, 4$ , and 6 are shown on the bottom side of Figure 34, revealing that the refined elements are concentrated around the corner  $(1, 1)$  where the solution is less regular.

Exact and estimated error curves for the MHM-H(div)- $\mathcal{E}_\gamma$  method based on these  $h$ -adaptive space configurations  $\mathcal{E}_\gamma$  are plotted in the left side of Figure 35 versus the number of required degrees-of-freedom (DoF). For comparison, results for uniform refinements are also shown. Observe that the  $h$ -adaptive settings demonstrate to be more efficient than the uniform scheme, specially for the trace adaptive Algorithm 2, with a strong error decay and high reduction of the number of equations to be solved.

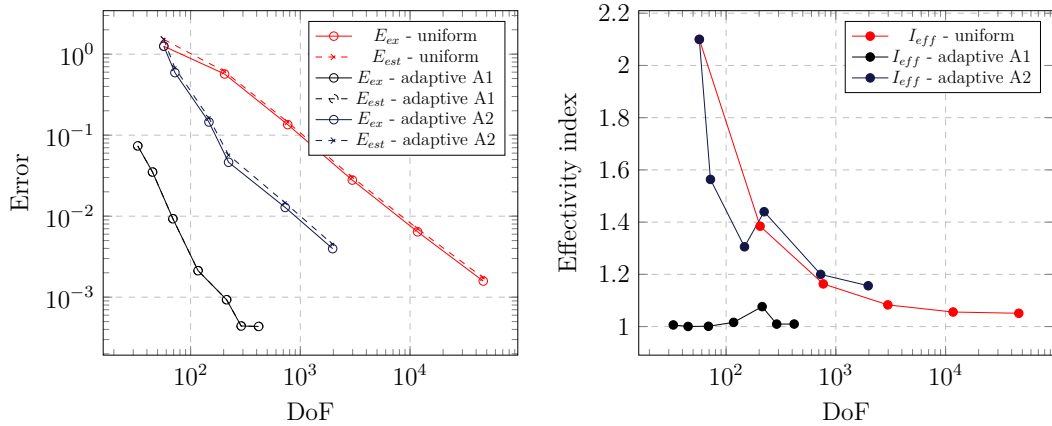


Figure 35 – Solution with high corner gradient approximated by the MHM-H(div)- $\mathcal{E}_\gamma$  method based on uniform partitions (red lines), on  $h$ -adaptive trace partitions by Algorithm 1 (A1 - black lines), on  $h$ -adaptive partitions by Algorithm 2 (A2 - blue lines), using  $k_{ks} = 1$  and  $k_{in} = 3$ . Left plots: exact errors  $E_{ex}$  (continuous lines) and estimator errors  $E_{est}$  (dashed lines) versus DoF. Right plots: effectivity indexes  $I_{eff}$  for uniform and adaptive settings.

### 6.3.2 Flow in heterogeneous porous media: trace adaptivity

The last example refers to a divergence-free flow ( $f = 0$ ) in a heterogeneous reservoir model. We consider the 2D dataset of the 36th layer of the SPE10 benchmark problem on a rectangular domain  $\Omega = [0, 208] \times [0, 48]$ , and heterogeneous permeability distribution, as plotted in Figure 36 (shown in the logarithmic scale). The Dirichlet boundary is split into  $\Gamma_D = \Gamma_{D,0} \cup \Gamma_{D,1}$  where  $\Gamma_{D,0} = \{(x, y) : x = 0, 0 \leq y \leq 48\}$  and  $\Gamma_{D,1} = \{(x, y) : x = 208, 0 \leq y \leq 48\}$ . The boundary condition  $u_D = 0$  is enforced on  $\Gamma_{D,0}$  and  $u_D = 1$  is enforced on  $\Gamma_{D,1}$ . Elsewhere, vanishing Neumann boundary condition  $\sigma_N = 0$  is applied.

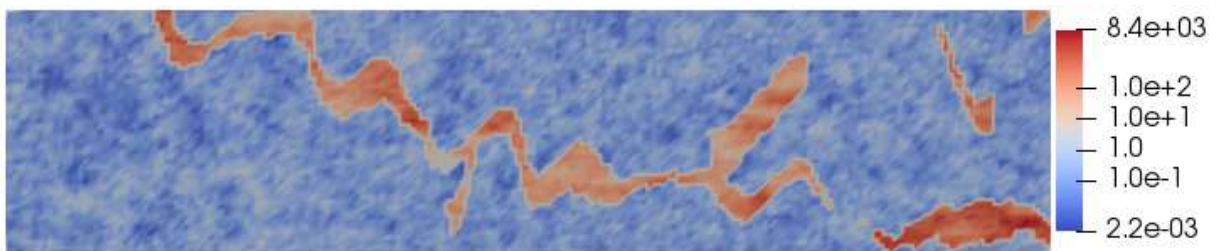


Figure 36 – Heterogenous permeability (in log distribution).

The domain  $\Omega$  is discretized taking  $13 \times 3$  coarse square subregions  $\Omega_i$  forming  $\mathcal{T}^0$ , with fully refined sub-partitions  $\mathcal{T}_{h_{in}}^{\Omega_i}$  ( $h_{in} = 1$ ). The space configurations  $\mathcal{E}_\gamma$  are for polynomial degree  $k_{sk} = 1$  over the skeleton partition and local subspaces  $\mathcal{V}_\gamma(\Omega_i) \times \mathcal{U}_{\gamma_{in}}(\Omega_i)$  with  $k_{in} = 4$ . A sequence of  $h$ -adapted skeleton partitions  $\mathcal{T}^{\Gamma, \ell}$ ,  $\ell = 1, \dots, 8$  are computed by Algorithm 1. The purpose is to verify the reliability of the error indicator  $\eta_{P, \Omega_i}$ , given by Theorem 3, to detect the regions where the trace refinement is necessary to choose an

appropriate skeleton partition in the presence of this highly heterogeneous permeability configuration. We emphasize that no reference solution is used.

The illustrations in Figure 38, for  $\ell = 0, 1, 3, 6,$  and  $8$  show the strong decay of the local estimated errors  $E_{est}(\Omega_i)$  (indicated by color scales) following the adaptive refinement of the trace partitions  $\mathcal{T}^{\Gamma, \ell}$ .

The fields after the last level of the trace adaptivity are shown in Figure 37. The approximate potential  $\tilde{u}$  is indicated by a background color map. The flux  $\tilde{\sigma}$  is plotted as glyphs, scaled by the factor 150.

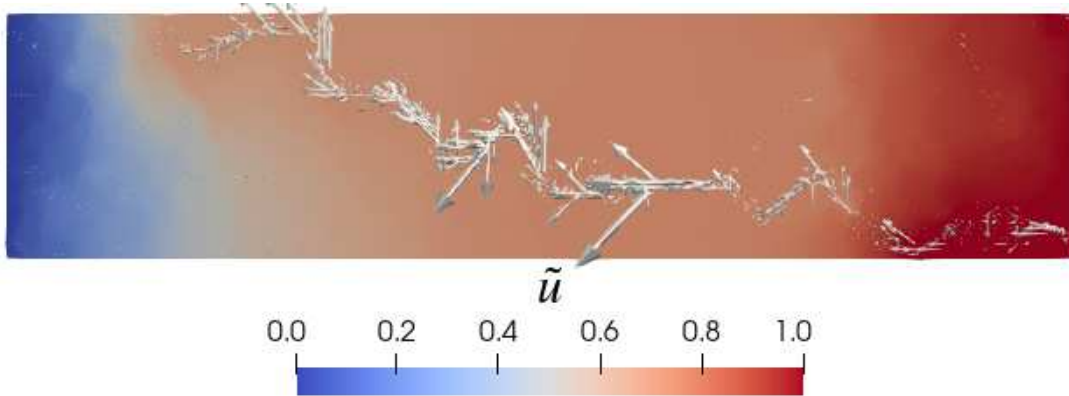


Figure 37 – Darcy’s model with heterogeneous permeability: approximation potential  $\tilde{u}$  and flux  $\tilde{\sigma}$  by the MHM-H(div)- $\mathcal{E}_\gamma$  based on the coarse sub-region partition  $\mathcal{T}^0$ , the trace adapted partition  $\mathcal{T}^{\Gamma, 8}$ , internal sub-partitions  $\mathcal{T}_{h_{in}}^{\Omega_i}$ , with  $h_{in} = 1$ , polynomial degrees  $k_{sk} = 1$ , and  $k_{in} = 4$ .

The evolution of the corresponding global estimated errors  $E_{est}$  are plotted in Figure 39. For comparison, estimated errors obtained by uniform refinement of the skeleton mesh are also shown. As observed in the previous example for the solution with strong corner gradient, the trace  $h$ -adaptive process applied to this heterogeneous flow problem also provides a fast error decay, with a strong reduction of the degrees-of-freedom.

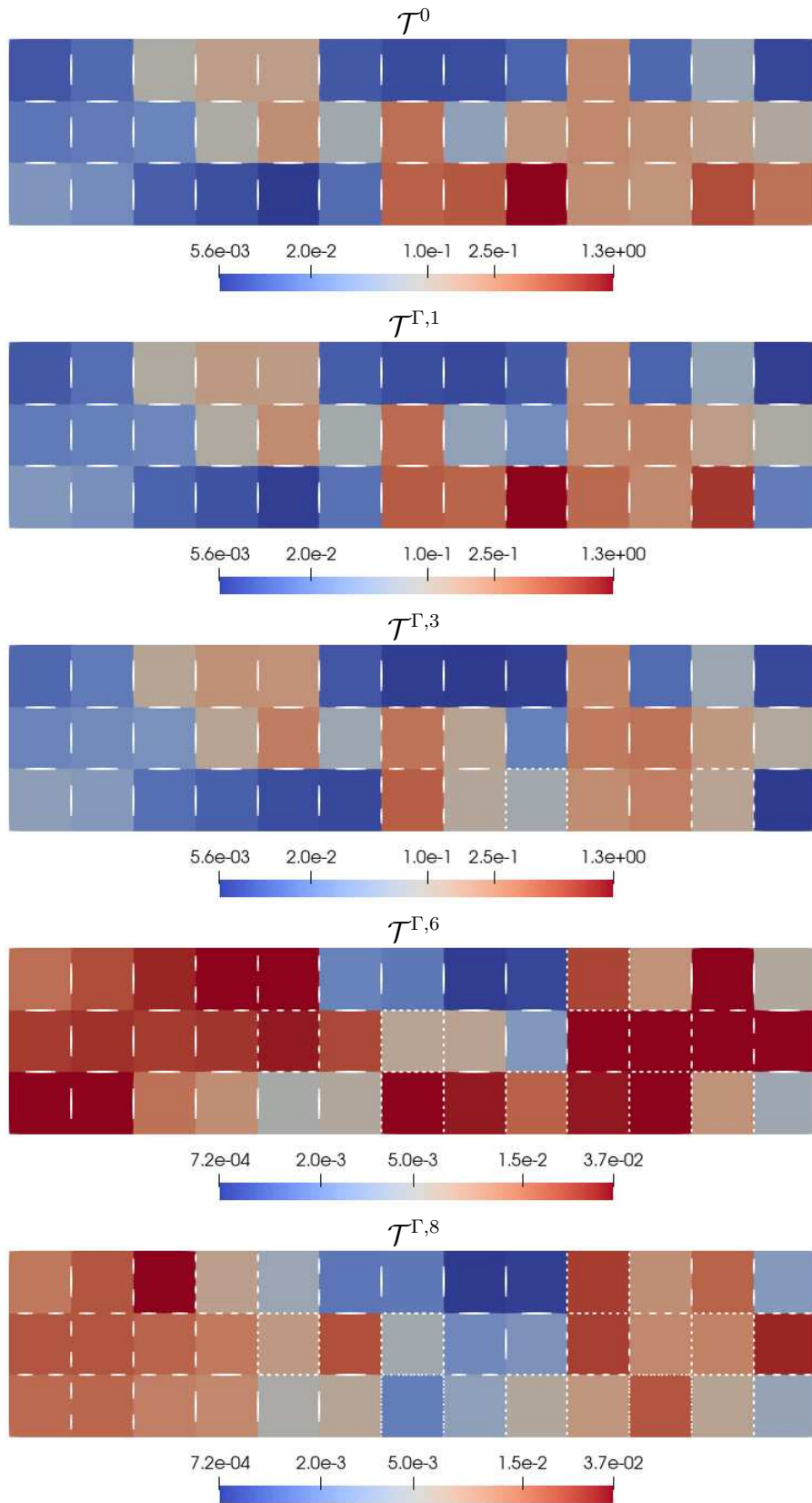


Figure 38 – Darcy's model with heterogeneous permeability:  $h$ -adapted skeleton partitions  $\mathcal{T}^{\Gamma,\ell}$ ,  $\ell = 1, 3, 6$  and  $8$ , and local estimated errors  $\eta_{P,\Omega_i}$  of adaptive solutions obtained by Algorithm 1 for the MHM-H(div)- $\mathcal{E}_\gamma$  formulation using the fixed coarse sub-region partition  $\mathcal{T}^0$  and internal sub-partitions  $\mathcal{T}_{h_{in}}^{\Omega_i}$ , with  $h_{in} = 1$ , polynomial degrees  $k_{sk} = 1$ , and  $k_{in} = 4$ .

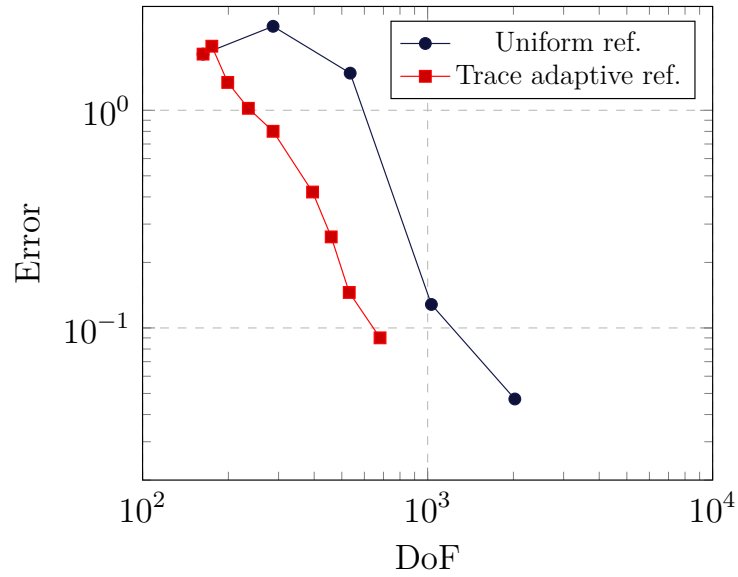


Figure 39 – Darcy’s model with heterogeneous permeability: estimated errors of adaptive solutions of the MHM-H(div)- $\mathcal{E}_\gamma$  formulation obtained by Algorithm 1 using space configurations based on the fixed coarse sub-region  $\mathcal{T}^0$ , internal sub-partitions  $\mathcal{T}_{h_{in}}^{\Omega_i}$ , with  $h_{in} = 1$ , trace adapted partitions  $\mathcal{T}^{\Gamma,\ell}$ ,  $\ell = 1, \dots, 8$ , polynomial degrees  $k_{sk} = 1$ , and  $k_{in} = 4$ .

## 7 Conclusion

In this work, an a posteriori error estimator is presented for the Multiscale Hybrid Mixed method. The estimator is based on a posteriori error estimations for standard single-scale mixed methods presented in the literature to the multiscale MHM-H(div)- $\mathcal{E}_\gamma$  context. The proposed methodology based on a reconstruction procedure aimed to recover a second continuous approximation for pressure to estimate the unknown exact flux and pressure errors. The results demonstrated the efficiency of the proposed approach by computing the efficiency index in problems with known exact solutions.

Moreover, the error estimator provides computable error bounds. The approach can be used to identify regions of the domain in which the approximation error is greater, which allows for the use in adaptive mesh refinement procedures. The obtained results confirmed the applicability of the proposed method to optimize multiscale simulations, which is particularly required in the context of heterogeneous materials with fine-scale characteristics.

The algorithm was implemented in the NeoPZ environment, an open-source, cross-platform, finite element library written in C++. This implementation ensures that the proposed approach is readily available to researchers and engineers who work with multiscale simulations. The developed code can also be used as a starting point for further research in the area, and it is expected to contribute to the development of new applications for multiscale methods in different fields of engineering.

# Bibliography

- AARNES, J. E. On the use of a mixed multiscale finite element method for greater flexibility and increased speed or improved accuracy in reservoir simulation. *Multiscale Modeling & Simulation*, v. 2, n. 3, p. 421–439, 2004. Available at: <<https://doi.org/10.1137/030600655>>. Cited in page 13.
- AINSWORTH, M. A posteriori error estimation for lowest order raviart-thomas mixed finite elements. *SIAM J Sci Comput*, v. 30, n. 1, p. 189–204, 2007. Cited in page 45.
- AINSWORTH, M. A framework for obtaining guaranteed error bounds for finite element approximations. *Journal of Computational and Applied Mathematics*, Elsevier BV, v. 234, n. 9, p. 2618–2632, set. 2010. Available at: <<https://doi.org/10.1016/j.cam.2010.01.037>>. Cited 2 times in pages 14 and 42.
- AINSWORTH, M.; MA, X. Non-uniform order mixed FEM approximation: Implementation, post-processing, computable error bound and adaptivity. *Journal of Computational Physics*, Elsevier BV, v. 231, n. 2, p. 436–453, jan. 2012. Available at: <<https://doi.org/10.1016/j.jcp.2011.09.011>>. Cited 4 times in pages 43, 44, 46, and 48.
- ARAYA, R. et al. Multiscale hybrid-mixed method. *SIAM Journal on Numerical Analysis*, Society for Industrial & Applied Mathematics (SIAM), v. 51, n. 6, p. 3505–3531, jan. 2013. Available at: <<https://doi.org/10.1137/120888223>>. Cited in page 13.
- BABUŠKA, I.; RHEINBOLDT, W. Error estimates for adaptive finite element computations. *SIAM Journal on Numerical Analysis*, Society for Industrial & Applied Mathematics (SIAM), v. 15, n. 4, p. 736–754, aug 1978. Available at: <<https://doi.org/10.1137/0715049>>. Cited in page 14.
- BECKER, E. B.; CAREY, G. F.; ODEN, J. T. *Finite elements: An introduction*. New Jersey, USA: Prentice Hall Inc., 1981. v. 1. ISBN 9780133170573. Cited 2 times in pages 15 and 30.
- BOFFI, D.; BREZZI, F.; FORTIN, M. *Mixed Finite Element Methods and Applications*. [S.l.]: Springer-Verlag, 2013. v. 44. Cited in page 31.
- BREZZI, F.; DOUGLAS, J.; MARINI, L. D. Two families of mixed finite elements for second order elliptic problems. *Numerische Mathematik*, Springer Science and Business Media LLC, v. 47, n. 2, p. 217–235, jun. 1985. Available at: <<https://doi.org/10.1007/bf01389710>>. Cited in page 31.
- CALLE, J.; DEVLOO, P.; GOMES, S. Implementation of continuous hp-adaptive finite element spaces without limitations on hanging sides and distribution of approximation orders. *Comput Method Appl*, v. 70, n. 5, p. 1051–1069, 2015. Cited in page 50.
- CASTRO, D. A. et al. Hierarchical high order finite element bases for  $h(\text{div})$  spaces based on curved meshes for two-dimensional regions or manifolds. *Journal of Computational and Applied Mathematics*, v. 301, p. 241 – 258, 2016. ISSN 0377-0427. Available at: <<http://www.sciencedirect.com/science/article/pii/S0377042716300334>>. Cited in page 25.

CIARLET, P. G. *The Finite Element Method for Elliptic Problems*. Society for Industrial and Applied Mathematics, 2002. Available at: <<https://doi.org/10.1137/1.9780898719208>>. Cited in page 15.

DEMKOWICZ, L. Polynomial exact sequences and projection-based interpolation with application to maxwell equations. In: *Mixed Finite Elements, Compatibility Conditions, and Applications*. Berlin, Heidelberg: Springer, 2008. v. 1939, p. 101–158. Cited in page 37.

DEVLOO, P. R.; FARIAS, A. M.; GOMES, S. M. A remark concerning divergence accuracy order for h(div)-conforming finite element flux approximations. *Computers & Mathematics with Applications Mathematics with Applications*, Elsevier BV, v. 77, n. 7, p. 1864–1872, apr 2019. Cited in page 31.

DEVLOO, P. R. et al. Two-dimensional hp adaptive finite element spaces for mixed formulations. *Mathematics and Computers in Simulation*, Elsevier BV, v. 126, p. 104–122, ago. 2016. Available at: <<https://doi.org/10.1016/j.matcom.2016.03.009>>. Cited in page 25.

DEVLOO, P. R. B. Pz: An object oriented environment for scientific programming. *Computer Methods in Applied Mechanics and Engineering*, v. 150, n. 1, p. 133 – 153, 1997. ISSN 0045-7825. Symposium on Advances in Computational Mechanics. Available at: <<http://www.sciencedirect.com/science/article/pii/S0045782597000972>>. Cited in page 14.

DEVLOO, P. R. B.; BRAVO, C. M. A. A.; RYLO, E. C. Systematic and generic construction of shape functions for p-adaptive meshes of multidimensional finite elements. *Computer Methods in Applied Mechanics and Engineering*, v. 198, n. 21, p. 1716 – 1725, 2009. ISSN 0045-7825. Advances in Simulation-Based Engineering Sciences – Honoring J. Tinsley Oden. Available at: <<http://www.sciencedirect.com/science/article/pii/S0045782509000255>>. Cited in page 21.

DOLEJŠÍ, V.; ERN, A.; VOHRALÍK, M. hp-adaptation driven by polynomial-degree-robust a posteriori error estimates for elliptic problems. *SIAM J Sci Comput*, v. 38, p. A3220–A3246, 2016. Cited 2 times in pages 46 and 48.

DURÁN, O. et al. A multiscale hybrid method for Darcy’s problems using mixed finite element local solvers. *Computer Methods in Applied Mechanics and Engineering*, v. 354, p. 213 – 244, 2019. ISSN 0045-7825. Cited 4 times in pages 13, 35, 37, and 40.

FORTI, T. L. et al. A comparative numerical study of different finite element formulations for 2d model elliptic problems: Continuous and discontinuous galerkin, mixed and hybrid methods. *Finite Elements in Analysis and Design*, Elsevier BV, v. 115, p. 9–20, ago. 2016. Available at: <<https://doi.org/10.1016/j.finel.2016.02.009>>. Cited in page 31.

FUENTES, F. et al. Orientation embedded high order shape functions for the exact sequence elements of all shapes. *Comput Math Appl*, v. 70, p. 353–458, 2015. Cited in page 31.

HARDER, C.; PAREDES, D.; VALENTIN, F. A family of multiscale hybrid-mixed finite element methods for the darcy equation with rough coefficients. *J Comput Phys*, v. 245, p. 107–130, 2013. Cited in page 38.

- PAULY, D.; VALDMAN, J. Poincaré-Fridrichs type constants for operators involving grad, curl, and div: Theory and numerical experiments. *Comput Math Appl*, v. 79, n. 11, p. 3027–3067, 2020. Cited in page 44.
- PIETRO, D.; DRONIOU, J. A hybrid high-order method for Leray–Lions elliptic equations on general meshes. *Math Comput*, v. 86, p. 2159–2191, 2017. Cited in page 44.
- PIETRO, D. D.; ERN, A. *Mathematical aspects of discontinuous Galerkin methods*. [S.l.]: Springer Science, 2012. v. 69. Cited in page 44.
- RAVIART, P. A.; THOMAS, J. M. A mixed finite element method for 2nd order elliptic problems. In: *Lecture Notes in Mathematics*. Springer Berlin Heidelberg, 1977. p. 292–315. Available at: <<https://doi.org/10.1007/bfb0064470>>. Cited in page 31.
- VOHRALÍK, M. Unified primal formulation-based a priori and a posteriori error analysis of mixed finite element methods. *Mathematics of Computation*, American Mathematical Society (AMS), v. 79, n. 272, p. 2001–2001, 2010. Available at: <<https://doi.org/10.1090/s0025-5718-2010-02375-0>>. Cited in page 42.
- VOHRALÍK, M. *A posteriori error estimates for efficiency and error control in numerical simulations*. 2015. Lecture notes. Available at: <[https://who.rocq.inria.fr/Martin.Vohralik/Enseig/APost/a\\_posteriori.pdf](https://who.rocq.inria.fr/Martin.Vohralik/Enseig/APost/a_posteriori.pdf)>. Access date: 25 jun. 2018. Cited 3 times in pages 14, 42, and 43.

# APPENDIX A – Proof of Theorems

## A.1 Proof of Theorem 1

Before going throughout of Theorem 1, consider the mapping  $R : \Lambda_\gamma \rightarrow U_0$  defined by  $\int_{\Omega_i} R(\lambda) v dx = \int_{\partial\Omega_i} \epsilon_i \lambda v ds, \forall v \in U_0$ .

**Lemma 2.** *The mapping  $R$  restricted to the subspace  $\mu \in \Lambda_\gamma; \mu|_{\Gamma_N} = 0$  is surjective on  $U_0$ .*

*Proof.* Given  $v^* \in U_0$ , let  $\boldsymbol{\tau}^* \in H^1(\Omega, \mathbb{R}^d)$  satisfying  $\nabla \cdot \boldsymbol{\tau}^* = v^*$ , with  $\boldsymbol{\tau}^* \cdot \mathbf{n}^\Omega|_{\Gamma_N} = 0$ . Then, define  $\tilde{\lambda}^* = \tilde{\boldsymbol{\tau}}^* \cdot \mathbf{n}|_\Gamma$ , where  $\tilde{\boldsymbol{\tau}}^* = \Pi_\gamma^\sigma \boldsymbol{\tau}^* \in \mathcal{V}_\gamma$ . Thus,  $\tilde{\lambda}^* \in \Lambda_\gamma$ ,  $\tilde{\lambda}^*|_{\Gamma_N} = 0$ , and the assumption  $v^* \in U_0 \subset U_{\gamma_{in}}$  implies that  $\nabla \cdot \tilde{\boldsymbol{\tau}}^* = v^*$ . Consequently,  $\int_{\Omega_i} v^* v dx = \int_{\partial\Omega_i} \boldsymbol{\tau}^* \cdot \mathbf{n}^{\Omega_i} v ds = \int_{\partial\Omega_i} \epsilon_i \tilde{\lambda}^* v ds$ , for all  $v \in U_0$ , meaning that  $R\tilde{\lambda}^* = v^*$ , and the result follows.  $\square$

Theorem 1 states uniqueness of solution for the local (4.3)-(4.4) and global (4.5) systems. The well posedness of the local systems (4.3) and (4.4) is a consequence of the divergence-compatibility of the local finite element pairs  $\mathcal{V}_{\gamma_{in}}(\Omega_i) \times \mathcal{U}_{\gamma_{in}}(\Omega_i)$  and the interpretation  $T(\mu)$  and  $\hat{T}(f)$  as mixed formulations for zero mean potentials of the local Neumann problems

$$\begin{aligned} \boldsymbol{\sigma}^\mu &= -\mathbb{K}\nabla u^\mu, & \nabla \cdot \boldsymbol{\sigma}^\mu &= R(\mu) \text{ in } \Omega_i, & \boldsymbol{\sigma}^\mu \cdot \mathbf{n} &= \mu \text{ on } \partial\Omega_i, \\ \boldsymbol{\sigma}^f &= -\mathbb{K}\nabla u^f, & \nabla \cdot \boldsymbol{\sigma}^f &= \Pi_0(f) \text{ in } \Omega_i, & \boldsymbol{\sigma}^f \cdot \mathbf{n} &= 0 \text{ on } \partial\Omega_i. \end{aligned}$$

In order to verify the uniqueness of solution of the global system, take zero data  $f = 0$  and  $u_D = 0$ . From the well posedness of the local solver  $\hat{T}(f)$ , thus  $\boldsymbol{\sigma}^f = 0$  and  $u^f = 0$  for  $f = 0$ . Thus the global system (4.5) becomes: find  $\tilde{u}_0 \in U_0$  and  $\tilde{\lambda} \in \Lambda_\gamma$ , with  $\tilde{\lambda}|_{\Gamma_N} = 0$ , solving

$$\begin{aligned} \int_{\Omega} \mathbb{K}^{-1} \boldsymbol{\sigma}^{\tilde{\lambda}} \cdot \boldsymbol{\sigma}^\mu dx - \int_{\Omega} \tilde{u}_0 \nabla \cdot \boldsymbol{\sigma}^\mu dx &= 0, \quad \forall \mu \in \Lambda_\gamma, \text{ with } \mu|_{\Gamma_N} = 0, \\ \int_{\Omega} \nabla \cdot \boldsymbol{\sigma}^{\tilde{\lambda}} \varphi dx &= 0, \quad \forall \varphi \in U_0. \end{aligned}$$

Taking test function  $\varphi = \nabla \cdot \boldsymbol{\sigma}^{\tilde{\lambda}} \in U_0$ , the last equation turns into  $\int_{\Omega} \nabla \cdot \boldsymbol{\sigma}^{\tilde{\lambda}} \nabla \cdot \boldsymbol{\sigma}^{\tilde{\lambda}} dx = 0$ , implying that  $\nabla \cdot \boldsymbol{\sigma}^{\tilde{\lambda}} = 0$ . Consequently, by taking  $\mu = \tilde{\lambda}$  in the first equation we obtain  $\int_{\Omega} \mathbb{K}^{-1} \boldsymbol{\sigma}^{\tilde{\lambda}} \cdot \boldsymbol{\sigma}^{\tilde{\lambda}} dx = 0$ , implying that  $\boldsymbol{\sigma}^{\tilde{\lambda}} = 0$  (i.e.,  $\tilde{\lambda} = 0$  as well).

Finally, the remaining equation is  $\int_{\Omega} \tilde{u}_0 \nabla \cdot \boldsymbol{\sigma}^{\mu} dx = 0$ ,  $\forall \mu \in \Lambda_{\gamma}$ , with  $\mu|_{\Gamma_N} = 0$ . Let  $\mu = \mu^* \in \Lambda_{\gamma}$ ,  $\mu^*|_{\Gamma_N} = 0$ , be such that  $\tilde{u}_0 = R\mu^*$  (by Lemma 2). Recalling that  $\nabla \cdot \boldsymbol{\sigma}^{\mu^*} = R(\mu^*)$ , we conclude that  $\tilde{u}_0 = \nabla \cdot \boldsymbol{\sigma}^{\mu^*}$ .

## A.2 Proof of Theorem 2

Let us denote by  $(\tilde{\mathbf{s}}, \tilde{w}) \in \mathbf{V}_\gamma \times U_{\gamma_{in}}$  the solution of the well posed mixed formulation (4.6). Set  $\tilde{w} = \tilde{w}_0 + \tilde{w}^\perp$ ,  $\tilde{\nu} = \tilde{\mathbf{s}} \cdot \mathbf{n}|_\Gamma$ . By testing (4.6) with  $v \in U_{\gamma_{in}}$  and  $\mathbf{q} \in \mathring{\mathbf{V}}_{h_{in}}$ , both with support in  $\Omega_i$ , and using the fact  $\int_{\Omega_i} \tilde{w}_0 \nabla \cdot \mathbf{q} dx = 0$ , we obtain

$$\begin{aligned} \int_{\Omega_i} \mathbb{K}^{-1} \tilde{\mathbf{s}} \cdot \mathbf{q} dx - \int_{\Omega_i} \tilde{w}^\perp \nabla \cdot \mathbf{q} dx &= 0, \\ \int_{\Omega_i} \nabla \cdot \tilde{\mathbf{s}} v dx &= \int_{\Omega_i} f v dx. \end{aligned} \quad (\text{A.1})$$

Using test functions  $\mathbf{q} = \boldsymbol{\sigma}^\mu$  of facet type, for arbitrary  $\mu \in \Lambda_\gamma$  with  $\mu|_{\Gamma^N} = 0$ , we obtain

$$\int_{\Omega} \mathbb{K}^{-1} \tilde{\mathbf{s}} \cdot \boldsymbol{\sigma}^\mu dx - \int_{\Omega} \tilde{w}_0 \nabla \cdot \boldsymbol{\sigma}^\mu dx = - \int_{\Gamma_D} u_D \boldsymbol{\sigma}^\mu \cdot \mathbf{n}, ds. \quad (\text{A.2})$$

where we used the fact  $\nabla \cdot \boldsymbol{\sigma}^\mu \in U_0$  is ortogonal to  $\tilde{w}^\perp$ . Finally, for  $\varphi \in U_0$ , the last equation in (4.6) turns into

$$\int_{\Omega} \nabla \cdot \tilde{\mathbf{s}} \varphi dx = \int_{\Omega} f \varphi dx. \quad (\text{A.3})$$

Let  $(\tilde{\boldsymbol{\sigma}}, \tilde{u}, \tilde{\lambda})$  be the solution given by the MHM-H(div)- $\mathcal{E}_\gamma$  method. By confronting the corresponding local Neumann solvers (associated to  $\mu = \tilde{\lambda}$ ) and equations in (A.1), the following identities hold for the differences  $\tilde{\boldsymbol{\sigma}} - \tilde{\mathbf{s}}$  and  $\tilde{u}^\perp - \tilde{w}^\perp$ , with  $(\tilde{\boldsymbol{\sigma}} - \tilde{\mathbf{s}})|_{\partial\Omega_i} = (\tilde{\lambda} - \nu)|_{\partial\Omega_i}$ :

$$\begin{aligned} \int_{\Omega_i} \mathbb{K}^{-1} [\tilde{\boldsymbol{\sigma}} - \tilde{\mathbf{s}}] \cdot \mathbf{q} dx - \int_{\Omega_i} (\tilde{u}^\perp - \tilde{w}^\perp) \nabla \cdot \mathbf{q} dx &= 0, \quad \forall \mathbf{q} \in \mathring{\mathbf{V}}_{h_{in}}, \\ \int_{\Omega_i} \nabla \cdot [\tilde{\boldsymbol{\sigma}} - \tilde{\mathbf{s}}] \varphi dx &= 0, \quad \forall \varphi \in U_{h_{in}}^\perp. \end{aligned} \quad (\text{A.4})$$

By using (A.2)-(A.3), then  $\tilde{u}_0 - \tilde{w}_0 \in U_0$  and  $\tilde{\lambda} - \tilde{\nu} \in \Lambda_\gamma$ , with  $\tilde{\lambda} - \tilde{\nu}|_{\Gamma^N} = 0$  solve

$$\begin{aligned} \int_{\Omega} \mathbb{K}^{-1} (\tilde{\boldsymbol{\sigma}} - \tilde{\mathbf{s}}) \cdot \boldsymbol{\sigma}^\mu dx - \int_{\Omega} (\tilde{u}_0 - \tilde{w}_0) \nabla \cdot \boldsymbol{\sigma}^\mu dx &= 0, \quad \forall \mu \in \Lambda_\gamma \text{ with } \mu|_{\Gamma^N} = 0, \\ \int_{\Omega} \nabla \cdot (\tilde{\boldsymbol{\sigma}} - \tilde{\mathbf{s}}) \varphi dx &= 0, \quad \forall \varphi \in U_0. \end{aligned} \quad (\text{A.5})$$

Observing from (A.4) that  $\tilde{\boldsymbol{\sigma}} - \tilde{\mathbf{s}} = \boldsymbol{\sigma}^{\tilde{\lambda} - \tilde{\nu}}$  and  $\tilde{u}^\perp - \tilde{w}^\perp = u^{\tilde{\lambda} - \tilde{\nu}}$ , then equations (A.4)-(A.5) imply that  $(\tilde{\boldsymbol{\sigma}} - \tilde{\mathbf{s}}, (\tilde{u}_0 - \tilde{w}_0) + (\tilde{u}^\perp - \tilde{w}^\perp), \tilde{\lambda} - \tilde{\nu})$  solve the MHM-H(div)- $\mathcal{E}_\gamma$  method for vanishing data  $f = 0$  and  $u_D = 0$ . Thus, Theorem 1 implies that  $\tilde{\lambda} = \tilde{\nu}$ ,  $\tilde{u}_0 = \tilde{w}_0$ ,  $\tilde{u}^\perp = \tilde{w}^\perp$ , and  $\tilde{\boldsymbol{\sigma}} = \tilde{\mathbf{s}}$ .  $\square$